THE UNIVERSITY *of* EDINBURGH

Systems redox biology analysis of cancer

Thesis presented for the degree of
Doctor of Philosophy,
University of Edinburgh

Hannah Johnston

October 2017

Supervisor: Dr Colin J. Campbell

Declaration of Authorship

I declare that this thesis is my own composition; that the work which is described has been carried out by me, unless otherwise stated; and that it has not been submitted in any previous application for a higher degree.

This thesis describes the results of research carried out in the School of Chemistry, University of Edinburgh, under the supervision of Dr Colin J. Campbell.

Hannah Johnston
University of Edinburgh
August 2017

Signed:

Date:

Abstract

The Warburg effect describes the survival advantage of cancer cells in that they can proliferate under low oxygen/hypoxic conditions via a less efficient pathway known as glycolysis. It has not yet been documented at which point, in an oxygen gradient, phenotypic changes occur. Measuring the intracellular redox potential (IRP) and its impact on cellular dynamics would provide greater insight into how disruption of redox homeostasis caused by changes in oxygen concentration leads to aberrant cell signalling and diseases such as cancer.

Current techniques in measuring IRP include redox-sensitive fluorescent proteins such as roGFP which is glutathione-specific. Measuring the concentration of one redox couple is, however, not an accurate representation of IRP as it does not necessarily inform about the state of other redox couples. Furthermore, fluorescent biosensors can suffer from photobleaching and may interact with other oxidants. The IRP was measured, in this work, using our newly developed novel-class of surface enhanced Raman scattering nanoparticles which can quantitatively measure the redox potential of cells *in vitro*. A "homemade" device was created to keep the cells under fixed pO_2 whilst obtaining measurements.

The IRP was correlated with the transcriptomic and downstream metabolic profiles of MCF7 breast cancer cells, under perturbed pO_2, using ^{1}H NMR spectroscopy (NMR), mass spectrometry (MS) and RNA-sequencing. Discriminatory metabolites were all associated with energy and glucose metabolism. Discriminatory microRNAs were all affiliated with the hallmarks of cancer; the regulation of some is controlled by transcription factors containing redox-sensitive motifs in their DNA binding domains.

Multivariate analysis techniques were used to analyse the different data streams in a holistic way that allows the correlation of redox potential, metabolism and transcription.

Lay Summary

There are still many unanswered questions about cellular mechanisms in cancer. Curing cancer is made more difficult by the fact that different cancers differ from each other and also that different patients respond differently to chemo- and/or radiotherapy. Current advances in research and technology are trying to push forward the concept of stratified medicine for patients and the disease.

One common feature shared amongst different cancer types is metabolic dysregulation. A survival advantage of cancer cells is that, compared to healthy cells, they often produce energy inefficiently without using oxygen which can make them resistant to therapy. One proposed explanation is that, despite using a less efficient energetic pathway, this altered metabolism provides the key building blocks required for rapid cell growth and makes the cells less oxidative. Being less oxidative may protect the cancer cell from death.

My project involves measuring how oxidative a cell is and correlating that to the cell's metabolism. Doing this allows for a better understanding of how the amount of oxygen in a tumour controls the cancer cell's ability to make energy and thus to evade therapy.

To measure how oxidative a cell is, my research group's engineered nanosensors were added to and taken up by the cells without inducing any toxic effects. These nanosensors are gold nanoparticles coated in reporter molecules that respond to oxidation by changing their conformation. A technique known as surface enhanced Raman scattering (SERS) was used to detect these changes in conformation. In short, when a laser is applied to a cell, light of different frequencies is returned, thus producing a spectrum which indicates the state of the reporter molecules. The gold particle acts like an amplifier, making the spectrum really intense so that it is possible to measure spectra from single particles in single cells.

Chemical analysis of cellular pathway activity was conducted to draw out discriminatory information relevant to changes caused by oxygen perturbation. This, in combination with SERS, allows me to get a chemical snapshot a cancer cell.

In conclusion, this work provides a deeper understanding of how cellular pathways are reprogrammed and controlled in response to the level of oxygen in their environment which may enlighten new strategies in cancer treatment.

Acknowledgements

Everyone who knows me would say I'm not a talker (said sarcastically) so I'll keep this concise. Doing this PhD was one massive rollercoaster ride. I may have come out of this with my hair a little on end but I enjoyed every minute of it. I got to meet and work with a lot of amazing people, in particularly the CJC and NMR groups and office 252. You are the nicest people and I will miss you all so much!

Juraj and Lorna (absolute legends) are my newest family members and have taught me so much, like what happens if you put a NMR spinner on incorrectly – thanks for bearing with my….wee mistakes.

I'd like to thank Logan Mackay for his support, banter and great music taste! If ever I had a bad day, I'd go visit the MS lab and see what gadgets he had made with his "research" 3D printer. You still owe me a superman logo baking mould!

To my supervisor, Dr. Colin Campbell, I can't actually thank you enough. You've been a fantastic teacher and role model and you should be very proud of how well you manage the group. My achievements within and outside the lab in the last 4 years can definitely be accredited to you. If only my bowling skills could be just as good as yours!

Last but not least, to my Padre and sisters, Grace and Ashleen, I love you. Thank you for letting me vent and providing me with (wine) support in any way possible. I'm the person I am today because of you.

Mumsy, you strong and inspiring woman, you battled and survived cancer during this PhD. This thesis is dedicated to you.

Contents

List of Figures

List of Tables

List of Abbreviations

A549 Adenocarcinomic Human Alveolar Basal Epithelial

ACACA Acetyl-CoA Carboxylase

ACLM ATP Citrate Lyase

AGO2 Argonaute 2

AQ Bis-(2-Anthraquinone Carboxamide)

AMP/ADP/ATP Adenosine Mono/Di/Triphosphate

AMPK AMP-Activated Protein Kinase

ARE Antioxidant Response Element

c-MYC Avian Myelocytomatosis Viral *Oncogene* Homolog

DFT Density Functional Theory

DGGR8 DiGeorge Syndrome Critical Region Gene 8

DHA Dehydroascorbic Acid

DNA Deoxyribonucleic acid

EMT Epithelial-Mesenchymal Transition

ETC Electron Transport Chain

FA Fatty Acid

FAD Flavin Adenine Dinucleotide

FASN Fatty Acid Synthase

FCS Fetal Calf Serum

FTICR Fourier Transform Ion Cyclotron Resonance

GC Gas Chromatography

Gpx Glutathione Peroxidase

GR Glutathione Reductase

GRP55 Orphan G-Protein-Coupled Receptor 55

Grx Glutaredoxin

GSH Glutathione (Reduced)

GSSG Glutathione (Oxidised)

H_2DFFDA 5-(and-6)-Carboxy-2',7'-Dihydrofluorescein Diacetate

HIF Hypoxia-Inducible Factor

HMDB Human Metabolome Database

HMG 3-Hydroxy 3-Methylglutaryl

HMGA High Mobility Group Protein

HPLC High Performance Liquid Chromatography

HSQC Heteronuclear Single Quantum Coherence

ICA Independent Component Analysis

IL6 Interleukin 6

IRP Intracellular Redox Potential

ISCU Cluster Assembly Protein

IVR Intervening Region

Keap1 Kelch-Like ECH-Associated Protein 1

LDA Lactate Dehydrogenase A

MAD MAX Dimerisation Protein

MAX MYC-Associated Protein X

MBA *para*-Mercaptobenzoic Acid

MCF7 Breast Adenocarcinoma

MiR/miRNA MicroRNA

MNT MAX Network Transcriptional Repressor

mRNA Messenger Ribonucleic Acid

MS Mass Spectrometry

mTOR Mechanistic Target of Rapamycin

NADH Nicotinamide Adenine Dinucleotide

NADPH Nicotinamide Adenine Dinucleotide Phosphate

NSCLC Non-Small Lung Cancer

NMR Nuclear Magnetic Resonance

Nox NADPH Oxidase

NS Nanoshell

O-PLSDA Orthogonal Partial Least Squares Discriminant Analysis

OXPHOS Oxidative Phosphorylation

PA Glycerolphosphatidic Acid

PBS Phosphate Buffer Solution

PC Glycerophosphocholine

PCs Principal Components

PCA Principal Component Analysis

PDC Pyruvate Dehydrogenase Complex

PDK1 Pyruvate Dehydrogenase Kinase 1

PE Glycerophosphoethanolamine

PG Glycerolphosphoglycerol

PGC-1α Prolyl Hydroxylase

PI Glycerophosphoinositol

PLP Pyriodoxal-5-Phosphate

PLS-DA Partial Least Squares Discriminant Analysis

PPP Pentose Phosphate Pathway

Prx Peroxiredoxin

PS Glycerolphosphoserine

PTEN Phosphatase and Tensin Homolog

RISC RNA-Induced Silencing Complex

RNA Ribonucleic Acid

RNS Reactive Nitrogen Species

RoGFP Redox-Sensitive Green Fluorescent Protein

ROS Reactive Oxygen Species

rRNA Ribosomal Ribonucleic Acid

RxYFP Redox-Sensitive Yellow Fluorescent Protein

SA Surprisal Analysis

SERS Surface Enhanced Raman Spectroscopy

SOD Superoxide Dismutase

SPT Palmityltransferase

SREP-1c Sterol Regulatory Element Binding Protein-1c

SVD Single Value Decomposition

TBH *tert*-Butylhydroperoxide

TCA Tricarboxlyic Acid Cycle

TF Transcription Factor

TGF-β Transforming Growth Factor Beta

Trx Thioredoxin

UDP-Glc Uridine Diphosphate Glucose

UMP/UDP/UTP Uridine Mono/Di/Triphosphate

YY1 Ying Yang 1

Chapter 1: Introduction

1.1/ Metabolomics and Chemometric Analysis

The omics sciences are becoming increasingly recognised and utilised in the study of biological systems. Omics is divided into the following main subgroups: genomics (genes), transcriptomics (mRNA), proteomics (proteins), metabolomics (metabolites) (Figure 1.1).

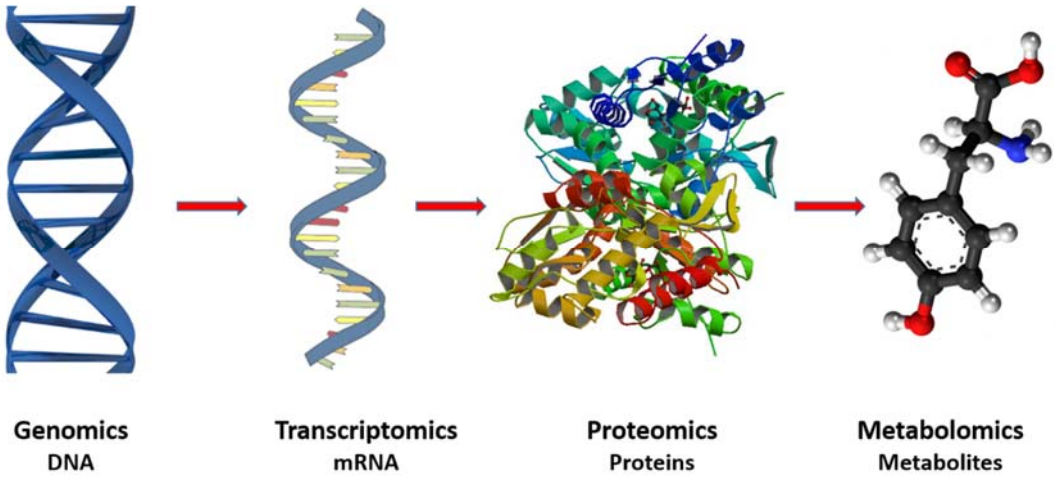

Figure 1.1. Schematic representation of Central Dogma and associated omics.

The latter has the ability to measure hundreds of endogenous and exogenous low molecular weight metabolites, making it a powerful tool in many scientific areas. Metabolic profiling has been used to study systems biology since the late 1990s, leading to the establishment of metabolomics and metabonomics. The former is defined as the biochemical profile generated from the collection of metabolites present in a cell, tissue or organism under certain conditions. The latter is the biochemical profile generated from a cell's, tissue's or organism's response to an external stimulus (e.g. drug, genetic defect).[1]

Metabolomics can be divided into two different analyses: targeted and untargeted. Targeted analysis requires the known identity and characteristics of pre-defined metabolites so that they can be separated from the matrix of data for quantification. Untargeted analysis, on the other hand, requires no *a priori* knowledge. Each of these procedures dictate the nature and levels of the extracted metabolites. A non-targeted approach was adopted in this work, making the objective to extract the maximum possible number of metabolites in a quantitative and non-biased manner with minimal metabolite loss.

Metabolite concentrations represent marks of genomic changes and responses of cells to an external stimulus. A small change in gene or protein expression and/or activity can often create a large downstream effect on the metabolite level. Metabolites express a phenotype of processes that have happened, providing data about systems biology which is complementary to information generated from other omics data. The fact that one transcript can encode, on average, ten different protein isoforms, with each of these proteins undergoing possible post-translational modifications, stunts the development of proteomic technologies. *Chubukov et al.* highlighted the fact that due to enzyme modifications and allosteric regulation, metabolic fluxes are not dependent on enzyme concentration. The sheer complexity of proteome makes metabolomics a more attractive area to research. Independently or in conjunction with genomic or proteomic data, models of biological pathways and networks can be developed.

1.1.1 Cancer Metabolomics

The number of publications in cancer metabolomics has increased drastically in the last 10 years. These studies are often conducted using urine or blood samples. Clinical samples have their advantages; however, cell analysis can be more relevant to answering specific questions. Metabolomic profiling of cell cultures offers a unique insight into the action and behaviour of a specific cell type under different conditions. The benefit of using cells over whole organisms is that they can be controlled for

homogeneity and exposed to specific conditions so that molecular information and answers to biological questions can be easily obtained. Furthermore, cells do not suffer from confounding factors such as age, health and gender and patient variability.[2] Cells may not directly provide diagnostic biomarkers without further validation but can suggest potential leads for further testing, assessment and validation on tissue *in vivo*.

Early detection of disease through the discovery of new biomarkers is an attractive driving force for research. Previous metabolomics research has identified potential biomarkers, for example differences between ER+ and ER- breast cancer cells [3] and differences in lipid profiles of various breast cancer subtypes.[4] This highlights the complexity of treating cancer as not only are different cancers different but also each subtype of cancer is different, making diagnosis and therapy extremely difficult.

A thorough understanding of each cancer subtype will take us one step closer to personalised medicine: one way of doing so is through metabolic profiling. Metabolites separation and identification is achieved thanks to several advancements in the following analytical techniques: Nuclear Magnetic Resonance (NMR) spectroscopy; Mass Spectrometry (MS) coupled to Gas Chromatography (GC) or High Performance Liquid Chromatography (HPLC); Raman Spectroscopy. NMR and MS have been demonstrated to be complementary and powerful in the complete characterization of the metabolome. MS provides higher sensitivity; however sample preparation is more complex, opening possibilities for experimental error. Furthermore, standards are needed for all metabolites which is difficult and expensive as MS can identify a large number of metabolites. NMR is reproducible and, with the introduction of cryogenically cooled NMR probes, enhancement of compounds present at low concentrations allows for better sensitivity and resolution.[5]

1.1.2 Cancer and Hypoxia

A survival advantage of cancer cells over normal cells is that cancer cells can proliferate under limited oxygen/hypoxic concentrations, a known hallmark of tumours. Under physiological conditions, cell energy metabolism is based primarily on oxidative phosphorylation (OXPHOS) in the mitochondria whereby oxygen is consumed and energy is produced in the form of ATP as electrons pass along the electron transport chain (ETC). Under hypoxic conditions, cells shift to a glycolytic phenotype which is less efficient than OXPHOS. An increase in lactate production can cause surrounding normal cells to undergo apoptosis as a result of decreased pH.[6]

Maintaining oxygen homeostasis requires the regulation of a variety of different genes. If cellular oxygen levels are inadequate, respiration switches over to anaerobic glycolysis from aerobic fatty acid metabolism to sustain ATP production. One key mediator of the hypoxic response is hypoxia-inducible transcription factor (HIF-1) complex. HIF-1, a heterodimer, constitutes the regulatory HIF-1α and catalytic HIF-1β subunits. HIF-1α is activated and binds to the hypoxia-responsive element in the regulatory DNA sequence when hydroxylation by prolyl and asparaginyl hydroxylases is inhibited. HIF-1α is thought to be a key mediator of the Warburg effect and it is, thus, important to gain a better understanding of oxygen sensing and signal transduction. More than 100 target genes of HIF-1α have been identified which control such processes as energy metabolism, angiogenesis and erythropoiesis.[7]

The tumour microenvironment can affect the efficacy of chemo- and radio-therapies, therefore it is important to characterise cellular dynamics and observe which biological pathways are affected by hypoxic conditions. Many studies have compared cancer cells under 21% pO_2 and hypoxic conditions (~1% pO_2) but it has not yet been documented at which point in an oxygen gradient phenotypic changes occur.[8], [9]

1.1.3 Analytical Platforms and Data Analysis

A problem associated with any omics study is the sheer volume of multivariate data to be processed and interpreted, making it difficult to extract what is actually biologically significant. In addition, careful experimental design is required to ensure that any changes measured are a function of the biological entity and not due to experimental bias and/or artefacts. Metabolic profiling has been combined with statistical chemometric and bioinformatic tools to reduce the dimensionality of the dataset and highlight biomarkers of the biological phenomenon of interest, for example cellular response to chemotherapeutic drugs.[10]–[12]

Below are some tools commonly used in the literature.[13] For all of them, a matrix X of size *n*x*m* (*n* = number of samples; *m* = number of variables) is inserted and converted to a Y matrix of size *n*, describing the class of each of the spectra. Variables which explain the class identification are the associated biomarkers.

1) **Principal Component Analysis (PCA)**

   PCA is one of the most commonly used tools in metabolomics. It is an unsupervised technique whereby the classes are not identified and the data are centred by the columns/samples of the matrix. PCA creates a new set of axes, called the principal components, which describes the data more efficiently. The first principal component (PC1) lies in the direction of the greatest variance in the data. A second principal component (PC2) is calculated orthogonal to PC1, as usually one component is insufficient to model the systematic variation of a data set. PC2 lies along the direction with the largest remaining variance (Figure 1.2). The variance decreases as more axes are added. Points that are close to each other have similar properties, whereas those far from each other are dissimilar. Furthermore, those close to the origin of the plane have average properties. The loadings plot gives an indication of the magnitude (large or small correlation) and the manner (positive or negative correlation) which the integrals contribute to the scores.

Integrals which have similar contributions group together. PCA, however, is highly sensitive to inherent noise in the data. Biomarkers are usually identified from PC1 and PC2 which do not necessarily contain relevant biological information about the variations between sample cohorts.[14], [15]

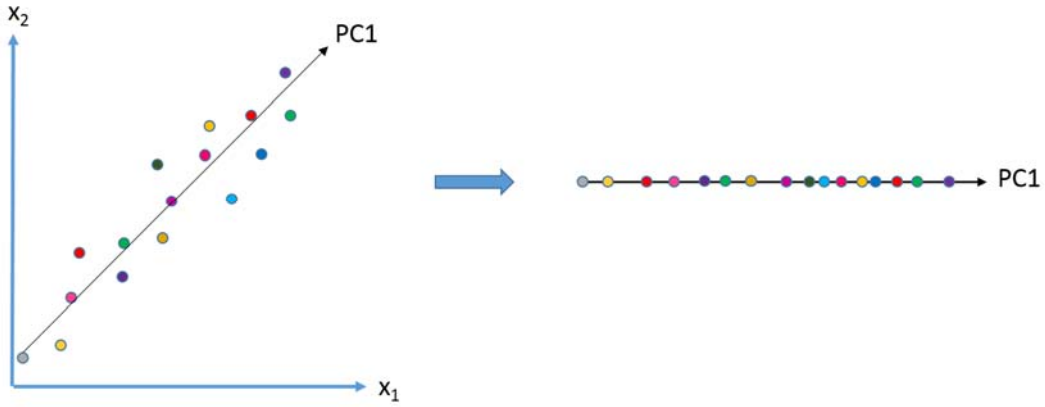

Figure 1.2. PCA reduces the dimensionality of the spectral data, thus patterns relating to pathological and physiological perturbation can be established. In this example, a simple 2D plot is reduced to 1D by measuring the distances of each sample point to PC1.

2) Independent Component Analysis (ICA)

ICA is an unsupervised learning algorithm. The initial matrix is centred (moving the data distribution to the origin of the multidimensional space) by rows/variables. It searches for statistical components that are independent of each other. ICA may be more meaningful than PCA because ICA uses higher order statistical methods which delivers more information with fewer components. ICA maximises the independence of components, whereas PCA maximises variation. PCA assumes a normal Gaussian distribution of biological features; ICA, on the other hand, identifies non-Gaussian components which are modelled as a linear combination of the biological features. The drawbacks of the method are that it chooses the number of components to be extracted to reduce data dimensionality. These components are not ordered in descending order of discriminatory power; therefore, it is

up to the user to define this. Furthermore, it is a stochastic method, meaning that the algorithm has to be run several times and averaged.[13], [15]–[17]

3) **Partial Least Squares Discriminant Analysis (PLS-DA)**

PLS-DA is often used in conjunction with PCA to verify the robustness of potential biomarkers.[16] A training set is created that is composed of class-preassigned features. This training set is then used to predict the class of an unknown sample. Like PCA, the initial matrix is centred by columns. PLS-DA suffers less from overfitting compared to PCA. A cross-validation technique is used to estimate the predictive ability of the model with increasing number of components. A scores and loadings plot are built in ranking order of significance.[2], [16], [18]

4) **Classification and Regression Trees (CART)**

Data are split into subsets until spectra are narrowed down to a certain homogenous class. The tree highlights those variables that best differentiate the class cohorts. Classification trees are non-parametric in that they do not assume a linear or non-linear relationship between the classes and the variables. However, they do not handle large datasets well.[18], [19]

1.1.4 Surprisal Analysis

Surprisal Analysis (SA) is grounded in (our favourite word in Chemistry) thermodynamics, and can be described using the analogy of a wee man stranded on an island (***Error! Reference source not found.***). Here he is surrounded by planks of wood which are positioned randomly; they are in a state of maximal entropy/disorder and no information can be interpreted from them - this represents the balanced state. The man realises he is not going to get rescued unless he does work to send information to any passing ships and planes. He positions the wood into the word "HELP" to send information that he is in distress. This work done represents the

transition away from maximal entropy to a state of lowered entropy. In other words, it can be viewed as deviation from the normal balanced state of lower energy to a cancerous state of higher energy because cancer cells proliferate quickly and need a lot of energy to do work. (Note that in Information Theory, entropy is seen as a physical quantity and not as a statistical measure of disorder.)

The biological molecular constraints represent phenotypes that exist as a profile of metabolite abundances which can change in response to environmental perturbations. Putting that into English, the constraints are the different amounts of work done/energy the wee man puts into rearranging the wood to signal for help. The phenotypes are what he has spelt with the wood, like "HELP" and "GET ME OFF THIS ISLAND" - these are two different phenotypes as they look different. In the context of this research, a phenotype is a group of metabolites/transcripts that change in a certain way under perturbed oxygen concentration. *Zadran et al.* discovered that in the balanced state, metabolite/transcript levels do not change and are actually common to both healthy and diseased states - these are the so-called "house-keeping" metabolites/transcripts which are essential for cells to survive (Figure 1.3). A thermodynamic weight for each metabolite/transcript is then assigned. Those with a higher weight from the balanced state reflect the influence of biological constraints. The relevance of the constraint to the system is ranked in order of how much it reduces the entropy from the balanced state. In each constraint, the metabolites are also ranked in order of their influence on that particular constraint - these are the biomarkers of the disease.

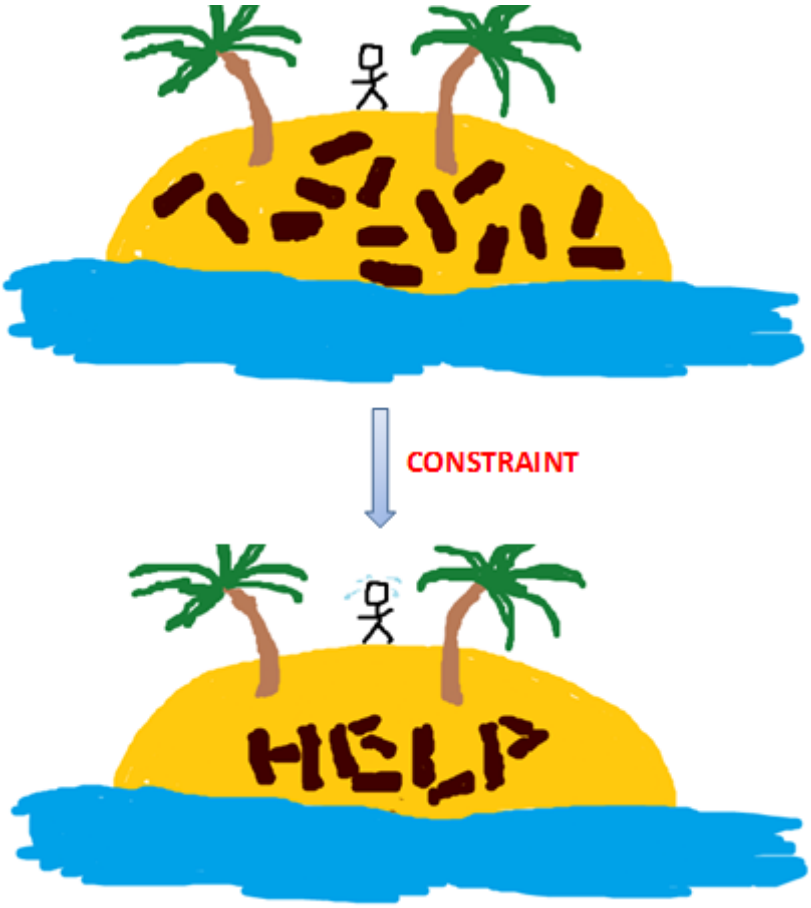

Figure 1.3. A cartoon representation of an analogy of surprisal analysis.

SA has been applied to cancer models, identifying genes that significantly contribute to the cancer state, the top 20 of which *Zadran et al.* affiliated with the hallmarks of cancer. The most highly expressed and stable RNAs were found to be those involved in maintaining cellular homeostasis. Some microRNAs (miRs) were also identified in being major contributors of the cancer signature, such as miR-206 which has recently been studied to be involved in lung cancer metastasis. Further studies demonstrated how inhibiting an RNA that was dominant in the cancer signature caused it to deviate towards the non-cancerous phenotype. For example, COL10A1, which is overexpressed in many tumours, contributed the most thermodynamically to the cancer state; however, once inhibited, *in vitro* cell proliferation reduced.[20] This highlights the potential of surprisal analysis in identifying possible disease biomarkers to help develop better therapeutics.

1.2/ Intracellular Redox Potential (IRP)

IRP is a measure of how oxidising/reducing the cellular environment is. This tendency to accept/donate electrons is quantitatively measured against the biochemical standard redox potential, $E^{\ominus}$, at pH 7 and 1 atm with all substrates at 1 M. The standard redox potential of a redox couple is dependent on the ability of the chemical species under study to accept/donate electrons. This is defined by the Nernst equation which is used in many current techniques to measure the IRP:[21]

$$E = E^{\theta} - \frac{RT}{nF} In \frac{[Red]}{[Ox]} \qquad \textit{equation 1.1}$$

whereby: R = gas constant (8.314 J K^{-1} mol^{-1}); T = temperature (K); n = number of electrons transferred in redox reaction; F = Faraday constant (9.649 x 10^4 C mol^{-1}); [Red] = concentration of reduced species; [Ox] = concentration of oxidised species.

IRP is highly regulated in cells and is critically important for normal physiological processes. Subtle changes in IRP create a dynamic redox signalling mechanism that regulates vital cellular processes: a more reducing environment is needed for proliferation, whereas a more oxidised environment is required for differentiation and cell cycle arrest (Figure 1.4).[22]

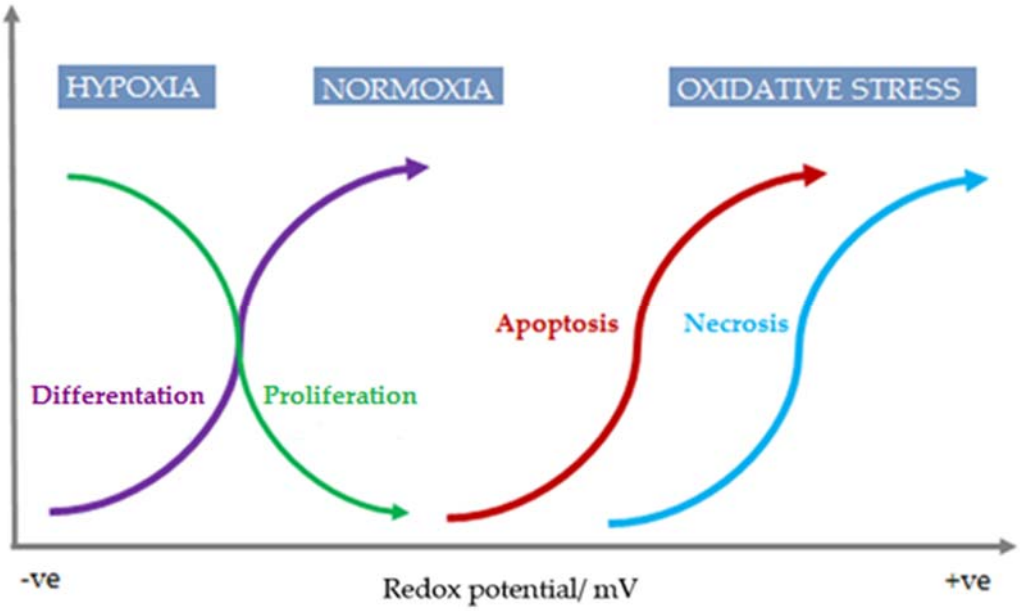

Figure 1.4. A change in intracellular redox potential can be viewed as a trigger to activate cellular switchboards which drive cells through different biological stages. (Adapted from [2].)

It is key to ascertain how redox chemistry impacts biological function because, as well as controlling normal cell function, its dysregulation is implicated in a range of diseases such as cardiovascular disease, neurodegeneration, and cancer.[22] In biological terms, it can be seen as the balance between the generation of reactive oxygen species (ROS) and the antioxidants that detoxify them.[21], [23], [24]

1.2.1 Production of ROS

During respiration in the mitochondria, oxygen can be converted to reactive oxygen and nitrogen species (ROS and RNS, respectively) in the ETC. A four-electron reduction of molecular oxygen to water occurs during OXPHOS, however partial reduction of oxygen can produce superoxide ($O_2^{\cdot-}$) and hydrogen peroxide (H_2O_2). ROS are also produced by mitochondrial membrane-bound nicotinamide adenine dinucleotide phosphate (NADPH) oxidase (Nox) which couples molecular oxygen with electrons transferred from NADPH to form superoxide anions. Superoxide can be converted into H_2O_2 by superoxide dismutase (SOD) and, subsequently, H_2O_2 can be converted to water and oxygen by the enzyme catalase or be reduced by glutathione peroxidase using glutathione (GSH). An excess of H_2O_2 can diffuse from the mitochondria to the cytosol and generate more reactive hydroxyl radicals through Fenton-like chemistry.

ROS influence cellular signalling through thiol oxidation of target proteins, resulting in a conformational change. This can have an impact on protein-protein and protein-DNA interactions. An excess of ROS/RNS can cause numerous diseases such as cancer.[21], [23]–[26] To detoxify these species, some antioxidants, such as GSH which is the most ubiquitous redox buffer in the body (1-11 mM), donate electrons which neutralise the ROS. These are oxidised in the process and then re-reduced by accepting electrons from NADPH. If the concentration of ROS increases beyond the point where antioxidants can degrade them, then the redox potential becomes more oxidising, causing oxidative stress and tissue damage (Figure 1.5**).** On the other end of the scale, hypoxia is the result of too little oxygen being available for OXPHOS which, from previous research, is thought to be a contributor to maintaining the malignancy of cancer.[21], [23]–[25], [27], [28]

1.2.2 The Body's Buffers

Hypoxia and oxidative stress cause cell death if severe or prolonged. Cells, however, maintain a homeostatic redox status through adaptive and genetic changes such as the antioxidant defence system which detoxifies ROS. If the antioxidant defence is compromised, free radicals and peroxides would otherwise damage DNA and other vital cellular components. The respiratory chain in mitochondria is the primary source of ROS.[29] Cellular responses to hypoxia include increased glycolytic metabolism and glucose transport. The question as to how mitochondria respond to hypoxia still remains unanswered.[30]

1.2.2.1 Glutathione

Redox potential is controlled by redox couples. One example is the tripeptide GSH, (structure found in Figure 1.5), which is synthesised naturally from L-cysteine, L-glutamic acid and glycine in the cytosol using the enzymes γ-glutamylcysteine synthetase and GSH synthetase.[31], [32] GSH contains a redox-active thiol group and acts as an endogenous reducing agent by donating electrons to peroxides, catalysed by selenium-dependent glutathione peroxidases (Gpx), or to disulfides, catalysed by gluteredoxins. The standard redox potential (i.e. the tendency for a chemical species to become reduced) of cytosolic GSH is -289mV [33] and it makes up 90% of the total low molecular weight thiols in cells.[34] Because mitochondria do not contain catalase, H_2O_2 is reduced by GSH and either peroxiredoxin or Gpx. Oxidised GSH (GSSG) is then re-reduced by NADPH-dependent GSSG reductase (GR).

GSH is predominantly present in the reduced state, thus a low GSH:GSSG ratio is considered indicative of oxidative stress. As the level of GSSG increases, so does the level of protein disulfides which alters their function. Glutaredoxin (Grx), however, can reduce these disulfides using the reductive power of GSH. The resultant GSSG can be re-reduced by NADPH (Figure 1.5).[22], [29], [35]

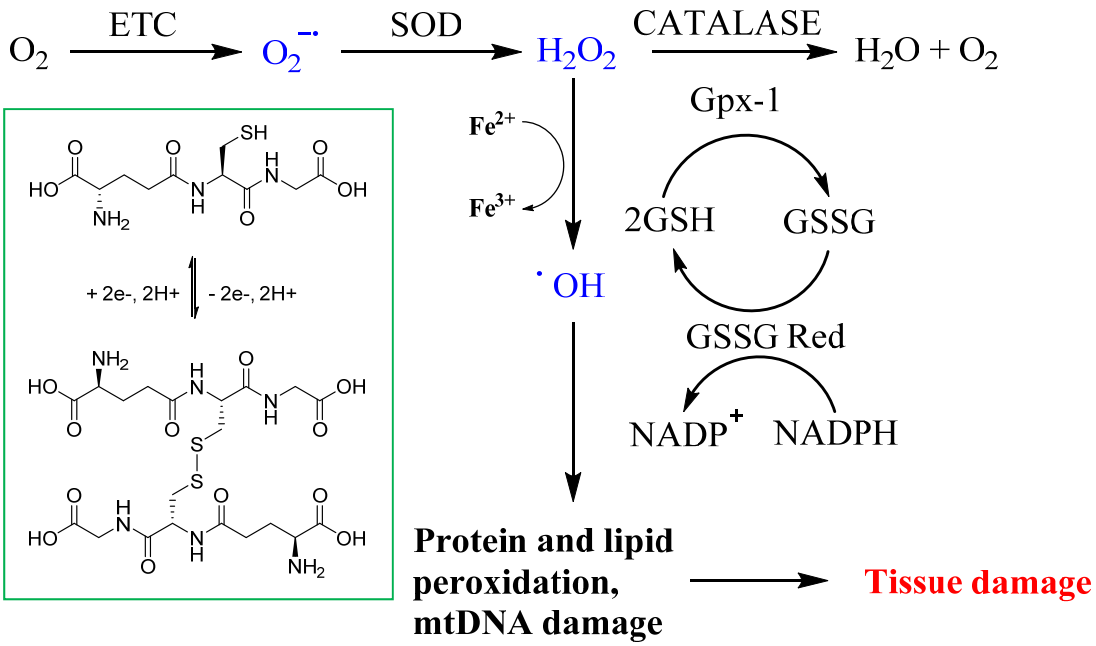

Figure 1.5. Respiration in the mitochondria creates reactive oxygen species which, if not detoxified by antioxidants, can cause oxidative stress and tissue damage. SOD = superoxide dismutase; ETC = electron transport chain; Gpx-1 = glutathione peroxidase.

1.2.2.2 Nicotinamide Adenine Dinucleotide Phosphate

NADPH is generated from the Pentose Phosphate Pathway (PPP). It is a major source of electrons for reductive biosynthesis. One role of NADPH is to reduce GSSG into its sulfhydryl form by donating electrons to flavin adenine dinucleotide (FAD) which is tightly bound on the enzyme glutathione reductase (GR). These electrons are then transferred to the disulfide bridge of GSSG. A similar process also occurs with oxidised thioredoxin (Trx) (Figure 1.6).[36]

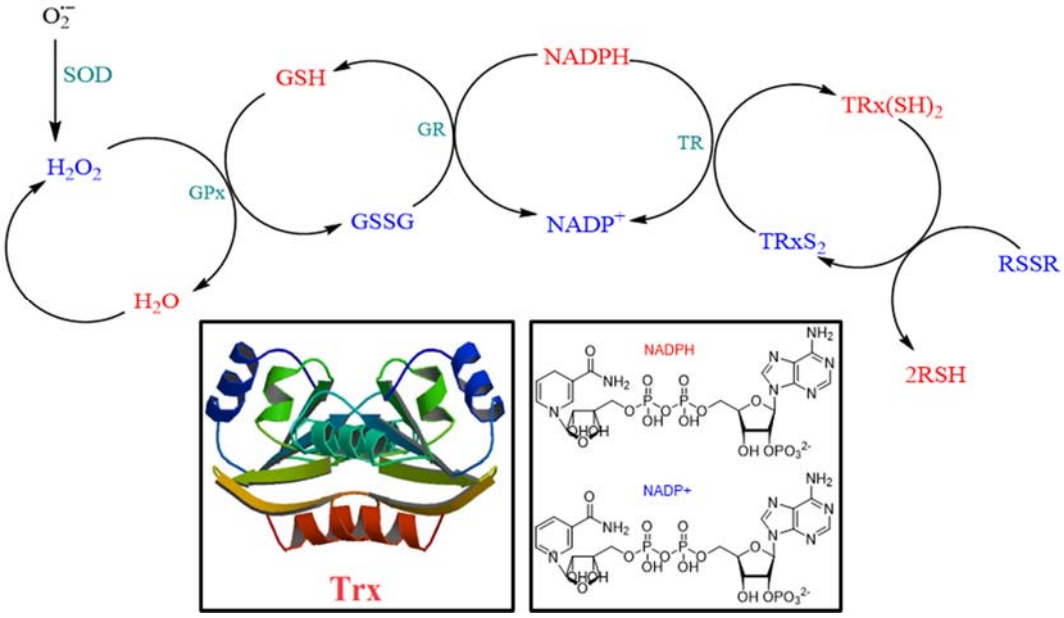

Figure 1.6. Interlinking of intracellular redox couples and their structures.

1.2.2.3 Thioredoxin

The Trx system incorporates Trx, thioredoxin reductase (TR) and NADPH, and is a key regulator of oxidative stress. Trx is a ubiquitous antioxidant enzyme, present in micromolar concentration.[37] There are two types: Trx1 which is present in the cytosol and nucleus and Trx2 which is found in the mitochondria. In the cell, Trx is thermodynamically stable in the oxidised form which acts as a driving force for Trx to reduce oxidised proteins (refer to Figure 1.7 for mechanism of action). The redox potentials for Trx1 and Trx2 have been shown to be -283 mV and -348 mV, respectively.[38]–[40] As well as being an antioxidant, Trx regulates redox signalling by controlling many transcription factors such as Nrf2, NF-κB and p53. Peroxiredoxins (Prx) also rely on Trx to remove H_2O_2, ROOH and $ONOO^-$.[29], [41]

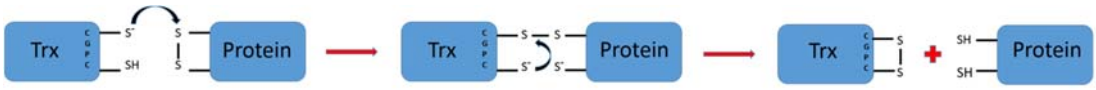

Figure 1.7. The low pKa value of the thiolate anion on the N-terminal cysteine on the conserved CGPC active site motif allows it to undergo nucleophilic attack on the disulphide of a substrate protein. The disulfide complex undergoes exchange reduction by nucleophilic attack of the C-terminal cysteine of the CGPC motif. Oxidised Trx is re-reduced by TR at the expense of NADPH. (Adapted from [40].)

1.3/ Current Techniques for Measuring Intracellular Redox Potential

1.3.1 Redox-Sensitive Fluorescent Proteins

The redox environment can be expressed using the equation below:

$$redox\ environment = \sum_{i=1}^{n\ (couple)} \mathrm{E}i\ x\ [reduced\ species]i \qquad \textit{equation 1.2}$$

whereby: E*i* = the half-cell reduction potential for a given redox couple; [reduced species]*i* = the concentration of the reduced species of that redox couple. The redox environment is the summation of all redox couples but this is impractical to measure as there are many redox couples in a cell. Instead, the redox state of one predominant redox couple present in cells could be measured to be representative of the redox environment. GSH is one such redox couple.[42] Current and present work use solely GSH to measure intracellular redox potential.

Redox-sensitive green fluorescent protein (roGFP) and redox-sensitive yellow fluorescent protein (rxYFP) are glutathione-specific genetically encoded fluorescent proteins. They contain cysteine residues located near the fluorophore which form reversible intramolecular disulfide bonds in response to redox dynamics. Oxidation results in a conformational change, forming a conjugated π-electron system capable of absorbing and emitting visible light. Their use is advantageous in that the encoded probes can be localised to specific cell compartments. Glutaredoxin (GR) is required to catalyse the direct equilibration with GSH by transferring the *S*-glutathionlyated cysteine to the fluorescent probe.[27], [43]

One problem associated with previous roGFP biosensors is that they can interact with other oxidants and/or have poor temporal resolution. Work, however, has since advanced on the usage of roGFPs by fusing them with human glutaredoxin-1 (Grx1) to enable dynamic live imaging of the GSH:GSSG redox couple in different cellular

compartments. Grx1 does this by catalysing the equilibration rate between roGFP and the cellular redox pair of interest.[44]

Fluorescence labelling, however, has its downfalls. Each probe requires specific excitation wavelengths in the visible region which can lead to photobleaching. Secondly, the fluorescence signature can be broad and nonspecific. The optical signals of different probes can show spectral overlap, limiting their multiplexing capability.[26], [45] Furthermore, it is possible that the fluorescent label could block a binding site and, consequently, affect molecular interactions.[46], [47] The fluorescent proteins only respond to changes in GSH:GSSG concentrations; however, this is not the only buffer in the body. Other redox couples include cysteine/cystine and thioredoxins (Trx_{red}/Trx_{ox}) which are maintained in non-equilibrium but stable states. They are independently regulated and their spatiotemporal pattern between and within cellular compartments may be non-uniform. For example, redox couples would exist more in the oxidised form in the endoplasmic reticulum (ER) to enable the oxidative folding of nascent proteins.[32] In the ER, the ratio of GSH:GSSG is 3:1, whereas in the cytoplasm and mitochondria ratios exceed 10:1. Furthermore, approximately 90% of GSH is found in the cytosol, 10% in the mitochondria and a small amount in the ER.[34] Measuring the concentration of one redox couple is, therefore, not an accurate representation of the intracellular redox potential as it does not necessarily inform about the state of other redox couples.

1.3.2 High Performance Liquid Chromatography

GSH and GSSG have characteristic retention times, allowing for their simultaneous separation and quantitation in complex biological samples. Quantification and electrochemical detection of intracellular GSH has been investigated via HPLC in numerous models such as autism.[22]

HPLC, too, comes with its drawbacks. Firstly, a derivatisation step is often needed to improve sensitivity, therefore prolonging analysis time. Secondly, HPLC is used in

conjunction with electrochemical or mass spectrometry detectors. Thirdly, cell lysis is required to extract the desired components. Doing so prevents the measurement of GSH in different cellular compartments and there is also a threat of GSH oxidation when exposed to air during cell lysis.[48]

1.3.3 Nuclear Magnetic Resonance Spectroscopy

Quantification of live-cell GSH and GSSG has recently been measured using heteronuclear single quantum coherence (HSQC) NMR. Isotopically labelled GSH was taken up through high affinity plasma membrane glutathione transporters in yeast cells. The level of uptaken GSH was compared to cells with a GSH biosynthesis defect which were incubated in media containing labelled GSH. Samples were then spiked with *tert*-butylhydroperoxide (TBH), which induced oxidative stress, and, again, were monitored via NMR over 180 min. The exact concentration of GSH and GSSG was obtained using, first, the DTNB-GSSG reductase recycling assay as a calibrant. The measured GSH and GSSG concentrations were plotted against their NMR peak intensities, and the exact concentrations of GSH and GSSG were calculated from the best fit regression through the origin of this plot. The two concentrations and estimated cellular volume were plugged into the Nernst equation so that the IRP could be established.[28]

Dynamic nuclear polarisation has been applied for noninvasive metabolic imaging of tumour redox state and pH. The reduced and oxidised forms of vitamin C (ascorbic acid and dehydroascorbic acid (DHA), respectively) were used as probes for extracellular and intracellular redox potential as they couple to GSH and NADPH. Furthermore, their long T_1 relaxation times *in vitro* and *in vivo* make them ideal for hyperpolarised NMR spectroscopy. DHA is rapidly reduced by GSH or GSH-dependent enzymes and NADPH-dependent enzymes such as thioredoxin reductase. These systems rely on NADPH for reducing power, therefore it is postulated that the rate of DHA reduction is proportional to the amount of NADPH present.[49]

1.4/ Surface Enhanced Raman Scattering (SERS)

Sir C.V. Raman experimentally observed in 1928 that when molecules are irradiated with a monochromatic incident beam, the surrounding electron cloud absorbs and re-emits photons. Most of the re-emitted photons are of the same wavelength as the incident light; this is termed elastic/Rayleigh scattering. However, some of the re-emitted photons are of different wavelength to the incident light; this is termed inelastic/Raman scattering.[50] Nearly 1 in 10^7 of the incident photons collide with molecules, thus they lose some of their energy and scatter at a lower frequency - these photons are termed Stokes radiation. Some incident photons may gain energy from the molecules and scatter at higher frequency if they were already excited - these photons are termed anti-Stokes radiation. Intense incident beams are required as the intensity of scattered radiation is very small, therefore lasers are commonly used.

The amount of inelastic scattering depends on the level of vibration of different molecular bonds; the spectrum is, therefore, directly correlated to biochemical species, analogous to a molecular fingerprint.[46], [51], [52] In conventional Raman spectroscopy, the incident radiation does not coincide with an absorption frequency of the molecule. The emitted photons are unstable and only a "virtual" transition occurs before relaxing back to the electronic ground state, as depicted in Figure 1.8.[50]

The signal intensity for a given vibrational mode is proportional to laser intensity and to the Raman cross-section. The cross-section can be seen as the spatial extent of the interaction between a target molecule and the incoming beam. In other words, the larger the cross-section, the more likely a collision between the molecule and a photon. Inelastic scattering is an intrinsically weak phenomenon and, so, the signal strength that reaches the detector is very poor. Surface-enhanced Raman scattering (SERS) is a variant of Raman spectroscopy that can be used to enhance this signal.

SERS was first observed in 1973 for pyridine absorbed on a roughened silver electrode. There are two proposed mechanisms for the enhanced Raman effect.

Firstly, *Moskovits* and *Kerker et al.* proposed that the surface enhancement is due to the electromagnetic effect. This involves the optical excitation of surface plasmons as a result of the adsorption of molecules on a roughened metal support. These plasmons are the collective oscillations of delocalised conduction electrons that lie parallel to the metal surface which generate strong electromagnetic fields. It is these oscillating electric fields that are responsible for the enhancement of the Raman vibrational modes and, therefore, Raman signal of molecules in close vicinity to the metal surface (typically no more than ~10 nm away).[51], [53] Secondly, the chemical enhancement mechanism is related to a change in the electronic properties of the adsorbate. The mechanism as to which this occurs remains under debate. One proposed explanation is that charge transfer between the chemisorbed analyte and the metal surface can increase the polarisability of the molecule which, subsequently, increases the Raman scattering.[50], [51]

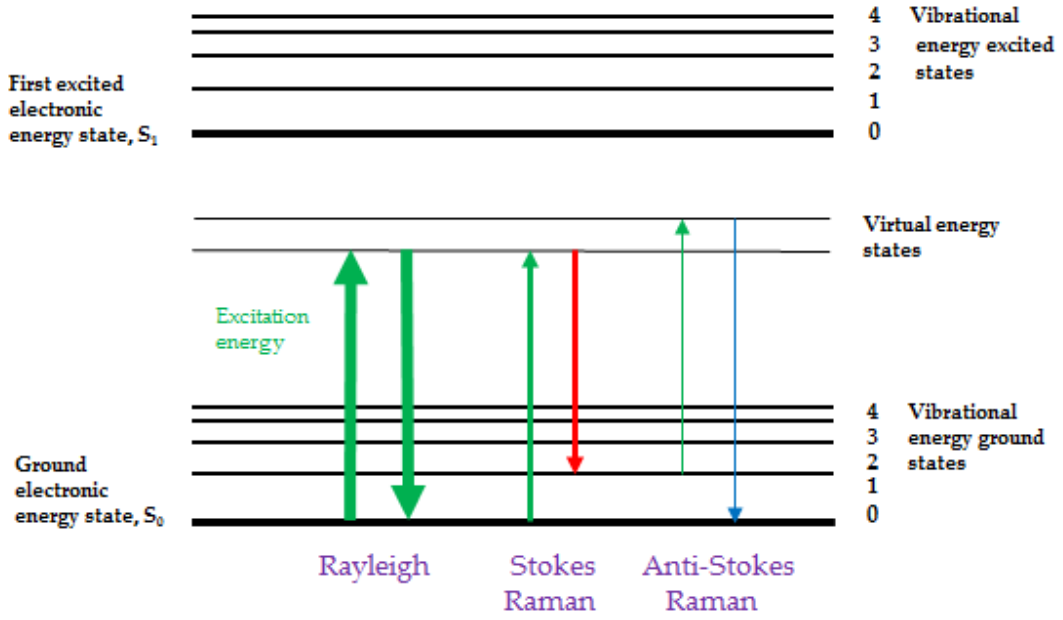

Figure 1.8. When cells are illuminated with a laser beam, emitted light is collected with a lens and sent through a monochromator which filters out intense Rayleigh scattering. The rest is dispersed onto a charge coupled device detector. The Raman shifted photons are of lower energy to the incident light (red shifted). This loss in energy is characteristic of the nature of each bond.

Fluorescence is a well-established technique, with countless available fluorescent probes that can be attached anywhere to the user's desire. It offers very high efficiency and sensitivity and has single-molecule detection. Although SERS can provide the same, it has the added potential complications in the practical implementation and is not as well developed as fluorescence. These shortcomings, however, can easily be counterbalanced by the following advantages. Fluorescence stability is a major issue when using fluorophores and excitation is limited to the visible wavelength. Photo-bleaching is likely to occur, particularly with the use of dyes. SERS, in principle, can be used at any excitation wavelength, as long as the molecule of interest is resonant at that wavelength, and be directly applied to any molecule, whereas a fluorophore is required for fluorescence. The specificity of SERS is also extremely high so that detection of a certain molecule can be easily detected from any background noise which is an issue inherent in other techniques used on biological samples. Simultaneous monitoring of a variety of probes/tags is possible with SERS due to each having a unique SERS fingerprint.[51]

1.5/ New Approach to SERS Measurement

Advances in nanotechnology have led to the development of prototypes to be used in biomedical applications and optimised therapy.[54], [55] SERS has been applied to many different fields from pharmaceutical discovery to cancer detection.[23], [53], [56]–[58] Silver exhibits the largest Raman enhancement, however gold is more biocompatible as it exhibits enhancement in the near-IR region of light.[51], [58]

The Campbell group have engineered gold nanosensors that are a class of engineered nanoparticles comprising a silica core (diameter of 125 nm) coated in a thin layer of gold. Thiols have a high chemical affinity for gold and form a strong covalent bond. These nanoshells (NS) (total diameter of 150 nm) are functionalised with a specific concentration of redox-active reporter molecule that allows for a monolayer coverage, avoiding steric hindrance and re-orientation of the molecules.[59] The surface chemistry of the NS can be easily manipulated to cover a wider potential range.

Conjugation with different reporter molecules allows for enhanced targeting to subcellular compartments. The gold nanosensors deliver chemical information of intrinsic cellular molecules in close vicinity. They contain a quinone moiety which undergoes a reversible 2 e^-, 2 H^+ redox reaction which results in a change in their structure and, hence, a difference in the Raman spectrum will be observed. The nanosensors enhance the Raman spectrum greater than 8 orders of magnitude.[23], [46], [60] The nanosensors can be controllably delivered to the cytoplasm, without any toxic effects allowing redox potential to be monitored in a reversible and non-invasive manner (Figure 1.9).[23] The nanosensors have a potential window of between -470 and +130 mV vs normal hydrogen electrode (NHE) which allows for IRP of cells in extreme hypoxic and oxidative stress conditions.[61]

Density functional theory (DFT) calculations were compared to the spectroelectrochemisty of the nanosensors under different redox potentials. Specific signals changed in response to the redox environment. In this work, the NS were functionalised with Bis-(2-Anthraquinone carboxamide) (AQ). For AQ, the signals at 1669 cm^{-1} and 1606 cm^{-1} corresponded to the quinone C=O stretch and the amide stretch/symmetric ring breathing, respectively. Applying a laser in the near-IR allows for deeper penetration with little damage to the cell as low-energy photos are used.

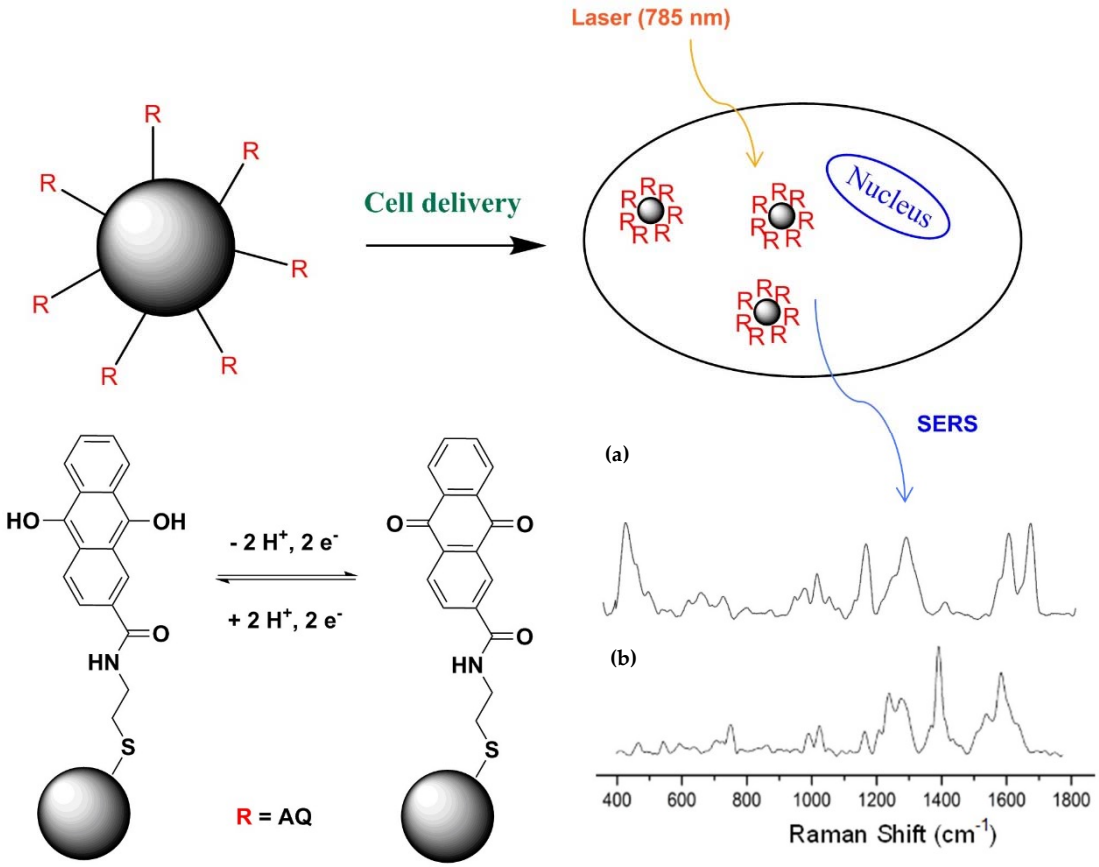

Figure 1.9. AQ functionalised NS are delivered to the cytoplasm. A laser is applied and a Raman spectrum of the AQ-NS is given. The ratio of the oxidised (a) and reduced (b) forms are inserted into the Nernst equation to give the intracellular redox potential. As the AQ is oxidised from the hydroxyl form to the carbonyl form, a different Raman spectrum will be produced. Spectral features include the: quinone C=O stretch (1666 cm^{-1}), aromatic C-C stretch (1430 cm^{-1}), aromatic C-H wag (1180 cm^{-1}). The intensity peak at 1666 cm^{-1} is used to quantify the redox potential as it is less prone to interference from the silica background.

1.6/ Project Aims

1) Use analytical techniques in conjunction with surprisal analysis to analyse differences in the metabolic and transcriptomic profiles of cells under normal physiological and perturbed conditions.

2) Use nanosensors to map redox potential distributions in living cells to correlate the effect of redox signalling on cell phenotype under normal physiological and perturbed conditions.

3) Create a pathway map by integrating biological networks to help in the recognition of redox-sensitive sites and their interconnectivity with each other.

Chapter 2: Methods

2.1/ General Cell Culture

Cells were grown in Dulbecco's Modified Eagle Medium (DMEM) supplemented with 10% heat-inactivated fetal bovine serum (FBS), 10,000 units/mL penicillin-streptomycin, and L-glutamine (200 mM). All reagents were purchased from Invitrogen, UK. Once confluent, cells are washed twice with warm phosphate buffer solution (PBS). Warm trypsin (0.5 % ethylenadiaminetetraacetic acid, 1.5 mL), was added and incubated for 3-5 min. The flasks were tapped to detach the cells. Medium (8.5 mL) was added and the cell solution was transferred to a centrifuge tube before centrifugation at 2000 x g for 4 min. The medium was aspirated and the pellet was resuspended in medium (10 mL). Depending on the desired dilution, cells were transferred to a new corning flask containing fresh medium and incubated at 5 % CO_2 and 37°C.

2.1.1/ Haemocytometry

For specific cell plating experiments, cells were trypinised, centrifuged, resuspended in medium and counted with a Bright Line™ haemocytometer. The concentration of the cells was determined using the equation below:

$$C = \frac{N}{Q} \times 2x10^4 \qquad \textit{equation 2.1}$$

whereby: C = cell concentration (cells/ mL), N = number of cells, Q = number of quadrants counted. For hypoxia experiments, cells were plated in T150 cell culture flasks so that the final total cell count was $2.5x10^7$. For SERS experiments, approximately 75,000 cells in 2 mL media were seeded in one well of a 6-well plate.

2.2/ Nanoshell (NS) Functionalisation

2.2.1 AQ-NS

NS (2.2 x 10^9 particles/mL, 3.65 pM) were functionalised overnight with bis-(2-anthraquinone carboxamide) (AQ) (1-2 mg) in 1% DMSO at room temperature. Functionalised AQ-NS were washed three times with water. NS were purchased from Nanospectra Biosciences. To confirm functionalization, UV-Vis analysis, using a Varian Carey 50 Bio UV/Vis Spectrophotometer, was performed between 200 and 900 nm. Once functionalised, an initial UV-Vis spectrum was taken of the nanosensors. This solution was then spun down for 10 min at 2000 x g and washed twice with TC water. After the second wash, the solution was made up to 1 mL with TC water and another UV-Vis measurement was taken to check for purity and NS concentration. A UV-Vis spectrum of unfunctionalised NS (peak absorbance at ~780 nm) was used as a reference to ensure the nanosensors had red-shifted due to functionalization.

2.2.2 MBA-NS

NS (2.2 x 10^9 particles/mL, 3.65 pM) were functionalised overnight with *para*-mercaptobenzoic acid (MBA) (1-2 mg) in 100% ethanol at room temperature. Functionalised MBA-NS were washed three times with water. NS were purchased from Nanospectra Biosciences. To confirm functionalization, UV-Vis analysis, using a Varian Carey 50 Bio UV/Vis Spectrophotometer, was performed between 200 and 900 nm. Once functionalised, an initial UV-Vis spectrum was taken of the nanosensors. This solution was then spun down for 10 min at 2000 g and washed twice with TC water. After the second wash, the solution was made up to 1 mL with TC water and another UV-Vis measurement was taken to check for purity and NS concentration. A UV-Vis spectrum of unfunctionalised NS (peak absorbance at ~780 nm) was used as a reference to ensure the nanosensors had red-shifted due to functionalization.

2.3/ SERS Measurements

In preparation for Raman analysis, approximately 75,000 cells were plated on a $MgCl_2$ dish placed in a well of a 6-well plate and incubated overnight at 37 °C and 5 % CO_2. The next day, growth media was removed and the cells were washed twice with PBS before adding serum-free media (2 mL). Functionalised NS (200 fM) were added and incubated overnight. The next day, medium was removed and the cells were washed twice with PBS. The $MgCl_2$ dish was removed from the well and inserted into a homemade imaging device, the construction of which is described in Chapter 6. Fresh media was injected into the device until all air bubbles were removed. A Renishaw inVia Raman Microscope and Spectrometer equipped with a 785 nm diode laser in line focus was used for obtaining SERS spectra. A map of a cell (step size of 1 μm) was analysed using 1 s acquisition times at 10 % laser power and a 20x objective. The spectra were then processed using in-house Matlab scripts as described in [62].

2.4/ Metabolite Extraction for NMR

Cells were prepared using method 2.1 and incubated at 1, 2, 3, 4 or 21 % pO_2 from second day of experiment. T150 cell culture flasks were plated for each condition including a control which contained no cells. After the second night of incubation, the cells ($2.5x10^7$) were washed twice with ice-cold PBS (10 mL). MeOH:$CHCl_3$:H_2O (1:1.5:0.7 mL) was added before vortexing for 60 s. All samples were centrifuged at 1000 x g for 5 min. The aqueous layer was pipetted into a plastic vial and the solvent was removed under nitrogen. The polar extracts were resuspended in pH 7.4 sodium phosphate buffer (0.1 M, 600 μL) containing 100 % D_2O, to minimise variations in pH, and TSP (50 nM) as a reference.

2.4.1 NMR Processing

Acquisition of NMR spectra. Samples were run on a Bruker Advance 600 MHz spectrometer. Topspin 2.1 was used to acquire spectra using software implementation of digital filters, which produced flat baselines but resulted in the reduction of the

signal-to-noise ratio by 25 %. Relaxation and acquisition times of 2 s and 1.36 s, respectively, and a NOE mixing time of 10 ms were used. Pulsed field gradients were set to 50 % and -10 % of 50 Gauss/cm. 356 scans were accumulated into each spectrum. The spectra were acquired in automation using home written AU programmes which optimised the homogeneity of the external magnetic field gradient shimming of *z* corrections. The programmes found the resonance frequency of water and calibrated the ^{1}H 90° pulse.

Spectra processing. Spectra were zero filled once and exponential line broadening (0.3 Hz) was applied before Fourier Transformation. Only zero order phase correction was used to phase the spectra. Spectral regions from δ 10.0 to 0 ppm were analysed. Standard baseline and phase corrections (MestReNova) were applied. The spectra were aligned using inbuilt peak alignment before integrating to a predetermined integral list. Regions δ 4.7 – 4.8 ppm containing the residual signal of water, δ 3.35 ppm methanol and δ 7.7 ppm chloroform were not integrated in all samples. Spectral resonances were assigned according to the literature and HMDB. The integrals of each spectrum were normalised to the spectrum with the largest total integral intensity.

2.5/ Metabolite Extraction for MS

The same protocol as the aqueous phase extraction was followed. The organic phase was transferred to a glass tube and the solvent removed under nitrogen. The samples were redissolved in analytical grade $CHCl_3$:MeOH (250:500 μL) and analysed using a solariX FT-ICR mass spectrometer equipped with a 12 Tesla superconducting magnet and an ESI/MALDI Dual Ion Source (BrukerDaltonics, Bremen, Germany) in both positive and negative modes. 20 scans for each sample was taken and averaged. Peaks in the experimental mass spectra were first processed using DataAnalysis™ version 4.4 (BrukerDaltonics, Bremen, Germany). Mass spectra were externally calibrated using ESI Tuning Mix (Sigma-Aldrich) and then internally calibrated to monoisotopic masses of: 678.50683, 692.52248, 703.57485, 706.53813, 718.53813,

720.55378, 732.55378, 734.56943, 746.56943, 758.56943, 774.60073, 786.60073, 813.68440 *m*/*z*. Molecular formulae were determined manually using the SmartFormula algorithm in DataAnalysis™ 4.4 (BrukerDaltonics, Bremen, Germany). Peaks greater than 1% (relative intensity) from *m*/*z* 650 to 850 in each mass spectrum were used in online search tools (LIPID MAPS Structure Database) with a mass tolerance of ±0.001 Da for $[M + H]^+$, $[M + Na]^+$ or $[M + K]^+$.

2.6/ RNA Extraction

Cells were prepared using method 2.1 and incubated at 1, 2, 3, 4 or 21 % pO_2 from second day of experiment. For each pO_2, triplicate T150 cell culture flasks were seeded to a total density of $2.5x10^7$. Total RNA was isolated using miRNeasy Mini Kit (Qiagen) with DNase digestion according to the manufacturer. The quality and quantity of RNA was assessed using the NanoDrop 2000 (Thermo Scientific), ensuring spectrophotometric ratios of $A_{260\ nm}/A_{280\ nm}$ ~2 and $A_{260\ nm}/A_{230\ nm} \geq 2$. A Bioanalyser 2100 Nano LabChip kit (Agilent Thechnologies) was used to determine the integrity of the RNA. Only samples with a RIN≥8.0 were selected for the study. Before submitting the samples to Edinburgh Genomics for RNA-sequencing, a collaborator, Paul Dickinson, made a pool of 15 small RNA libraries using TriLink's CleanTag™ technology (TriLink BioTechnologies, San Diego, USA).

2.7/ ROS measurements

For each pO_2, five T75 cell culture flasks were seeded to a total density of $3x10^6$. Cells were prepared using method 2.1 and incubated at 1, 2, 3, 4 or 21 % pO_2 from second day of experiment. After adding fresh media after centrifugation, H_2DFFDA (10 μM) was added to four of the samples. H_2O_2 (0.03%) was added to one sample and one was left untreated of both reagents. All samples were covered with foil and incubated for 1 h at 37°C and a set pO_2. After incubation, the samples were centrifuged for 4 min at 2000 x g before being washed twice and resuspended in PBS (5 mL). Fluorescence

measurements were taken using a Jobin Yvon Spex Fluoromax spectrofluorometer. The peak emission of H_2DFFDA is ~525nm.

Chapter 3: NMR and Chemometric Analysis of Aqueous Phase Metabolites

3.1/ Introduction

Metabolomics has been increasingly recognised as a valuable methodology to aid in the understanding of disease and toxicity. It is the comprehensive study of endogenous low molecular weight metabolites and their role in biochemical networks and pathways. Metabolomics is an attractive tool for research and clinical studies due to several reasons. Firstly, for its ease of preparation of plasma, tissue, urine and serum samples, circumventing the need for specialist preparations for protein and genome sequencing. Secondly, a perturbation in the tissue environment can elicit a rapid response in the metabolome compared to hours for the transcriptome, for example.[63]

In cancer research, tumour heterogeneity is a major issue for targeted drug therapy; metabolomics, however, can help in deviating away from the "one-size fits all" approach to personalised medicine by identifying which patients are likely to respond well to a drug or will experience toxic effects. Metabolomics can identify potential new biological targets and provide greater insight into the modes of action of drugs in the hope to improve the efficiency and efficacy of radio- and chemo-therapy.[12], [64]

Extraction of intracellular metabolites requires the following steps: (1) quenching of metabolism; (2) cell disruption; (3) hydrophilic and hydrophobic metabolite separation; (4) solvent removal. Previous work conducted on several procedures highlighted that extraction via MeOH:$CHCl_3$:H_2O was the most efficient in obtaining the best data by spectroscopic and chromatographic techniques.[65]–[67] This method was, therefore, adopted in this work.

The high throughput analysis associated with metabolomic studies means that they benefit from visualisation software to interpret the complex multivariate data sets of nuclear magnetic resonance (NMR) and mass spectrometry (MS) spectra. The differential diagnosis between diseased and healthy samples is important to identify the early onset of disease to better improve treatment. Principal Component Analysis (PCA), a chemometric analytical tool, is a widely used multivariate technique in metabolomics to detect metabolic profile perturbations in many disease models such as Alzheimer's disease[66], arthritis[68] and cancer[69]–[71]. PCA examines inherent clustering and patterns within the data by transforming a numerical data set to a new coordinate system. It transforms an original set of correlated variables into a new set of uncorrelated variables, known as principal components (PCs), with the aim to reduce the dimensionality of the data. Once the dimensionality of the NMR and MS data is reduced, the new plots generated are known as scores. Sample points on the scores plot which cluster together have similar properties - as in particular metabolite concentrations increase/decrease to the same extent - whereas those far from each other are dissimilar. The goal is to find a way to represent high dimensional data by a projection into a small dimensional subspace, without losing the important features of the data. PCA, however, has limitations in that it is biased and swayed by metabolites present in higher concentrations. But highly abundant metabolites are not necessarily biologically important; some metabolites are highly regulated whilst others are highly expressed but do not actually affect the phenotype. PCA assumes that expression of metabolites, for example, follows a multivariate normal distribution.[72]

One tool that has recently been utilised to help solve this problem is surprisal analysis (SA). It was first used to analyse energy transfer of non-equilibrated systems but, since 2010, it has been applied to biological systems using thermodynamics and an information-theoretic approach. It transforms high density data, from *omic* studies, into quantifiable information about the disease phenotype state.

3.1.1 Principles of Surprisal Analysis

Any chemical or physical system will tend toward a state of maximal entropy/disorder of minimal free energy. However, most systems are constrained by forces which lower the maximal entropy. For example, using the analogy of a room full of people (Figure 3.1), gravity can be perceived as the largest constraint as it prevents everyone from floating around at maximal disorder with no forces exerted upon them. Another constraint could be that a heater is turned on, creating convection currents which affect the movement of lighter objects. This constraint has little impact on heavier objects but it has still caused a deviation away from a state of maximal entropy to a state of lowered entropy. An unknown force may also push a pen so that it collides with one of the floating people. That person will feel a slight bump in the head but the pen will not drastically change their direction or speed. Maybe not the most scientific of explanations but I hope the reader understands that a system contains constraints that can be ranked in order of how much they lower the entropy of the system.

SA not only identifies and ranks the constraints but also provides, using the same analogy, a snapshot of the distribution of the contents in the room. This is related to Boltzmann's distribution which is a probability distribution of particles in a system existing in different states as a function of energy and temperature, shown in *equation 3.1*:

$$P_i = \frac{e^{-E_i/kT}}{\Sigma_{j=1}^{M} e^{-E_j/kT}} \qquad \textit{equation 3.1}$$

whereby: P_i = the probability of state i; E_i = the energy of state i; k = the Boltzmann constant; T = the temperature of the system; M = the number of all states accessible to the system. I cannot experimentally measure these different states so instead I am looking at concentration changes of metabolites in a biological system.

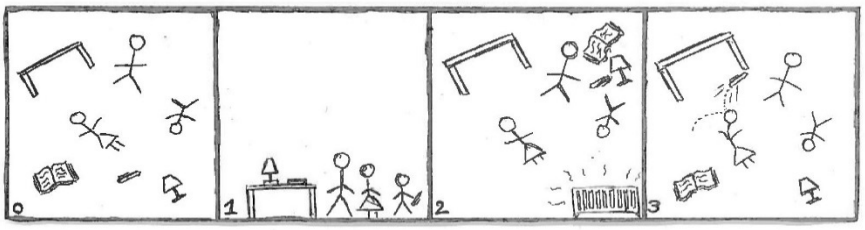

Figure 3.1. Cartoon describing constraints of a system. 0 = balanced state; 1 = addition of constraint 1 (gravity); 2 = addition of constraint 3 (radiator turned on); 3 = addition of constraint 3 (unknown force pushing pen).

Referring back to the gravity constraint, all objects have moved to one face of the room. In the case of the high-speed pen, it has only caused a slight movement of one person and, therefore, the distribution of objects is similar to the non-constrained system (Figure 3.1). The "snapshots" provide information on the free energy changes of each item in the room from a non-constrained to a constrained system. Objects are weightless when gravity is removed but, for simplicity's sake, here we could imagine it takes more energy to move a table to the floor compared to a piece of paper. These changes in energy are also ranked by SA.

In relation to biological systems, these constraints can be thought of as cellular design features like the switch to glycolysis in tumours or activation of signalling pathways. These different molecular constraints represent phenotypes that exist as a profile of, for example, metabolite abundances which can change in response to environmental and/or genetic perturbations. Constraints can also be viewed as cancer signatures or metabolite patterns. SA first determines the thermodynamic reference point referred to as the "balanced state". This is unconstrained system of maximal entropy (*c.f.* the room of objects with no gravity). Here, the state the metabolite levels are not changing and are common to both healthy and diseased patients, i.e. they are needed for the cell to survive. A thermodynamic weight (or free energy change) for each metabolite is assigned and ranked from its deviation from the balance state; the higher the free energy change of a metabolite, the more weight it contributes to each constraint.

The sum of the constraints subtracted from the balanced state equals the logarithm of the experimentally measured expression level of each metabolite, as shown below:

$$InX_i(\mathrm{t}) \quad = \quad InX_i^0 \quad - \quad \sum_{\alpha=1} G_{i\alpha}\lambda_\alpha(\mathrm{t}) \qquad \textit{equation 3.2}$$

whereby: X_i = the experimental expression level of each metabolite i; X_i^0 = the expression of each metabolite in the balanced state; $G_{i\alpha}$ = the weight of each metabolite in each constraint α; $\lambda_\alpha(\mathrm{t})$, the Lagrange multiplier = the size of the entropy reduction due to the constraint α.[73], [74] This equation can be related back to *equation 3.1* as follows:

$$X_i^o = e^{-\lambda_0 G_{i0}} = e^{-\frac{E_i}{kT}} \qquad \textit{equation 3.3}$$

Constraints are not static: they change in response to genetic or environmental perturbation. These changes of state will be reflected in differential abundance in response to a stimulus. The outcome is a compaction of the experimental dataset and extraction of relevant biological information. In this research, aqueous metabolite abundances of cell cultures incubated in a range of states of induced hypoxia were extracted and analysed using ^{1}H NMR. The results were interpreted via SA.

3.2/ Results

Preliminary analysis was conducted on 3 cell lines at 21% and 1% pO$_2$ to identify possible metabolite changes. Figure 3.2 and Figure 3.3 clearly emphasise the fact the cancer-derived cell lines are dissimilar. On observation, breast adenocarcinoma (MCF7) cells grow particularly rapidly compared to androgen-nonresponsive (PC3) and adenocarcinomic human alveolar basal epithelial (A549) cells. In the interest of time, MCF7 and A549 were chosen for further analysis.

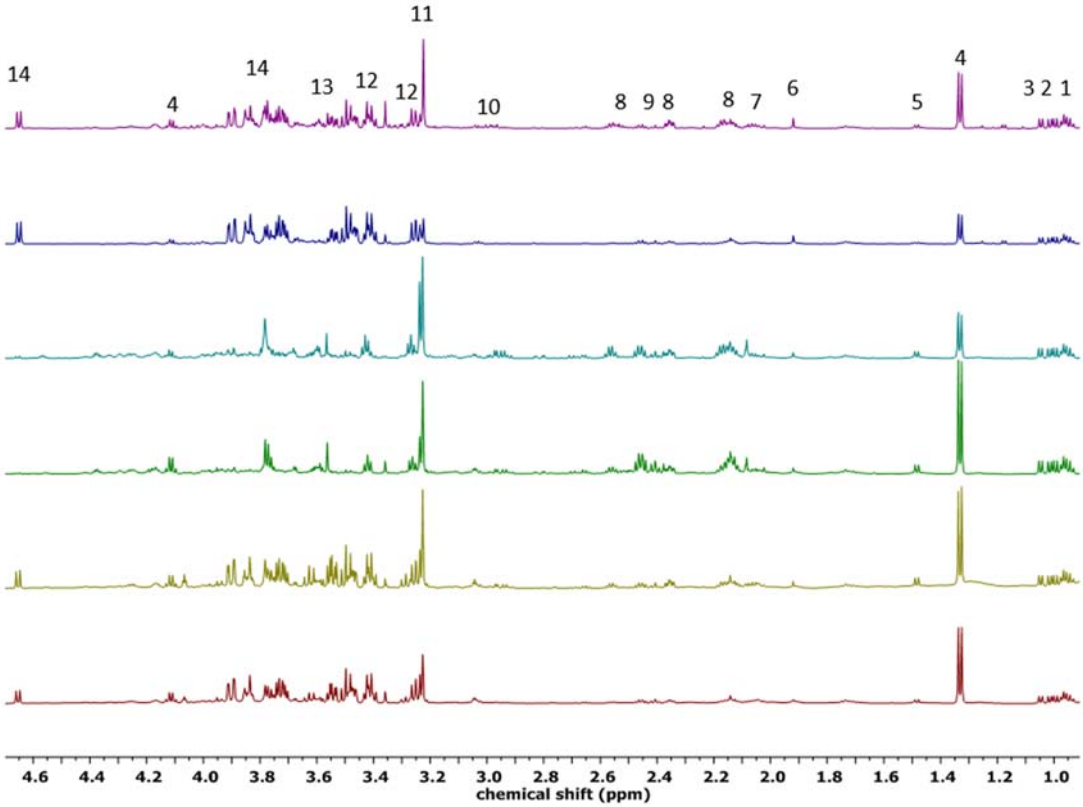

Figure 3.2. Representative ^{1}H NMR of from top: A549 cells at 1% pO_2, 21% pO_2; MCF7 cells at 1% pO_2, 21% pO_2; PC3 cells at 1% pO_2, 21% pO_2 in aliphatic region. 1 - Valine, 2 – Leucine, 3 – Isoleucine, 4 – Lactate, 5 – Alanine, 6 – Acetate, 7 – Pyruvate, 8 – Glutamate, 9 – Glutamine, 10 – GSH, 11 – GPC, 12 – Taurine, 13 – Glycine, 14 - Glucose. Spectra of chemical shift vs. intensity are overlaid on one spectrum.

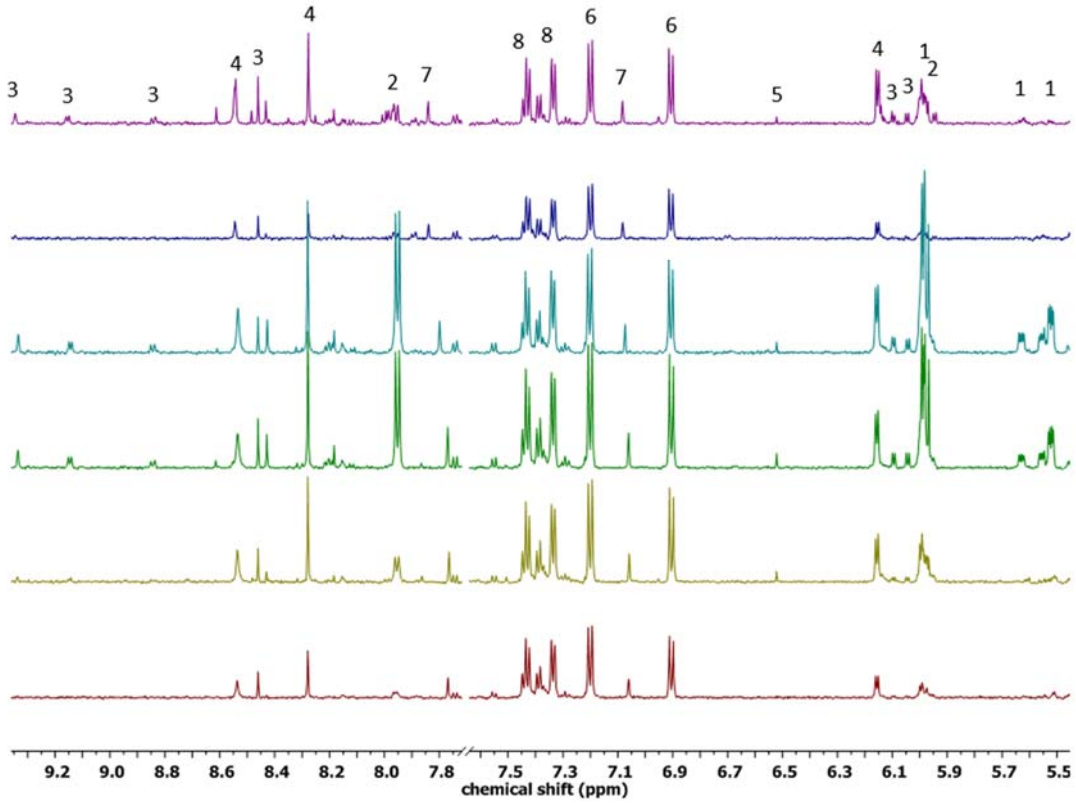

Figure 3.3. Representative ^{1}H NMR of from top: A549 cells at 1% pO_2, 21% pO_2; MCF7 cells at 1% pO_2, 21% pO_2; PC3 cells at 1% pO_2, 21% pO_2 in aromatic region. 1 – Nucleotides, 2 - UDP-glc, 3 – NADH, 4 – ATP/ADP/AMP, 5 – Fumarate, 6 - Tyrosine, 7 - Histidine, 8 – Phenylalanine. Spectra of chemical shift vs. intensity are overlaid on one spectrum.

Many parameters can affect the final NMR spectra: for example, pH, temperature and instrumental affects can cause drifting in the chemical shifts of metabolites. It is, therefore, of paramount importance that the NMR spectra are processed appropriately before inserting into a data analysis tool. MestReNova has an in-built peak alignment tool which was applied after phase and baseline correction (Figure 3.4).

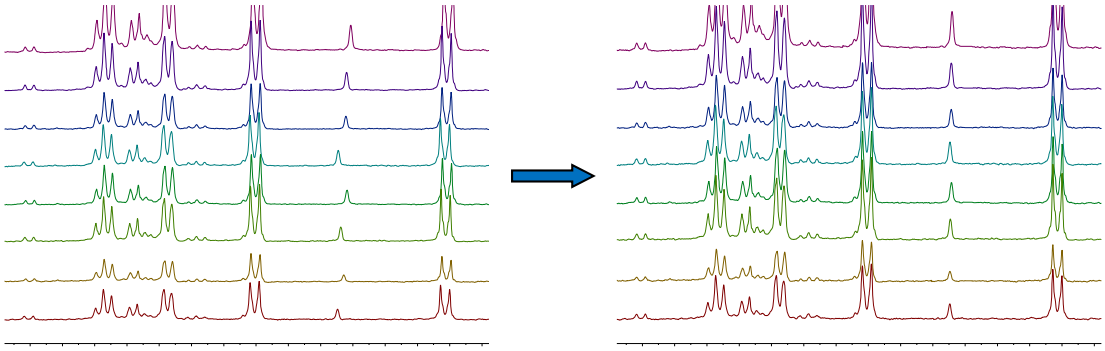

Figure 3.4. Overlapping ^{1}H NMR spectra of intensity vs chemical shift before and after peak alignment.

3.2.1 Metabolic fingerprint analysis of A549 cells

Representative ^{1}H NMR spectra of A549 cell samples at perturbed and normal physiological oxygen concentrations are shown in Figure 3.5 and Figure 3.6. Published literature[75], the Human Metabolome Database (HMDB) and spiked cell samples were used to assign and confirm presence of metabolites. Table 8 (Appendix A) shows the assignment of peaks.

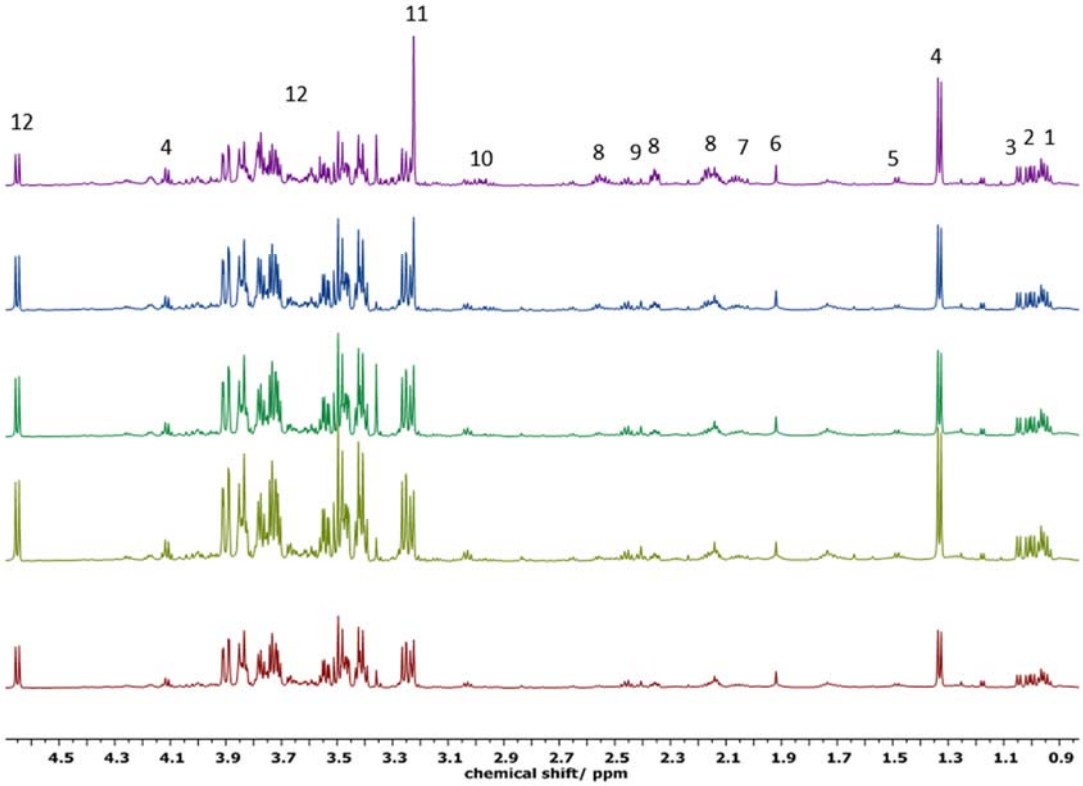

Figure 3.5. Representative ^{1}H NMR spectra comparison of A549 cells cultured under (from top) 21%, 4%, 3%, 2% and 1% pO_2 conditions in aliphatic region. 1 - Valine, 2 – Leucine, 3 – Isoleucine, 4 – Lactate, 5 – Alanine, 6 – Acetate, 7 – Glutamate, 8 – Glutamine, 9 – Succinate, 10 – GSH, 11 – GPC, 12 – Glucose. Spectra of chemical shift vs. intensity are overlaid on one spectrum.

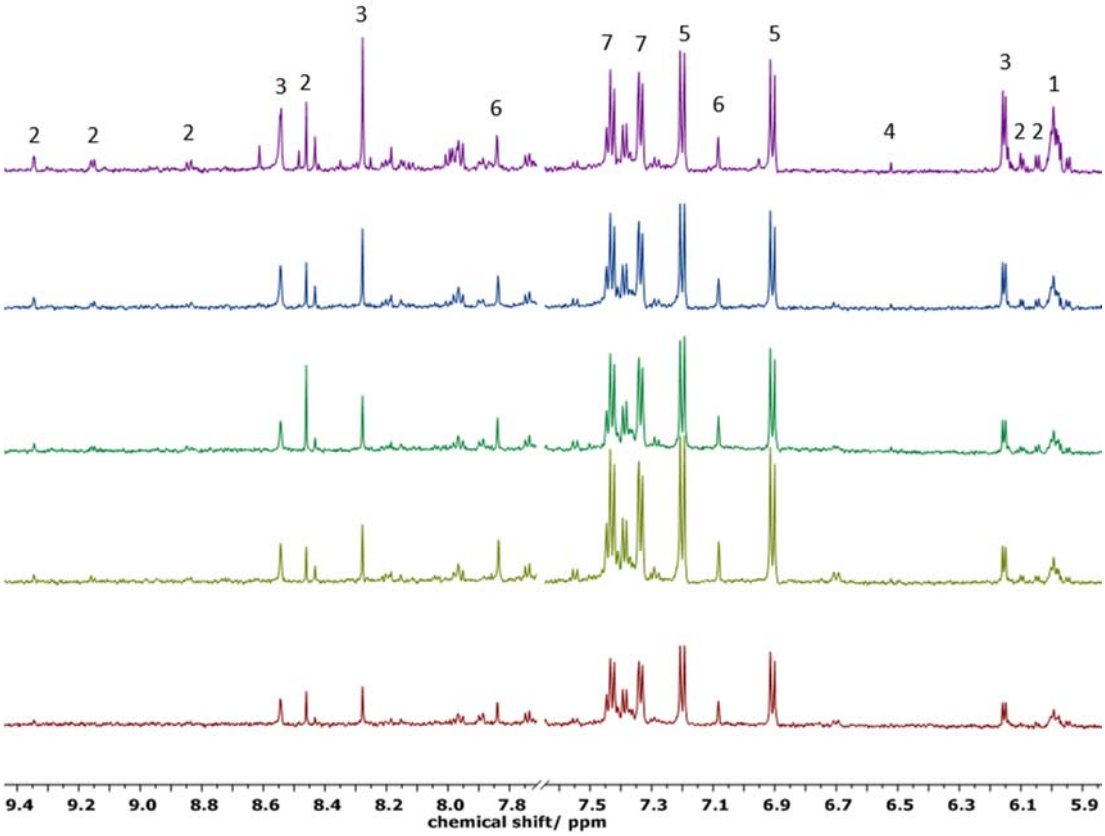

Figure 3.6. Representative ^{1}H NMR spectra comparison of A549 cells cultured under (from top) 21%, 4%, 3%, 2% and 1% pO_2 conditions in aromatic region. 1 – Nucleotides, 2 - NADH, 3 – ATP/ADP/AMP, 4 – Fumarate, 5 - Tyrosine, 6 – Histidine, 7 - Phenylalanine. Spectra of chemical shift vs. intensity are overlaid on one spectrum.

The NMR integrals are represented as matrix X consisting of 5 columns (n) and 89 rows (m): each column contains data for one pO_2 and each row is the average integral number associated with a given metabolite from 10 replicates. There are 89 integrals in total which were normalised by scaling up to the same overall intensity as the spectrum with the greatest total intensity (to take into account cell number differences). The peaks were integrated individually as binning could result in peak overlap. The normalised spectra were averaged for each oxygen condition so that the final matrix of data (nxm) was 5x89. Log scaling was applied to the normalised integrals. Surprisal analysis was conducted on the new matrix which involves singular value decomposition (SVD). This procedure finds the eigenvalues and

eigenvectors of the system which are the sizes and directions of the system's constraints, respectively.

SA was conducted to identify disease signatures and particular metabolites that characterise the phenotypic states at different oxygen concentrations. Each metabolic profile of the 5 conditions is represented as a constraint that prevents the system reaching maximal entropy. SA highlights the fact that distribution is not uniform and reflects the free energy of metabolites. A reference state is first derived whereby metabolite levels do not change with respect to oxygen concentration, thus there is no net change to the system (analogous to identifying housekeeping genes). Phenotypes (collections of metabolites that change similarly with pO_2) which cause a deviation from the reference state are determined and ordered in decreasing importance. Each constraint lowers the entropy from its maximal value, the extent by which is denoted by the Lagrange Multiplier, λ_α. Lagrange multipliers which have small numerical values contain no or little information.

Identification of balanced state:

The balanced state of a system is the reference point whereby all cellular processes are in equilibrium, i.e. there is not net change. The balanced state is invariant of pO_2 and is referred to as the zeroth phenotype, G_{i0}. Metabolites with the lowest free energy are the most stable and contribute most to the balanced state. The equation for the zeroth phenotype, G_{i0}, represents the metabolite expression at the entropic global maximum (*equation 3.4*).

$$InX_i^0 = -\lambda_0 G_{i0} \qquad \textit{equation 3.4}$$

Whereby: G_{i0} = the O_2-independent extent of participation of metabolite i in the balanced state; λ_o = the phenotype of the balanced state.

Identification of constraints:

It is important to decide how many constraints should be chosen to best describe the patterns observed within the dataset using as little information as possible. There are *n*-1 constraints with *n* being the number of oxygen conditions. I have different 5 different oxygen concentrations; therefore, I would have a total of 4 possible constraints to add to *equation 3.2*. If all 4 constraints were added (*equation 3.5*), the entire raw dataset would be regenerated, including any inherent noise within the data because all the information has been used (as shown in Figure 3.7). *Equation 3.3* shows how each constraint, λ, with its corresponding G vectors, dictating free energy changes of each metabolite in the phenotype, are added to give the sum of the system's constraints.

$$\sum_{\alpha=0} G_{i\alpha}\lambda_{\alpha} = G_{89x0}\lambda_0 + G_{89x1}\lambda_1 + G_{89x2}\lambda_2 + G_{89x3}\lambda_3 + G_{89x4}\lambda_4 \quad \textit{equation 3.5}$$

SVD first produces a matrix of dimensions *n*x*n*, ranking the constraints in order of influence with constraint one being the biggest influence on the metabolite pathway transitioning. Referring back to the people in a room analogy, gravity would be constraint one. SA produces plots of the raw dataset versus the addition of one or constraints which are subtracted from the balanced state (refer to *equation* 3.2). As mentioned before, a model with no more than (in this case) two constraints is ideal to alleviate the problems associated with high throughput data such as sample heterogeneity and noise, and to best explain the relative trends in the data with as little raw data as possible. In Figure 3.7, it can be seen that addition of one constraint to the A549 cell model suffices as it produces a relatively straight line, modelling the main characteristics and trends of the experimental data. In biological terms, one or two important dominant metabolite expression patterns is sufficient to quantitatively reproduce the expression levels of all individual metabolites. If all 5 metabolite patterns were computed, a straight line would be observed.

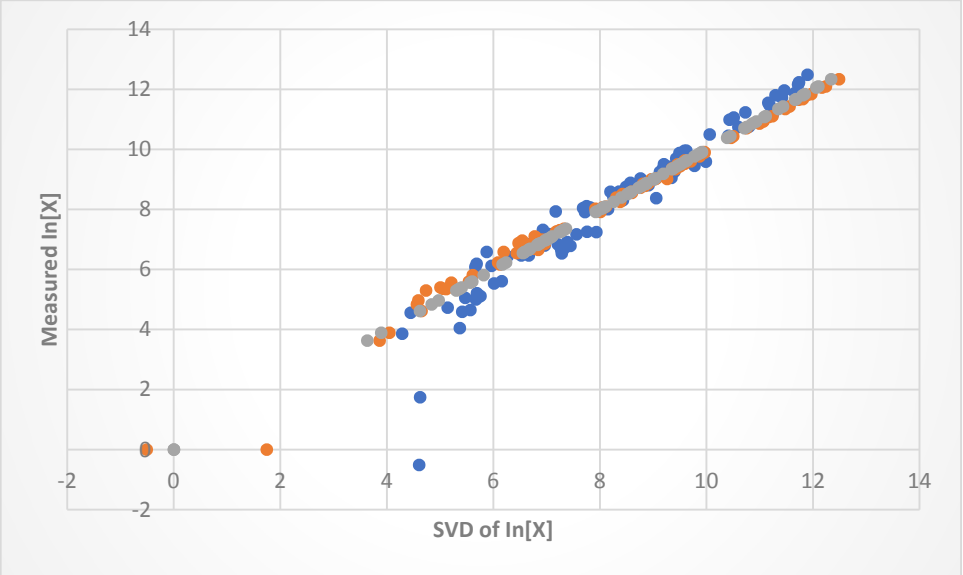

Figure 3.7. Scatter plot of measured metabolite levels vs. computed values of A549 cells. The addition of one constraint (red) and all 4 constraints (green) are modelled with the balanced state (blue).

Identification of discriminatory metabolites:

Another matrix that SVD produces is independent of oxygen concentration which states the order of influence that metabolites have on a particular constraint/phenotype. For each constraint/phenotype, α, a list of the oxygen-independent weights, or free energy changes, of each metabolite, i, is generated. This list describes the "snapshots" previously mentioned of the positions of objects in the room and how much energy is needed to move them. Metabolites that have a free energy change of/close to zero have no impact on this phenotype, whereas those that do change can be either up- or downregulated.

Figure 3.8 shows the G plots with S-shaped curves of the A549 cell model depicting the free energy changes of metabolites as a constraint is added to the system. Metabolites further away from 0 contribute to the response to change in pO_2. When one constraint is added, metabolites with the highest negative free energy are (in descending order of importance): AMP/ADP/ATP, UMP/UDP/UTP, NADH and UDP-glucose (UDP-glc). Two unknown peaks at 1.57 ppm and 6.68 ppm and glucose change in the opposite direction (greatest positive free energy change) to the former metabolites.

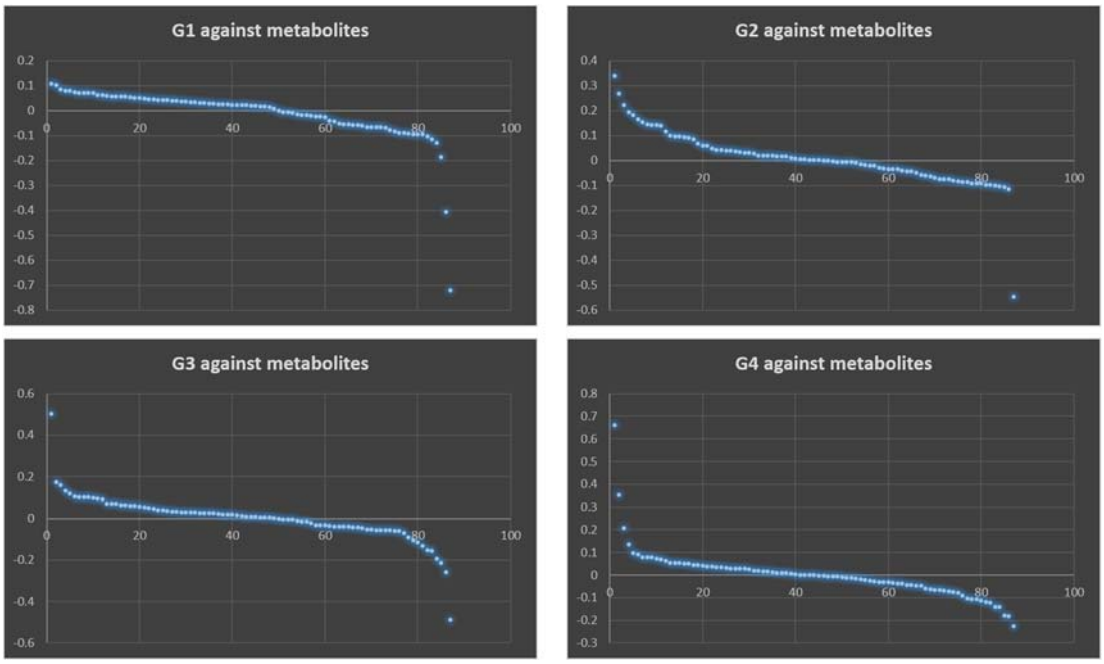

Figure 3.8. G plots of metabolite free energy change from balanced state vs. metabolite number of A549 cells on addition of a constraint.

Figure 3.9 and Figure 3.10 graphically display how some of these discriminatory metabolite concentrations from constraint one change depending on the pO_2. All but glucose appear to follow a similar trend of a sharp increase from 1-2% pO_2 and a decrease from 2-3% pO_2. *P*-values for metabolites of interest can be found in Appendix B.

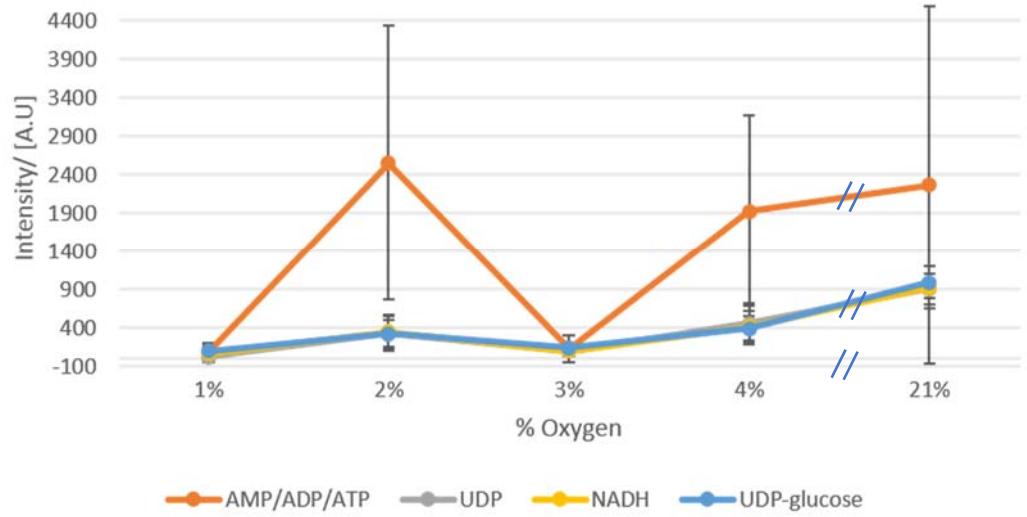

Figure 3.9. Averaged discriminatory metabolite concentration changes at varying pO_2. Error bars of standard deviation of replicates are plotted.

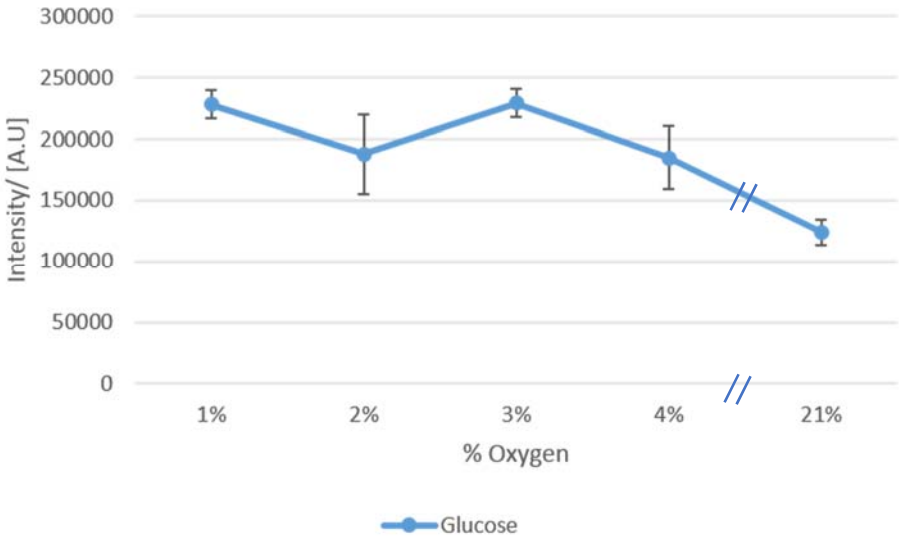

Figure 3.10. Averaged glucose concentration changes at varying pO_2. Error bars of standard deviation of replicates are plotted.

Results obtained from SA were compared to those from PCA using SIMCA-16 software. PCA first mean centres the normalised data and scales it using Pareto which is the mean divided by the square root of the standard deviation. Supervised orthogonal projections to latent structures (O-PLS) was also used and the score plots of the two models are depicted in Figure 3.11 and Figure 3.12. The algorithm of O-

PLS is an extension of the PLS regression method. It uses an orthogonal signal correction filter to pick out variations in the data that are considered to be useful for the prediction of a quantitative response and excludes those that are unrelated/orthogonal to the class response/descriptor variables (X). Doing so decreases the number of predictive components and improves interpretability. Variation in X that is unrelated to Y can cause imprecise predictions for new samples and disturb multivariate modelling. Here, PCA has clustered the majority of the samples cultured at 21% pO_2, which is further enhanced in the OPLS scores plot.

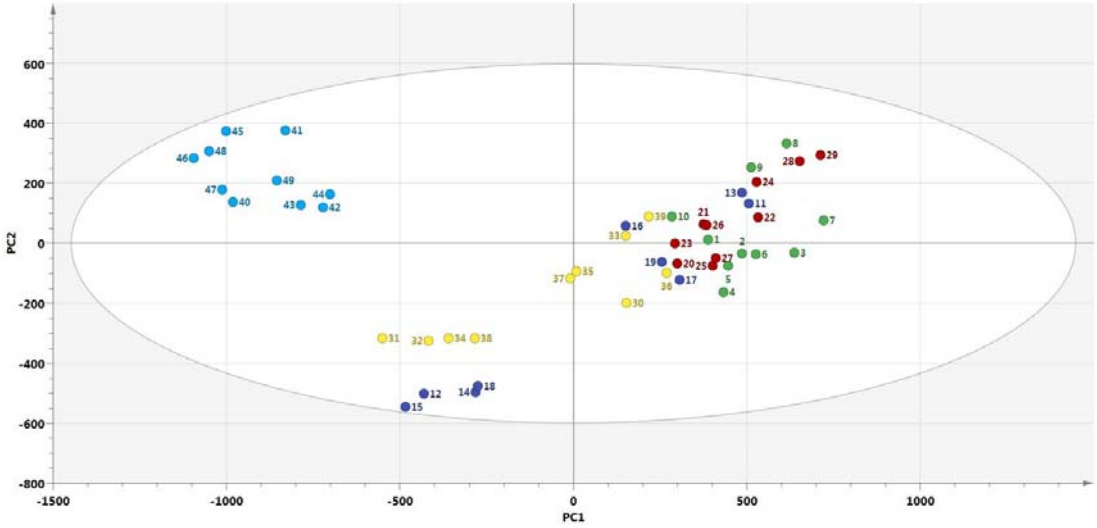

Figure 3.11. PCA score plot of PC1 vs PC2 of A549 cells cultured under 1% (green), 2% (dark blue), 3% (red), 4% (yellow) and 21% (light blue) pO_2.

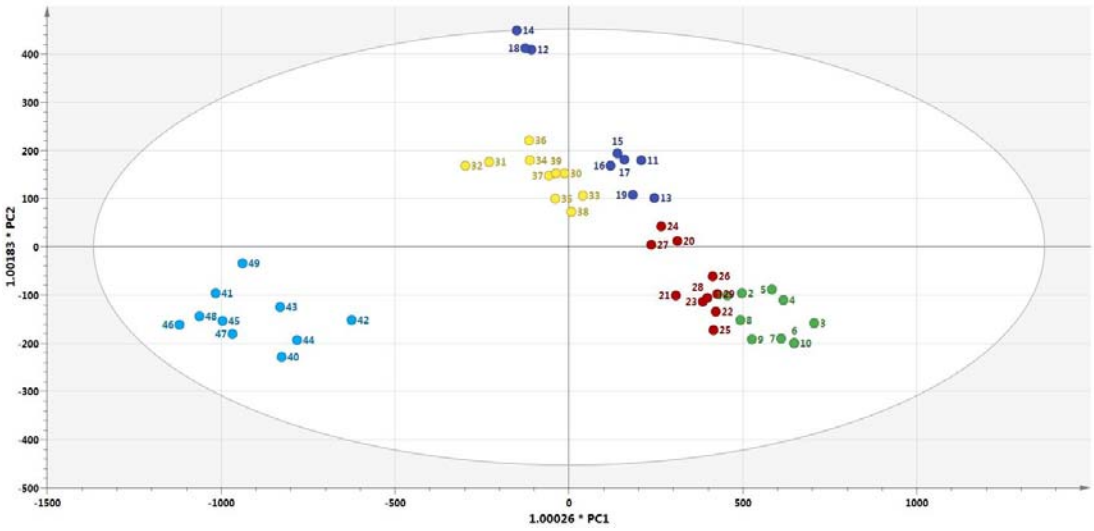

Figure 3.12. OPLS-DA score plot of PC1 vs PC2 of A549 cells cultured under 1% (green), 2% (dark blue), 3% (red), 4% (yellow) and 21% (light blue) pO_2.

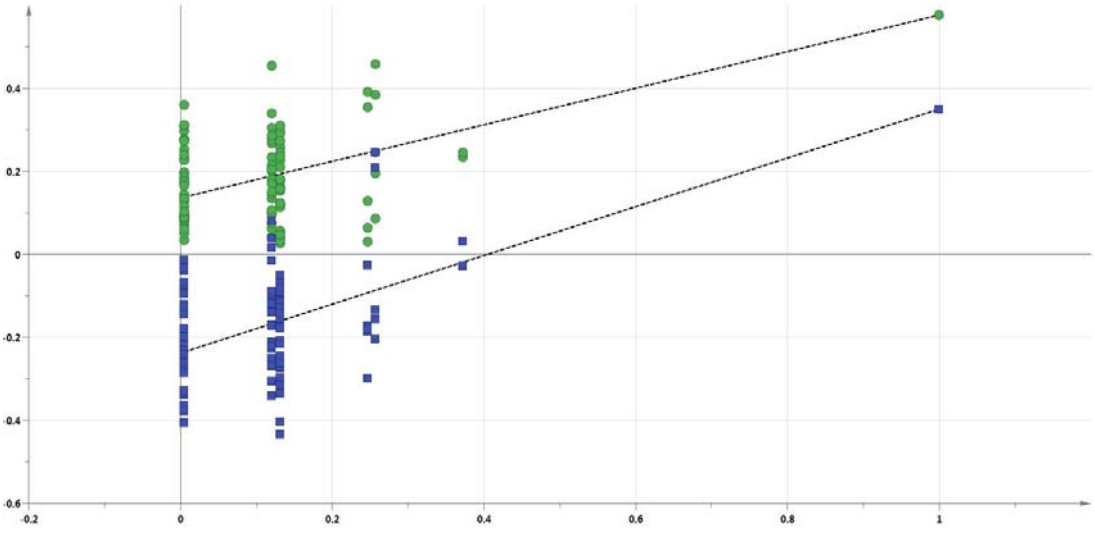

Figure 3.13. Permutation test of A549 cell line.

Q^2 and R^2X provided an estimation of the predictive power and goodness of fit of the models, respectively. Models with Q^2 and R^2X values over 0.9 are considered 'excellent'. A permutation test was conducted to test the validity and degree of over-fit of the model. 100 permutations were calculated, meaning that the sample class was randomly permuted while keeping the X matrix intact. For the model to be regarded

as robust, Q^2 of the original model must be equal to or higher than the maximum value of Q^2_{max} from the randomly permuted data and the blue Q^2 regression line must intersect the vertical at or below zero. The permutation test revealed positive slopes with a Q^2_{max} of 0.35 which is lower than the original model (R^2 = 0.90 and Q^2 = 0.36), indicating a good predictive model. The permuted data also has a R^2 of 0.56, suggesting the original PLS-DA model is not over-fitted (Figure 3.13).

The loadings plot (Figure 3.14) has identified the following metabolites in order of importance for explaining the variance observed in the scores plot: glucose, phosphocholine, valine, isoleucine, leucine, and glutamine. These findings are different to those obtained from SA. It is perhaps the result of some metabolites present in high concentrations skewing the variation in the scores plots. These metabolites may not actually affect concentrations of other metabolites and the overall pO_2-dependent phenotype but it is their large fold change that PCA is identifying as discriminatory metabolites.

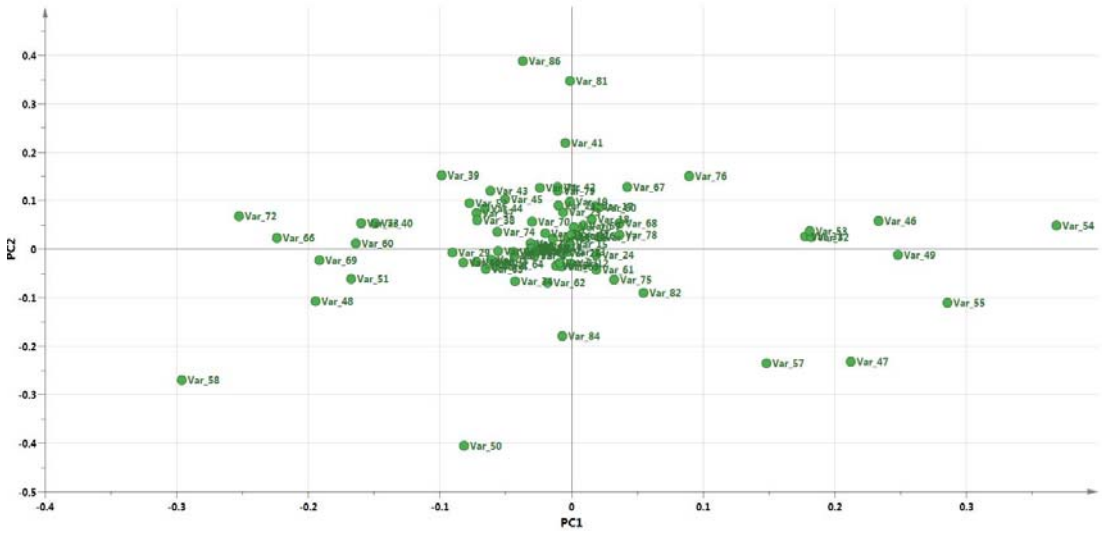

Figure 3.14. Loadings plot of PC1 vs PC2 of A549 cell ^{1}H NMR integrals. Points further away from the origin explain no/very little of the variation shown in the scores plot

3.2.2 Metabolic footprint analysis of A549 cells

By looking at the metabolic fingerprint alone (i.e. intracellular metabolites), it is difficult to know if an increase in a metabolite level is due to its increased production or increased uptake from the media. The metabolic footprint (i.e. extracellular metabolites) was, therefore, measured to help answer a few questions. Figure 3.15 and Figure 3.16 compare media taken from A549 cells cultured under 1% and 21% pO_2 to control media which is not derived from cells. Lactate, interestingly, pyruvate, fumarate and formate are present in higher concentrations at 21% O_2.

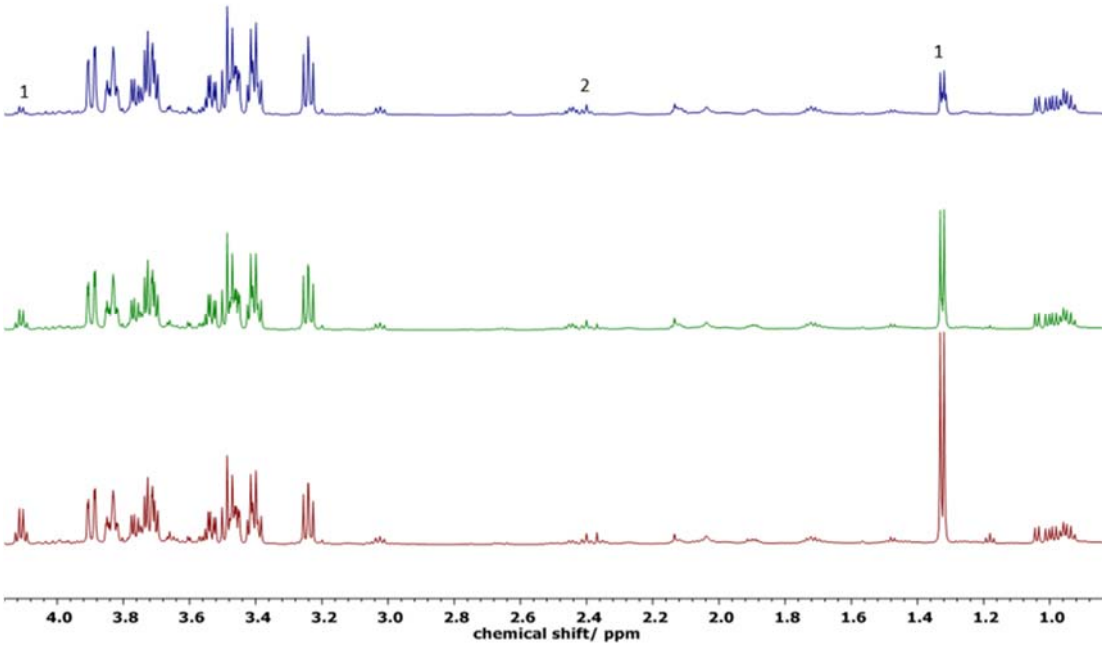

Figure 3.15. Representative ^1H NMR spectra of A549 footprint collected from media of cultured cells in 21% (red) and 1% (green) pO_2 and control media (blue). Labelled metabolites that change in concentration are: 1 - Lactate, 2 – Pyruvate. Spectra of chemical shift vs. intensity are overlaid on one spectrum.

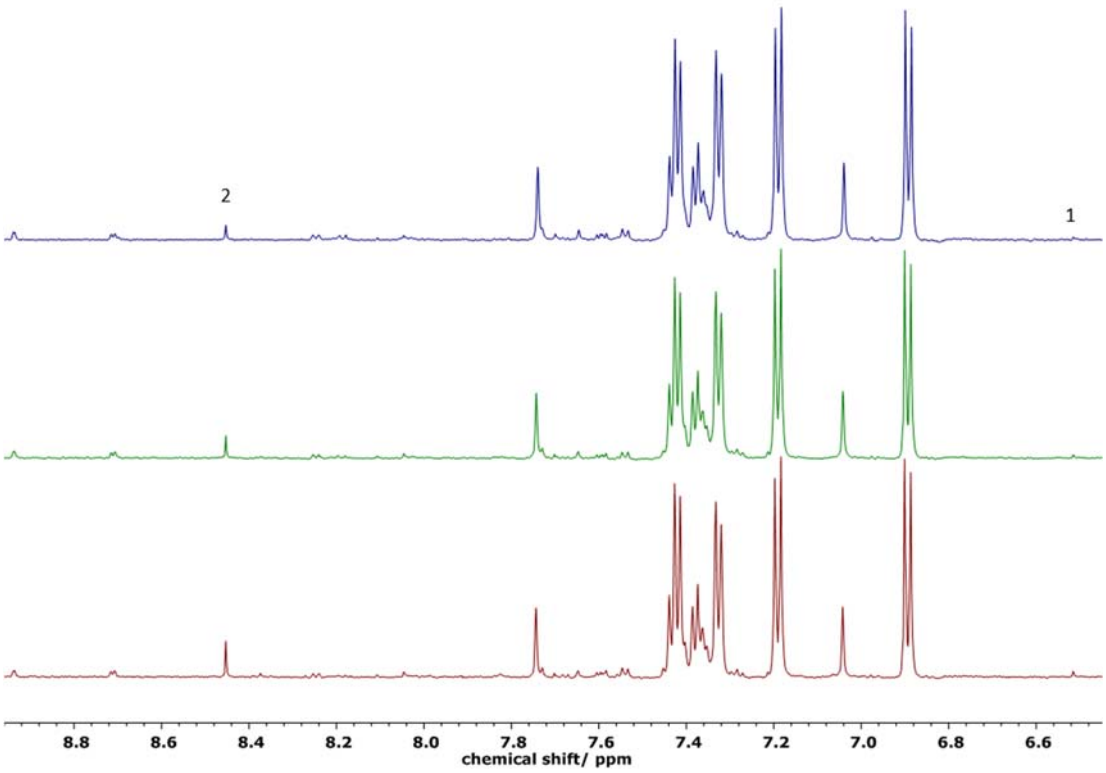

Figure 3.16. Representative ^{1}H NMR spectra of A549 footprint collected from media of cultured cells in 21% (red) and 1% (green) pO_2 and control media (blue). Labelled metabolites that change in concentration are: 1 - Fumarate, 2 – Formate. Spectra of chemical shift vs. intensity are overlaid on one spectrum.

3.2.3 Metabolic fingerprint analysis of MCF7 cells

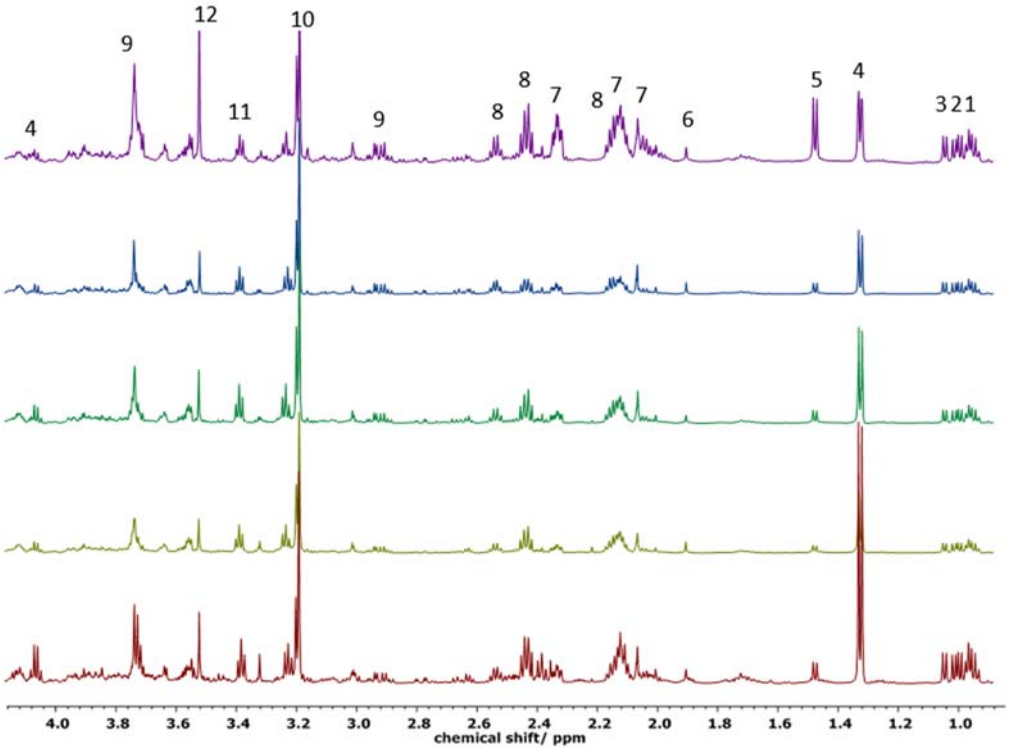

Figure 3.17. Representative ^{1}H of MCF7 cells, cultured under (from top) 21%, 4%, 3%, 2% and 1% pO_2 conditions, in aliphatic region. 1 - Valine, 2 – Leucine, 3 – Isoleucine, 4 – Lactate, 5 – Alanine, 6 – Acetate, 7 – Glutamate, 8 – Glutamine, 9 – GSH, 10 – GPC, 11 –Taurine, 12 - Glycine. Spectra of chemical shift vs. intensity are overlaid on one spectrum.

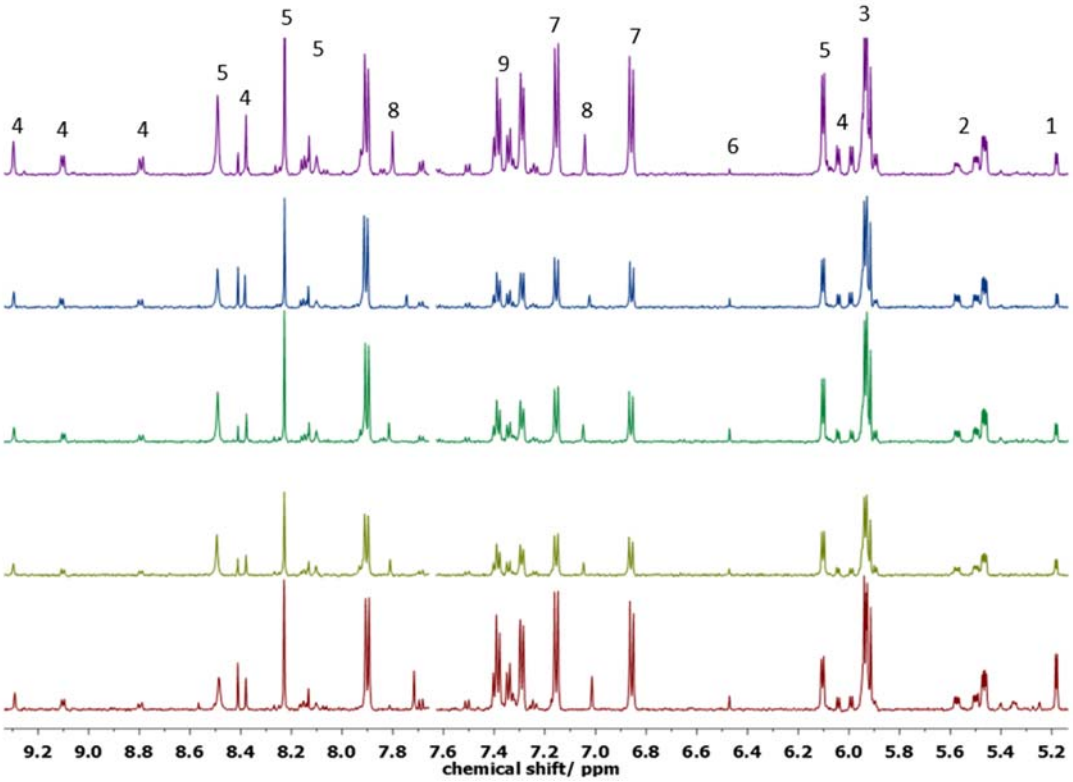

Figure 3.18. Representative ^{1}H of MCF7 cells, cultured under (from top) 21%, 4%, 3%, 2% and 1% pO_2 conditions, in aromatic region. 1 – Glucose, 2 – Nucleotides, 3 – UDP–Glucose, 4 – NADH, 5 – ATP/ADP/AMP, 6 – Fumarate, 7 – Tyrosine, 8 – Histidine, 9 – Phenylalanine. Spectra of chemical shift vs. intensity are overlaid on one spectrum.

On addition of one constraint, the following positively identified metabolites with the biggest contribution to the phenotype (in descending order) in terms of positive free energy changes were: glucose, lactate, taurine, fumarate, glutamine, unknown (8.45 ppm), histidine, and acetate. Metabolites with the greatest negative free energy changes were: alanine, glycine, glutamate, tyrosine, unknown (4.22 ppm), NADH, and phenylalanine. *P*-values for metabolites of interest can be found in Appendix B.

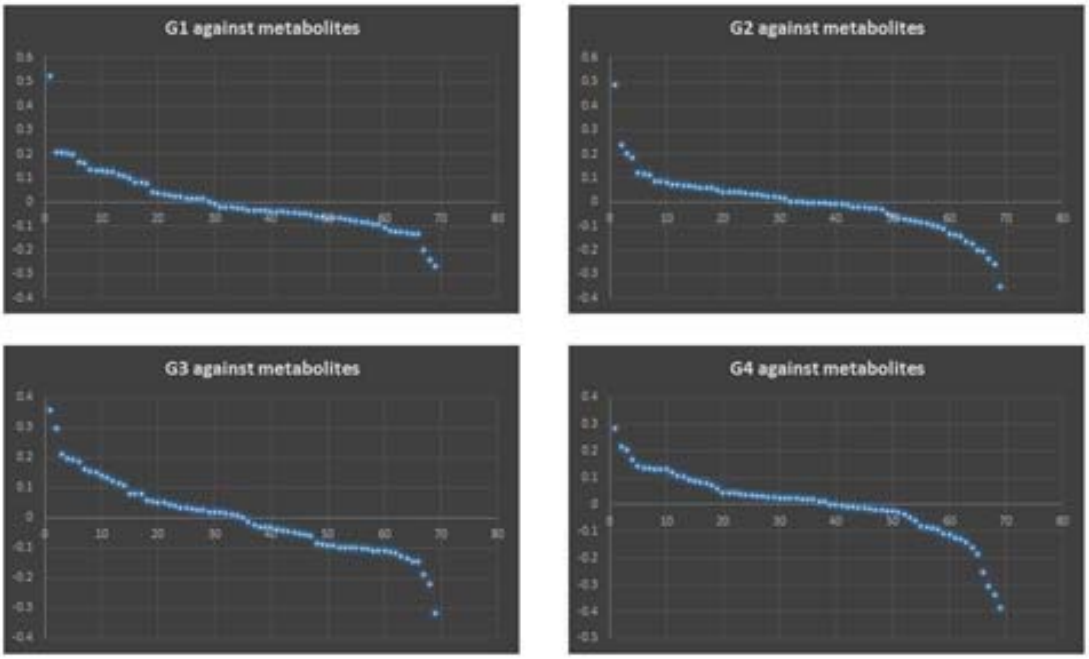

Figure 3.19. G plots of free energy change from balanced state of metabolites vs. metabolite number of MCF7 cells on addition of a constraint.

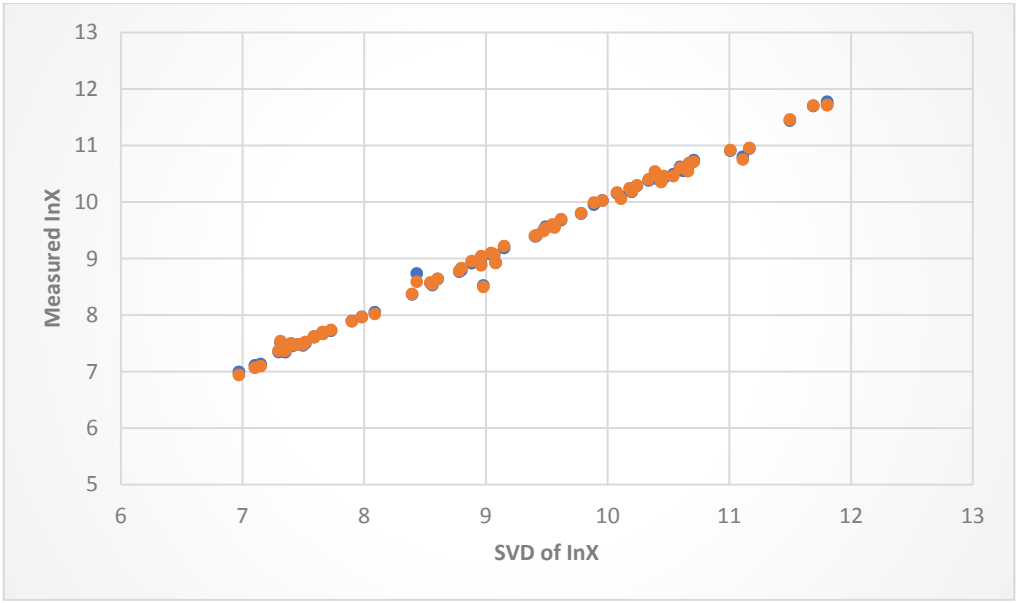

Figure 3.20. Scatter plot of measured metabolite levels vs. computed values of MCF7 cells. The addition of one constraint (red) is modelled with the balanced state (blue).

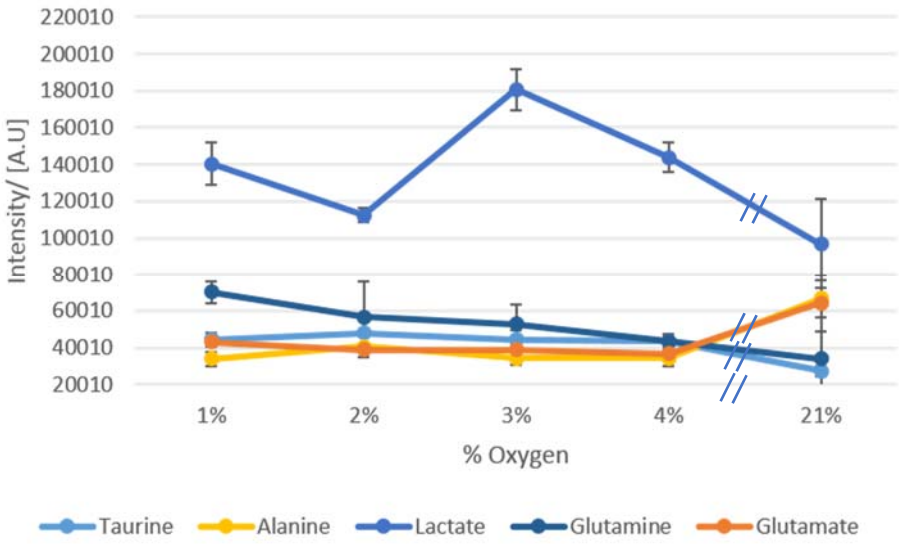

Figure 3.21. Graph plotting normalised MCF7 metabolites of interest from SA. Error bars showing standard deviation of replicates are shown.

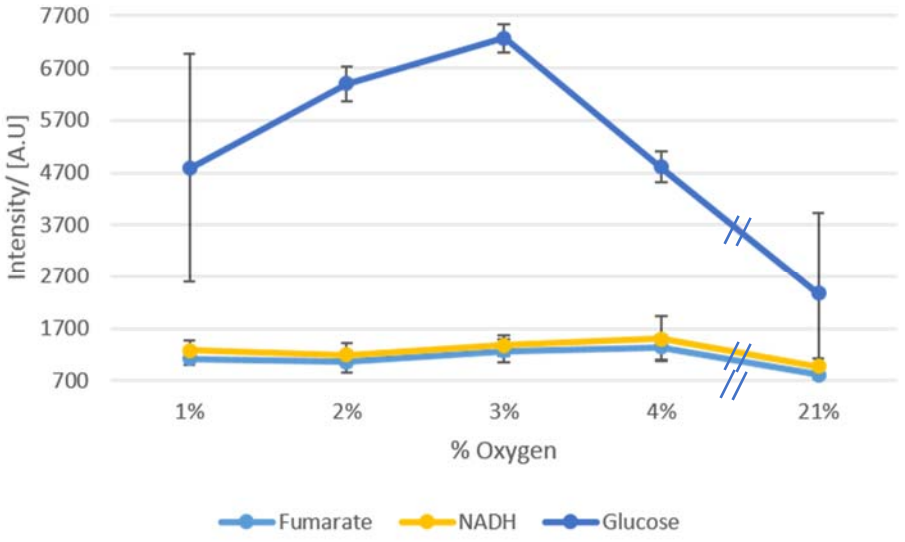

Figure 3.22. Graph plotting normalised MCF7 metabolites of interest from SA. Errors bars showing standard deviation of replicates are shown.

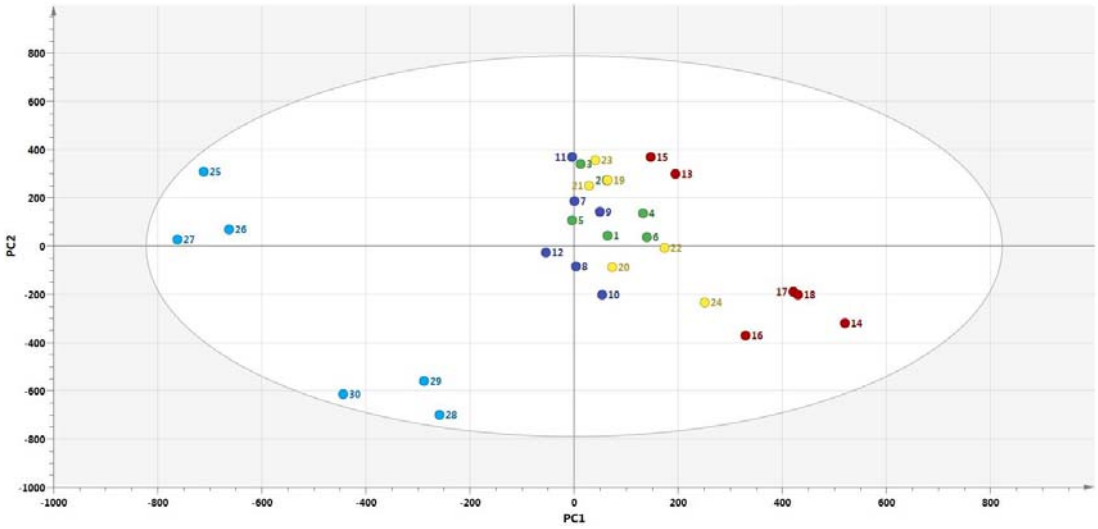

Figure 3.23. PCA score plot of MCF7 cells cultured under 1% (green), 2% (dark blue), 3% (red), 4% (yellow) and 21% (light blue) pO_2.

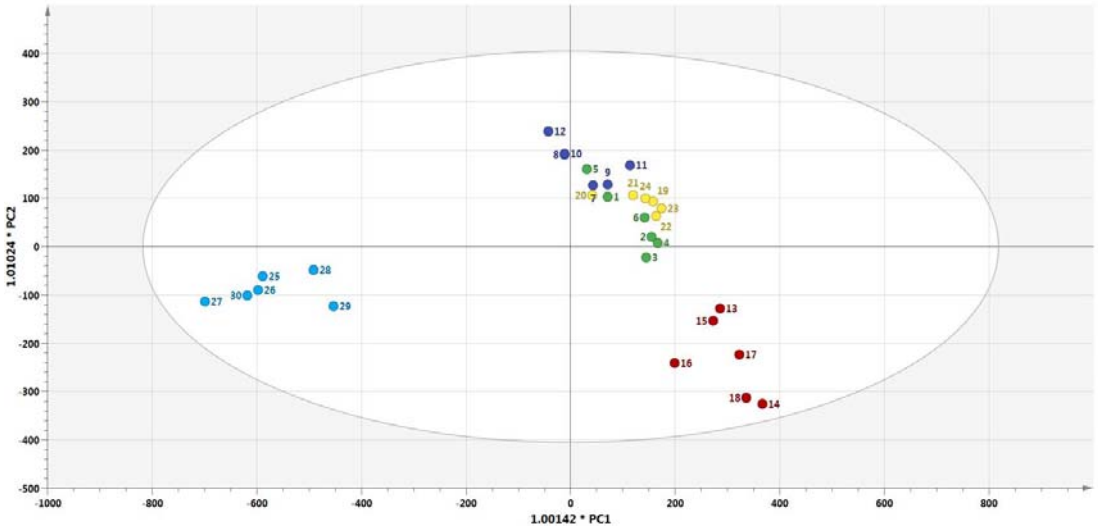

Figure 3.24. OPLS-DA score plot of MCF7 cells cultured under 1% (green), 2% (dark blue), 3% (red), 4% (yellow) and 21% (light blue) pO_2.

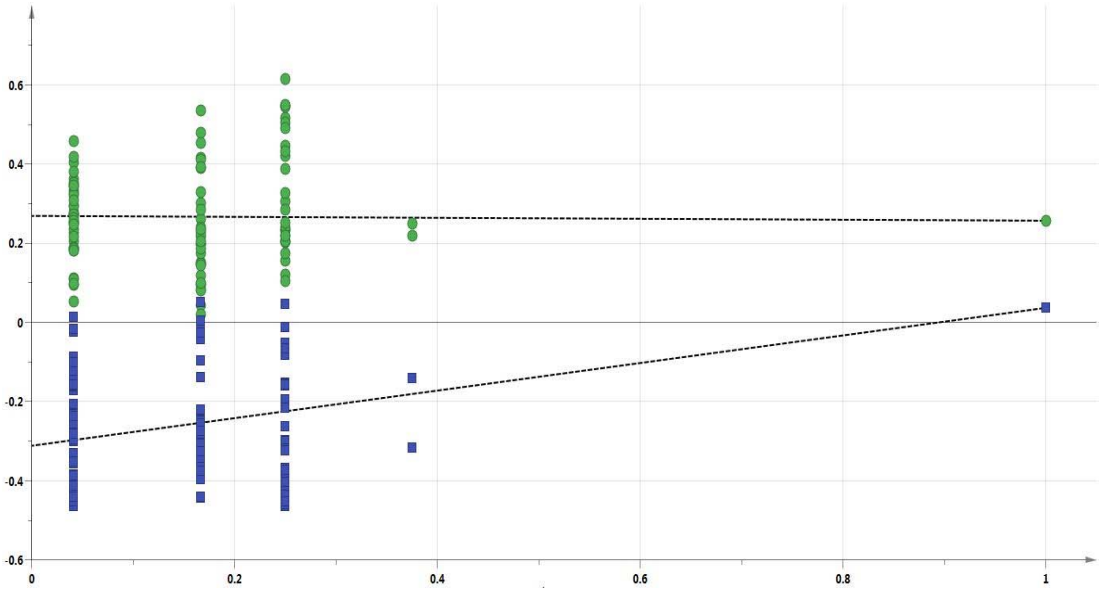

Figure 3.25. Permutation test of MCF7 cell line.

The permutation test (Figure 3.25) revealed slightly positive slopes with a Q^2_{max} of 0.03 which is lower than the original model (R^2 = 0.76 and Q^2 = 0.44). However, Q^2 is still low, indicating a poor predictive model. The permuted data also has a R^2 of 0.26, suggesting the original PLS-DA model is poorly fitted.

PCA (Figure 3.23) shows some clustering of cells cultured at 1-4% pO_2; however, supervised analysis (Figure 3.24) separates cells cultured under 3% and 21% from the remaining sample set. Metabolites of interest in descending order of importance are lactate, an unknown metabolite (3.03 ppm), glutamine, an unknown metabolite (2.07ppm), aliphatic amino acids, alanine, glutamate, glycine, taurine, an unknown metabolite (2.55ppm) and UMP/UDP/UTP. A TCOSY spectrum was run to try identify any unknown peaks but, unfortunately, the resolution was very poor – there was merging of many cross peaks of coupled protons. Mass spectrometry could, therefore, be used in future work.

3.2.4 Metabolic footprint analysis of MCF7 cells

Figure 3.26 depicts that, due to the high proliferative rate of these cells, it is not surprising glucose concentrations were barely detected compared to the control media. Increased levels of lactate, glutamine and pyruvate were present in the media of cells cultured at 1% pO_2. In cells cultured under 21% pO_2, glutamine was not detected and fewer amino acids (less so than hypoxic cells) were present compared to the control. Furthermore, it can be seen from Figure 3.26, formate is double the concentration compared to both hypoxic cells and the control.

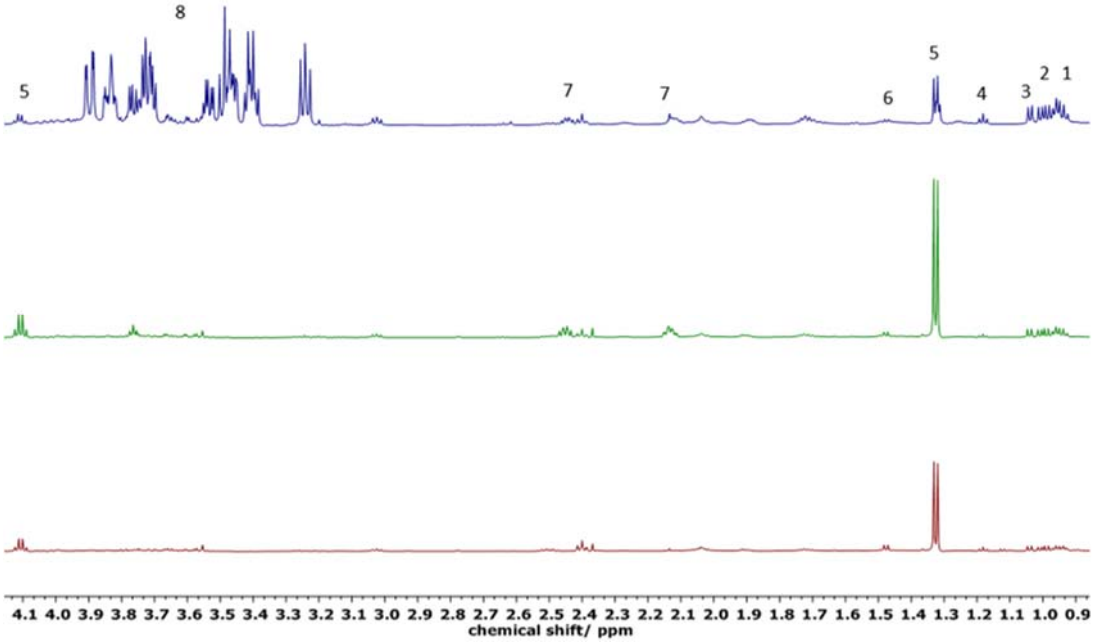

Figure 3.26. Representative ^1H NMR spectra of MCF7 metabolic footprint collected from media of cultured cells in 21% (red) and 1% (green) pO_2 and control media (blue). Labelled metabolites that change in concentration are: 1 – Valine, 2 – Leucine, 3 – Isoleucine, 4 – Ethanol, 5 – Lactate, 6 – Alanine, 7 – Glutamine, 8 – Glucose. Spectra of chemical shift vs. intensity are overlaid on one spectrum.

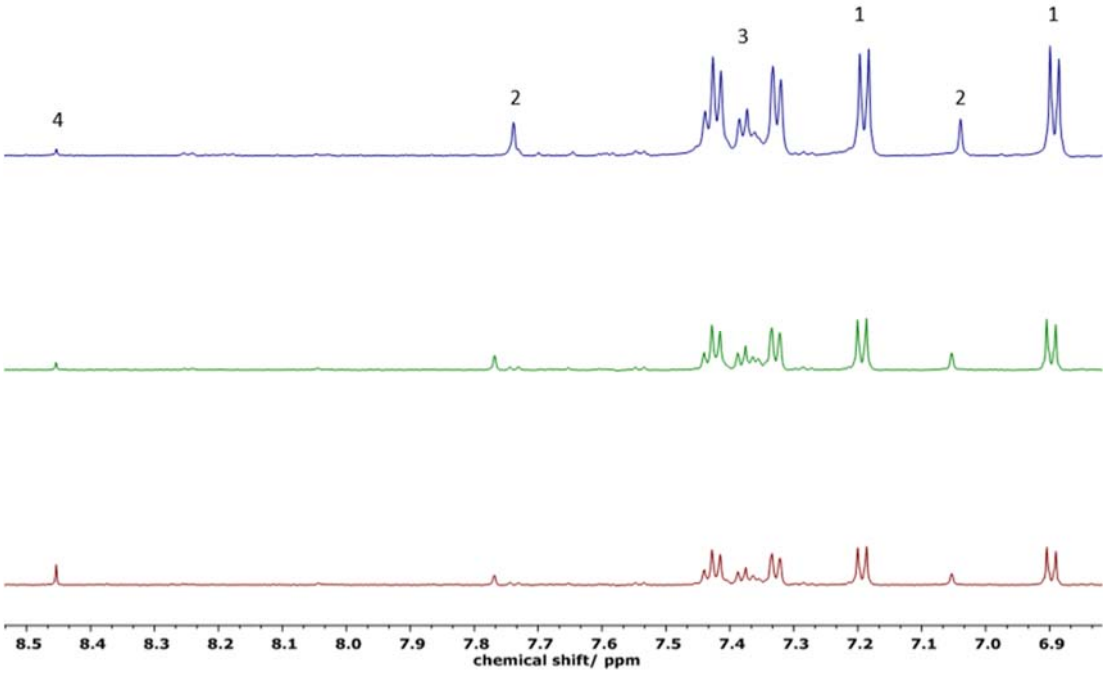

Figure 3.27. Magnified aromatic region of representative ^{1}H NMR spectra of MCF7 metabolic footprint collected from media of cultured cells in 21% (red) and 1% (green) pO_2 and control media (blue). Labelled metabolites that change in concentration are: 1 – Tyrosine, 2 – Histidine, 3 – Phenylalanine, 4 – Formate. Spectra of chemical shift vs. intensity are overlaid on one spectrum.

3.2.5 Metabolic fingerprint of MCF7 cells spiked with a mitochondrial inhibitor

Further analysis was conducted on this cell line to determine if what is being observed, in the aforementioned, is due to suspected increased glycolysis at lower pO_2. Rotenone (1 μM) was spiked into cells cultured at 21% pO_2 for 4 h before metabolite extraction. Rotenone is known to inhibit complex I of the mitochondrial respiratory chain.[81] Normal metabolism via oxidative phosphorylation (OXPHOS) would be hindered and aerobic glycolysis would be favoured, thus mimicking, in theory, results obtained from cells cultured under hypoxic conditions. Figure 3.28 shows, by eye, that increased levels of lactate and amino acids and decreased levels of glucose are observed in both cells cultured at 1% pO_2 and rotenone-spiked samples. No distinct differences were observed in the aromatic regions of all spectra, therefore the spectra are not shown here.

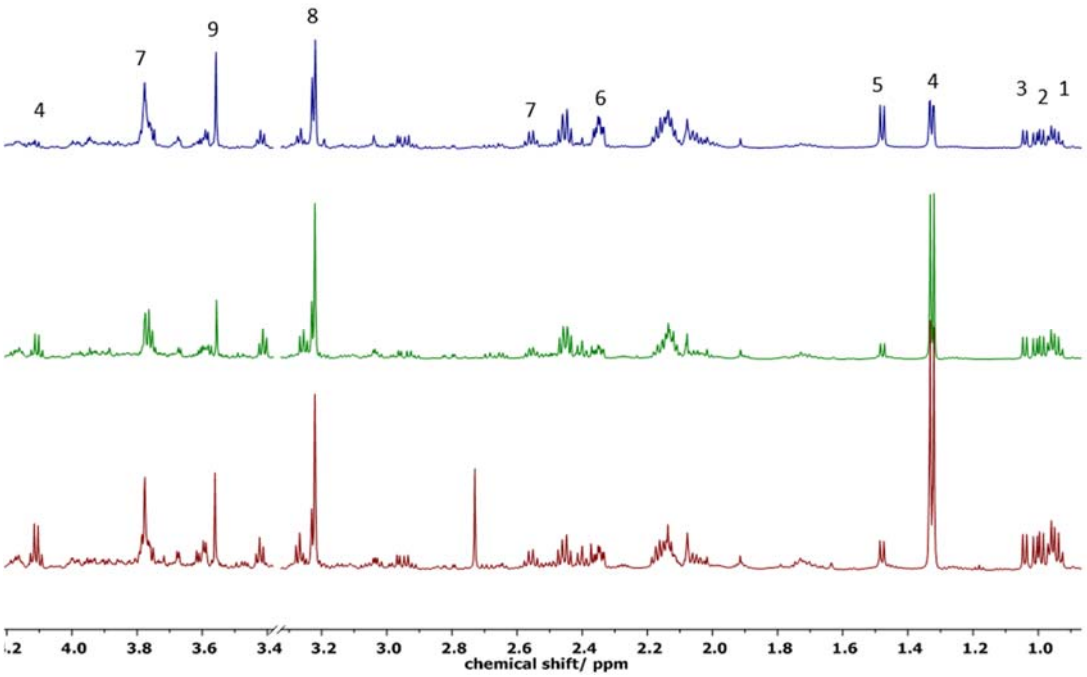

Figure 3.28. Representative aliphatic region ^{1}H NMR of MCF7 cells cultured at (blue) 21% pO_2, (green) 1% pO_2, (red) 21% pO_2 spiked with 1 μM for 4 h. Labelled metabolites that change in concentration are: 1 – Valine, 2 – Leucine, 3 – Isoleucine, 4 – Lactate, 5 – Alanine, 6 – Glutamate, 7 – GSH, 8 – GPC, 9 – Glycine. Spectra of chemical shift vs. intensity are overlaid on one spectrum.

As before, the 3 sample cohorts were normalised to the spectrum with the greatest integral sum and analysed via PCA. Unsupervised analysis has clustered 1% pO_2 and rotenone-spiked samples close together along the first PC, separated from the 21% pO_2 samples (Figure 3.29). The loadings plot (not shown) highlights lactate, alanine, glutamine, glycine, aliphatic amino acids, an unknown (4.22 ppm) and taurine as important contributors to the scores plot results.

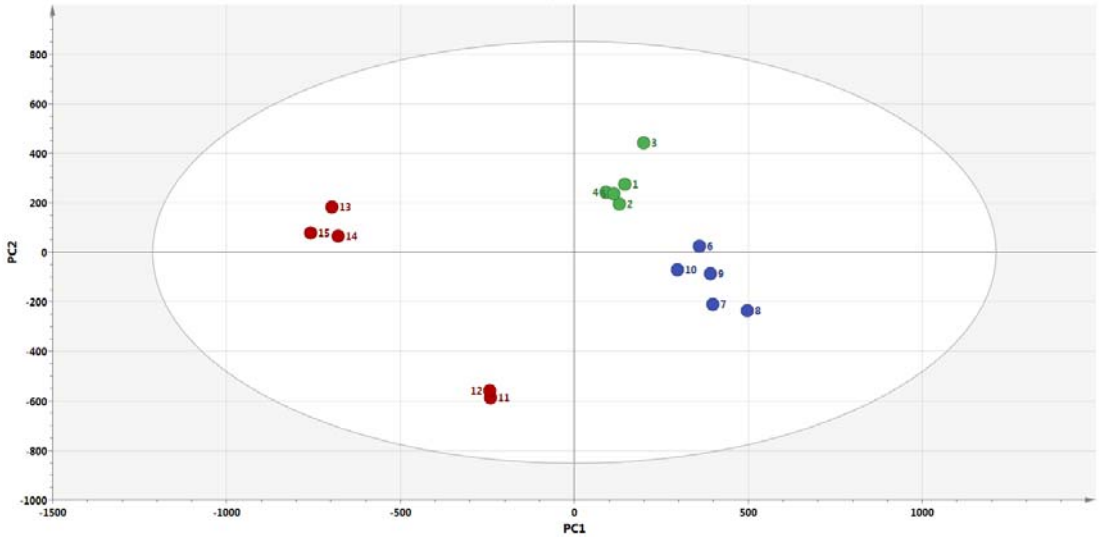

Figure 3.29. PCA score plots of MCF7 cells cultured at 21% pO_2 (red), 1% pO_2 (blue), 21% pO_2 spiked with 1 μM rotenone for 4 h (green).

3.3/ Discussion

A literature search of the main metabolic molecular interactions was conducted and illustrated as a pathway map using yEd Graph Editor. It was added to the group's previously researched and drawn pathway map that includes cellular metabolism, glutathione production and HIF activation. The mEPN, a graphical system, is a collection of symbols that represent components which are defined as physical entities that contribute to a biological pathway. Networks are depicted using nodes and edges. Components, such as proteins and genes, are represented as nodes (vertices) and their interconnectivity with each other is represented as an edge (lines/arcs). Edges symbolise the type of interaction such as inhibition, catalysis and phosphorylation (refer to Figure 3.30 for the key used to construct a pathway map). The human genome nomenclature committee (HGNC) and the mouse genome database (MGD) are used to denote the identity of a component. Cellular compartments are also represented as a particular colour. Metabolites of interest from this work were added to the pathway map to help visualize cellular dynamics.

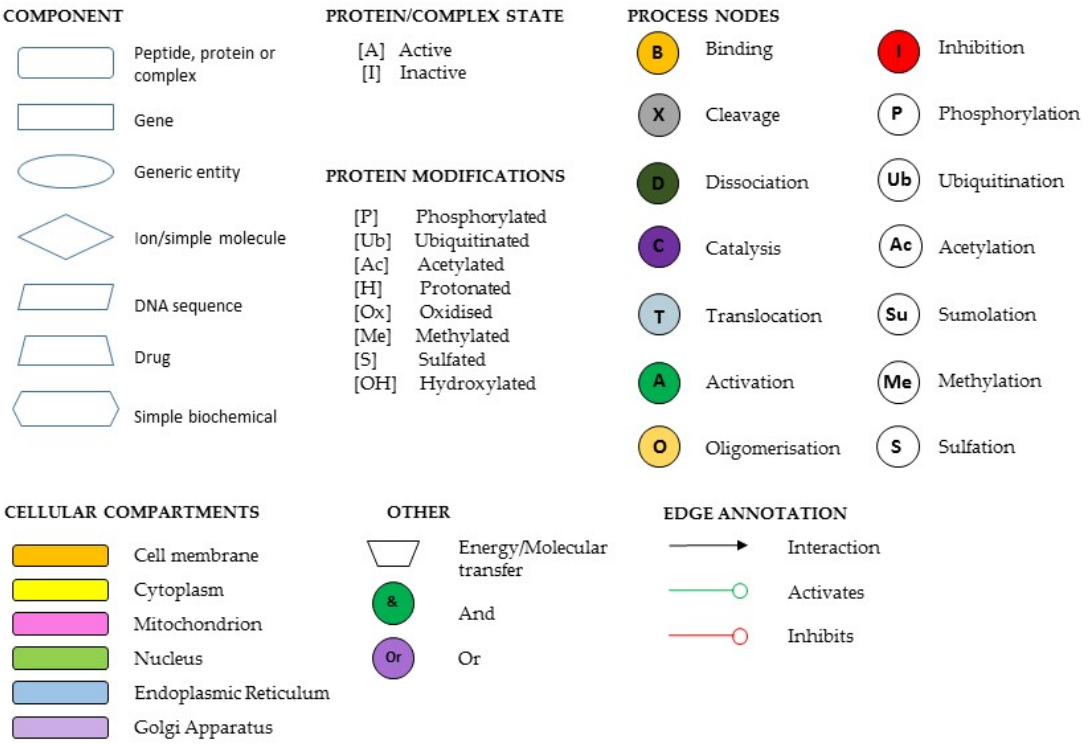

Figure 3.30. Key for drawing a pathway map using yEd Graph Editor.

Metabolite concentrations represent sensitive markers of genomic changes. In this study, the metabolic effects induced by hypoxic conditions were investigated in PC3 cells and in more detail for MCF7 and A549 cell lines. The metabolic fingerprints and footprints of the breast and lung cancer cells were characterised using ^{1}H NMR. The changes associated with response to pO_2 were analysed using both an untargeted and unbiased technique, known as surprisal analysis, and multivariate statistical analysis using SIMCA, a commonly used tool in *omics* studies. Furthermore, the metabolic signature of MCF7 cells after treatment with a mitochondrial inhibitor was probed to determine whether changes observed at 1% pO_2 are likely due to glycolytic fluxes.

Proliferating tumours have a distinct metabolic phenotype characterised by up-regulation of aerobic glycolysis which is a universal trait of malignant transformation, first described by the German biochemist Otto Warburg in 1920. Tumour cells require vast changes in cellular metabolism to sustain the high energy and biosynthetic precursor demands needed for accelerated growth. Warburg discovered that a new

metabolic phenotype is created whereby glucose is directed towards anabolic processes such as the PPP which provides precursors for nucleotide synthesis. The PPP also favours NADPH recycling to maintain GSH levels. Similar to Warburg's findings, discriminatory metabolites discovered by surprisal analysis for A549 and MCF7 cells were mostly associated with energy and glucose metabolism. Below is a comparison of discriminatory metabolites identified by PCA and SA of A549 and MCF7 cell lines in addition to the roles that these metabolites play in the progression of cancer.

3.3.1 Comparison of discriminatory metabolites of A549 cells using PCA and SA

PCA and OPLS-DA separated cells at 21% pO_2 from the rest of the relatively clustered samples incubated at lower pO_2. PCA highlighted glucose, phosphocholine, glutamine, valine, isoleucine and leucine as discriminatory metabolites.

With the exception of glucose, entirely different metabolites of interest were generated using SA. When one constraint was added to the model, metabolites with the highest negative free energy were (in descending order of importance): AMP/ADP/ATP, UMP/UDP/UTP, NADH and UDP-glc. Two unknown peaks at 1.57 ppm and 6.68 ppm and glucose changed in the opposite direction (greatest positive free energy change) to the former metabolites.

3.3.2 Comparison of discriminatory metabolites of MCF7 cells using PCA and SA

Similar to the lung model, PCA separated samples cultured under 21% pO_2 from the rest of the relatively clustered samples incubated at lower pO_2; however, OPLS-DA then further separated cells cultured under 3% pO_2 from the remaining sample set. This is an indication that there are two phenotype changes occurring between, firstly, cells at 21% pO_2 and hypoxic cells and, secondly, between cells at 3% pO_2 and very low pO_2-incubated cells. Metabolites of interest in descending order of importance are lactate, an unknown metabolite (3.03 ppm), glutamine, an unknown metabolite (2.07

ppm), aliphatic amino acids, alanine, glutamate, glycine, taurine, an unknown metabolite (2.55 ppm) and UMP/UDP/UTP.

In contrast to the A549 model, both chemometric tools generated similar metabolites of interest. Furthermore, SA highlighted that many metabolites were contributing to a change in phenotype, whereas in the A549 cell line most metabolites were considered as unimportant to the cancer phenotype when one constraint was added. On addition of one constraint to the MCF7 cell line, the following metabolites with the biggest contribution to the phenotype (in descending order) in terms of positive free energy changes were: glucose, lactate, taurine, fumarate, glutamine, an unknown metabolite (8.45 ppm), histidine, and acetate. Metabolites with the greatest negative free energy changes were: alanine, glycine, glutamate, tyrosine, an unknown metabolite (4.22 ppm), NADH, and phenylalanine.

3.3.3 Glutamine's role in cancer

As mentioned before, tumour cells undergo high rates of glycolysis and redirect carbon sources from catabolic (i.e. Krebs cycle) to anabolic processes. In normal cells, glucose is converted to pyruvate during glycolysis, followed by complete oxidation of pyruvate to carbon dioxide through OXPHOS and Krebs cycle in the mitochondria. This process, which is respiration essentially, produces 36 molecules of ATP per glucose molecule. Redirecting metabolism away from the mitochondria produces only 2 molecules of ATP per molecule of glucose. The decrease in energy production and metabolite sources from processes occurring in the mitochondria make glycolysis insufficient in providing precursors for cell growth and proliferation. However, two anaplerotic pathways - pyruvate carboxylation and glutaminolysis - help replenish metabolites otherwise produced from the Krebs cycle, especially for those metabolites that occur naturally in low concentrations such as α-ketoglutarate and oxaloacete.[76] The turnover rate of glucose is high and, therefore, other carbon sources are needed.

Glutamine, a metabolite of interest common to both A549 and MCF7 cells, is the most abundant amino acid present in cells at a concentration of ~500 μM.[77] Glutamine is

used as an alternative to glucose to provide precursors for biosynthesis, energetics and homeostasis. Mitochondrial glutaminases convert glutamine to glutamate followed by catabolism to α-ketoglutarate. The latter enters the Krebs cycle via glutamate dehydrogenase, a process that produces NADH and NADPH, or by several aminotransferases. This process is particularly important to compensate for loss of metabolites when Krebs cycle rate decreases (refer to Figure 3.31 for Krebs cycle). Depending on the aminotransferase, nitrogen from glutamate is transferred to form α-ketoglutarate and alanine, aspartate or serine. Aspartate is a precursor for nucleotide synthesis.[76] In a previous breast cancer study, it was found that mTOR inhibits glutamate dehydrogenase and promotes aminotransferases which could help explain the increase in the aforementioned amino acids and glutamine concentrations in MCF7 cells under hypoxic conditions.[78] Interestingly, glutamine levels were greater in A549 cells incubated at pO_2 of 4% and higher.

Glutamine also plays a major role in redox homeostasis by being a precursor of GSH, the body's main buffer. GSH is a tripeptide of glutamate, cysteine and glycine (refer to Figure 3.33 for GSH synthesis). The conversion of glutamine to glutamate is the rate-limiting step of GSH synthesis. High concentrations of glutamate, possibly from glutamine turnover, and glycine were present in MCF7 cells under hypoxic conditions but remain unchanged in A549 cells. Glutamate and glycine are also metabolites of interest but unfortunately both GSH and cysteine were undetected in both cell lines.

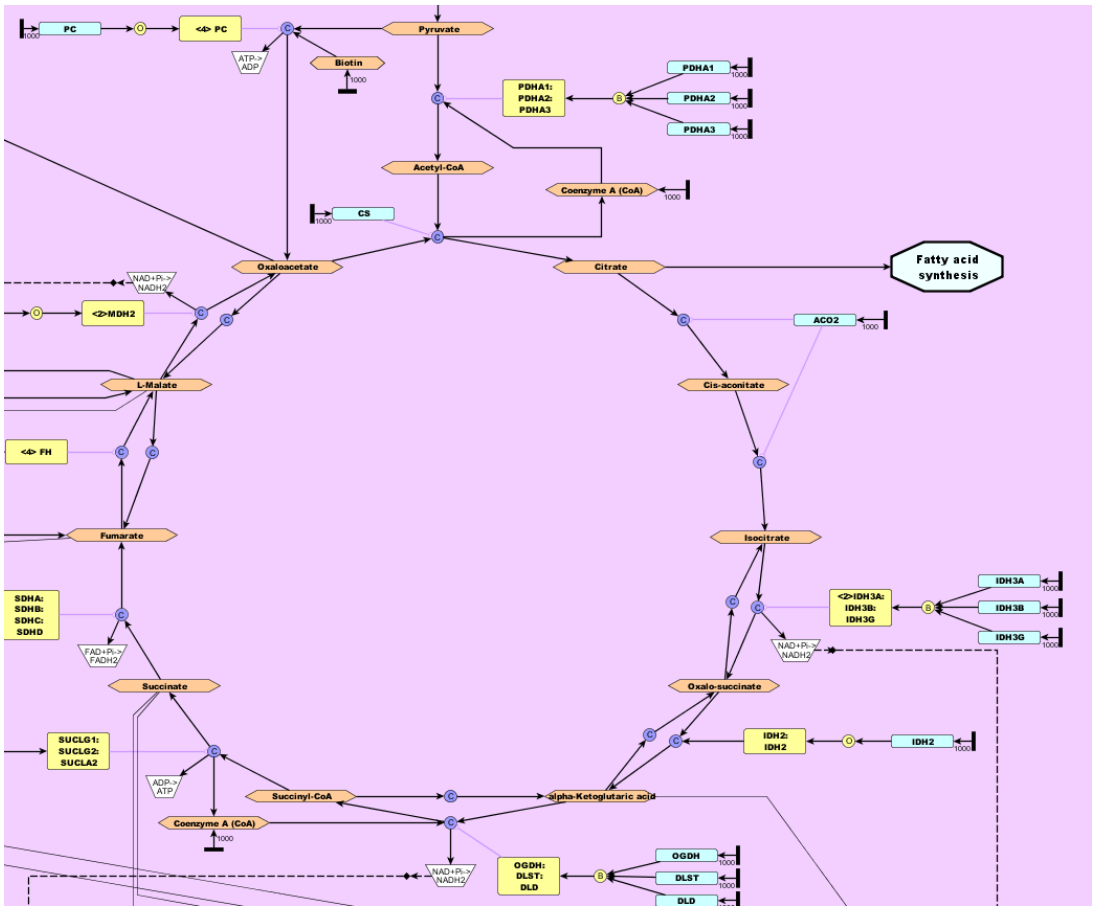

Figure 3.31. Pathway map of TCA cycle.

Nitrogen from glutamine participates directly to the *de novo* synthesis of nucleotides [79] and indirectly through glutamine-derived aspartate.[80] In addition, ribose-5-phosphate converted from glucose-6-phosphate (an intermediate of glycolysis) produces nucleotides, DNA and RNA - all metabolites of interest in both A549 and MCF7 cells.

3.3.4 Lactate's role in cancer

Hypothetically lactate concentrations would increase under hypoxic conditions in cancer models as a result of more active glycolysis.[11], [69], [71] Increased intracellular lactate levels were observed in PC3 and MCF7 cells under hypoxic conditions but were not significantly altered in A549 cells, explaining why the chemometric tools did not identify lactate as a discriminatory metabolite.

Extracellular lactate levels, however, were higher at 21% pO_2 for A549 cells. Lactate metabolism has been found to be different in different cell lines.[81] Under low oxygen and nutrient availability, cancer cells scavenge for alternative carbon sources such as lipids, acetate and lactate, therefore it is possible that A549 cells are consuming lactate rather than excreting it.[82] Intracellular acetate levels, a metabolite of interest in MCF7 cells, were higher under low oxygen conditions in both A549 and MCF7 cells.

3.3.5 Amino acids' role in cancer

Mitochondria play important roles in energy metabolism and are also crucial oxygen sensors; changes in mitochondrial function under hypoxic conditions are likely to contribute to the altered metabolic profiles observed in this work. In mammalian cells, the respiratory chain is composed of 5 enzymes embedded in the inner mitochondrial membrane and is responsible for OXPHOS. Rotenone inhibits complex 1, therefore impacting metabolic pathways associated with OXPHOS activity.[83] If indeed the level of oxygen is having an effect on the metabolic profile by diverting to predominantly glycolysis, it would be expected that inhibition of the mitochondria would express similar results found from cells cultured under hypoxic conditions. As can be seen from Figure 3.29, spiked cells and those cultured under hypoxic conditions are relatively close in the scores plot, suggesting similar characteristics. Lower concentrations of alanine were present in the rotenone spike, similar to MCF7 cells under limited oxygen availability. Elevated levels of alanine, which is produced by transamination of pyruvate during amino acid synthesis, were found in cells cultured under 21% pO_2.[84] Glycine concentrations were higher compared to normoxic cells which are indicative of the profound need for this metabolite in purine and GSH synthesis.

In both cell lines, the levels of amino acids are listed as important contributors to a change in the phenotype. More intracellular amino acids are found under 21% pO_2 in A549 and MCF7 cells. An increase in amino acid concentrations could be attributed

by either decreased protein synthesis,[81] increased protein catabolism and/or increased amino acid uptake. The latter can be confirmed as the concentration of amino acids in the media from cultured cells is lower than those in media from hypoxic cells. Under hypoxic conditions, these ATP-consuming reactions may be slowed down.

3.3.6 Coenzymes' role in cancer

Coenzymes, such as ATP and NADPH, play important roles such as redox homeostasis, cell signalling and cell death. The rate of the reversible redox reactions that these enzymes undergo is in important indication of the physiological state of the cell, whether the cell is undergoing apoptosis or entering into a diseased state. ATP is the cell's main energy source, mediating many biochemical reactions that are fundamental to the functioning of cells. Ratios of the oxidised and reduced forms of coenzymes can give a measure of cellular bioenergetics but, unfortunately in both cell models, coenzymes could not be differentiated.[85] Under hypoxic conditions, HIF-1 inhibits pyruvate dehydrogenase activity, thus preventing the conversion of pyruvate into acetyl-coA. Pyruvate can then be metabolised back into glucose to repeat glycolysis and the regeneration of NAD^+ required for ATP production.[86] SA identified NADH in MCF7 as a key metabolite that differentiates samples at different oxygen conditions. NADH concentration is highest at 4% pO_2 and lowest at 21% pO_2.

3.3.7 UDP-glucose's role in cancer

Uridine diphosphate glucose (UDP-Glc) is used for glycogen synthesis and is a precursor in glycosphingolipids.[87] UDP-Glc is synthesised from glucose-1-phosphate which is converted from glucose-6-phosphate.[88] UDP-Glc is high at 21% and 1% pO_2 in MCF7 cells. In A549 cells, UDP-Glc is present in low concentrations at varying oxygen pO_2.

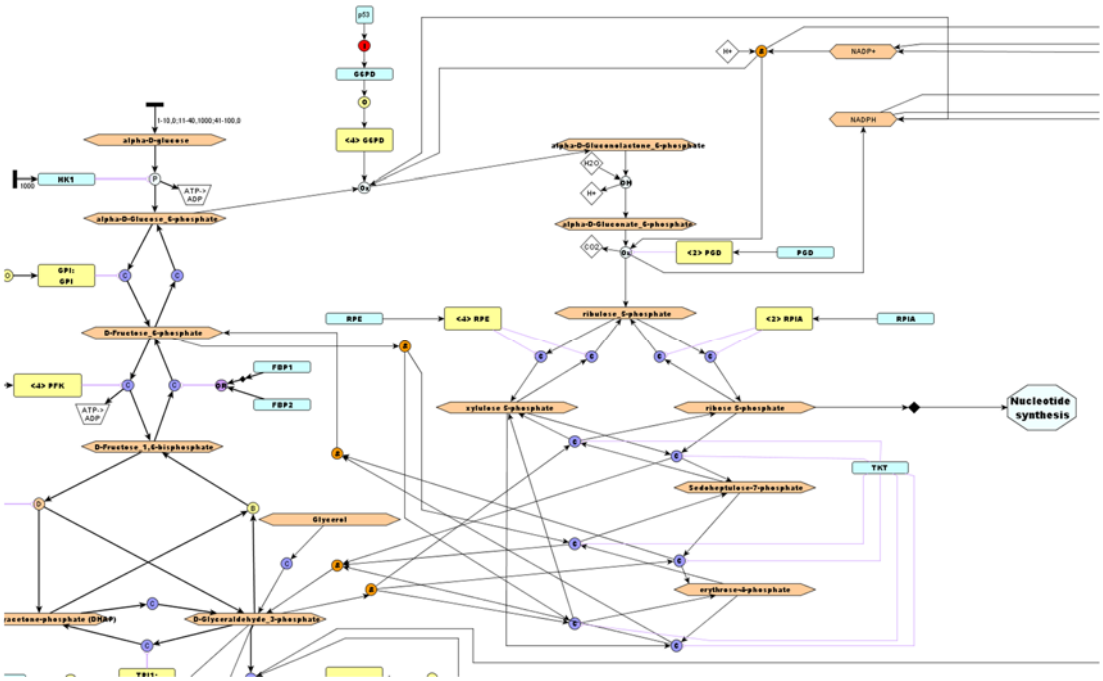

Figure 3.32. Partial pathway map of glycolysis and PPP.

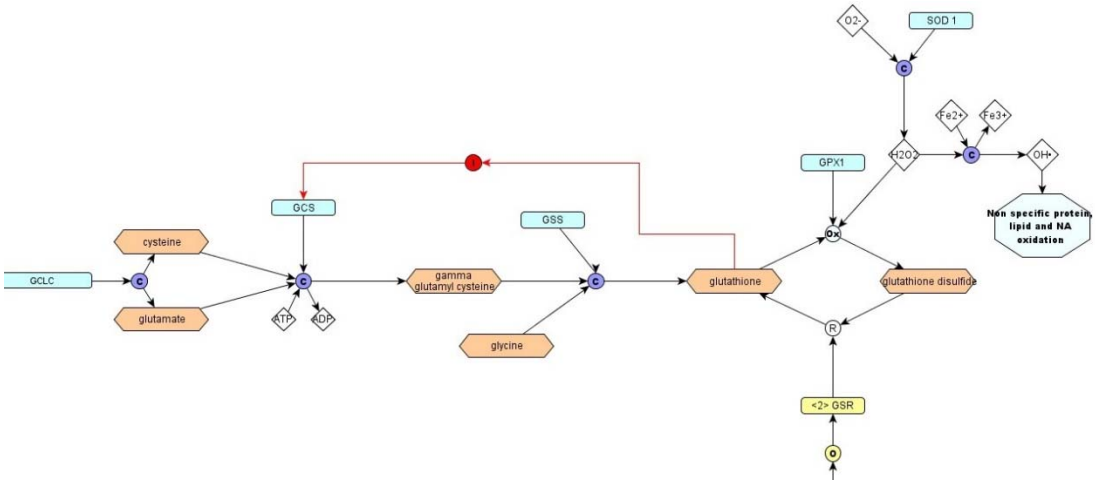

Figure 3.33. Pathway map of GSH synthesis.

3.3.8 Taurine's role in cancer

Taurine, which is synthesised from cysteine, is a stabiliser of cell membranes and has the potential for scavenging free radicals due to its sulfur group.[89], [90] The concentration of taurine is at its highest at 2% pO_2 and significantly lower at 21% pO_2 in MCF7 cells. Studies have shown that taurine is abundant in breast cancer and induces apoptosis through process not yet fully elucidated. In mouse models, intake of taurine actually led to breast tumour attenuation.[91], [92] Perhaps in my model, taurine is quickly metabolised to acetate and acetyl-CoA for fatty acid synthesis.

3.3.9 Fumarate's role in cancer

Lastly, fumarate, another important metabolite flagged up by SA, is relatively consistent in concentration between 1 and 4% pO_2 and lower at 21% pO_2. Fumarate is synthesised through the oxidation of succinic acid in the Krebs cycle. It has been reported that fumarate is leaked into cytosol to inhibit prolyl hydroxylase enzymes which subsequently leads to stabilisation of HIF.[93]

3.4/ Conclusion

Cancer cells can adapt their metabolism under low nutrient and oxygen availability, avoiding apoptosis and increasing the rate of anabolic synthesis. Monitoring the metabolic status of biological models can help us to better understand the reprogramming of cancer cells and the Warburg effect. Metabolomics is employed to help identify biomarkers of these changes and detect personalised responses to therapy. A challenge for systems biology is to discover the driving forces for malignancy transformation away from the healthy cellular state. Surprisal analysis is an information-theoretic analysis method that is used for dimension reduction and visualization of the data. Combining NMR with surprisal analysis provides an instantaneous snapshot into the biochemical pathways of a cell which is downstream and complementary to other *omic* studies. This research has identified metabolites responsible for discriminating cells incubated under different oxygen concentrations.

Chapter 4: MS and Chemometric Analysis of Organic Phase Metabolites

4.1/ Introduction

Lipidomics is an emerging field with potential for identifying disease biomarkers due to advancements in lipid analysis and bioinformatics technology. Further investigation in comprehending perturbation in lipid biochemical mechanisms under different cellular conditions is still needed but the complexity and diversity of lipids make this formidably challenging.

Lipids usually consist of fatty acids linked by a backbone of glycerol or a sphingoid. Lipids can be divided into subgroups such as fatty acyls, glycerophospholipids, sphingolipids and sterol lipids (structures in Figure 4.1). Lipogenesis is responsible for the biosynthesis of cell membranes and is, therefore, essential for the growth and proliferation of cells. Previous research reveals the roles of lipids in tumour progression; however, their biological role in cancer remains partially understood. Alterations in the lipid profile can affect: signalling functions; the availability of structural lipids for the synthesis of membranes; energy homeostasis through the storage and degradation of lipids.[94]–[97]

Fatty acyls:

Fatty acyl is a generic name for describing fatty acids (FAs) and their derivatives. Fatty acids are common building blocks of complex lipids. Their structure constitutes a straight-chain of even number of carbon atoms as their biosynthesis involves elongation of an acetyl-CoA primer. Fatty acyls normally contain one carboxylic acid group and can be either saturated or unsaturated. Most naturally occurring FAs are 4-28 carbon atoms long and are metabolised by cytochrome P450 enzymes to form active cell signalling molecules, upregulation of which has been reported in various cancers such as breast.[98], [99]

Phospholipids:

Phospholipids are key components of the cellular lipid bilayer. They are divided into subgroups depending on the diacylglycerophosphoryl unit. They are: glycerophospocholines (PC), glycerophosphoethanolamines (PE), glycerophosphoinositols (PI), glycerophosphoglycerols (PG), glycerophosphoserines (PS) and glycerophosphatidic acid (PA).

Sterol lipids:

Sterol lipids, with cholesterol being the most abundant, play different roles as hormones and signalling molecules. They are important components of the cell membrane and can be responsible for protein trafficking and signalling at the cell surface.[100]

Sphingolipids:

Sphingolipids (SL) are formed from the condensation of L-serine and a long-chain acyl thioester, and are divided into 2 categories: sphingomyelins and glycosphingolipids. These lipids contain a long-chain sphingosine backbone and are also one of the main components of cell membranes. The sphingosine amino group is acetylated with long-chain FAs, producing a ceramide. Sphingomyelin, derived from ceramide and choline from phosphatidylcholine, is the only phospholipid not derived from glycerol. SLs are involved in cell proliferation, inflammation, apoptosis regulation and senescence.[101], [102] Previous studies on lung cancer discovered that sphingolipid levels, such as ceramide, glycosphingolipid, sphinganine, sphingomyelin and spingosine-1-phosphate, are elevated. SLs are already being used in anti-cancer therapy and are regarded as important signals for inducing apoptosis.[103]–[105]

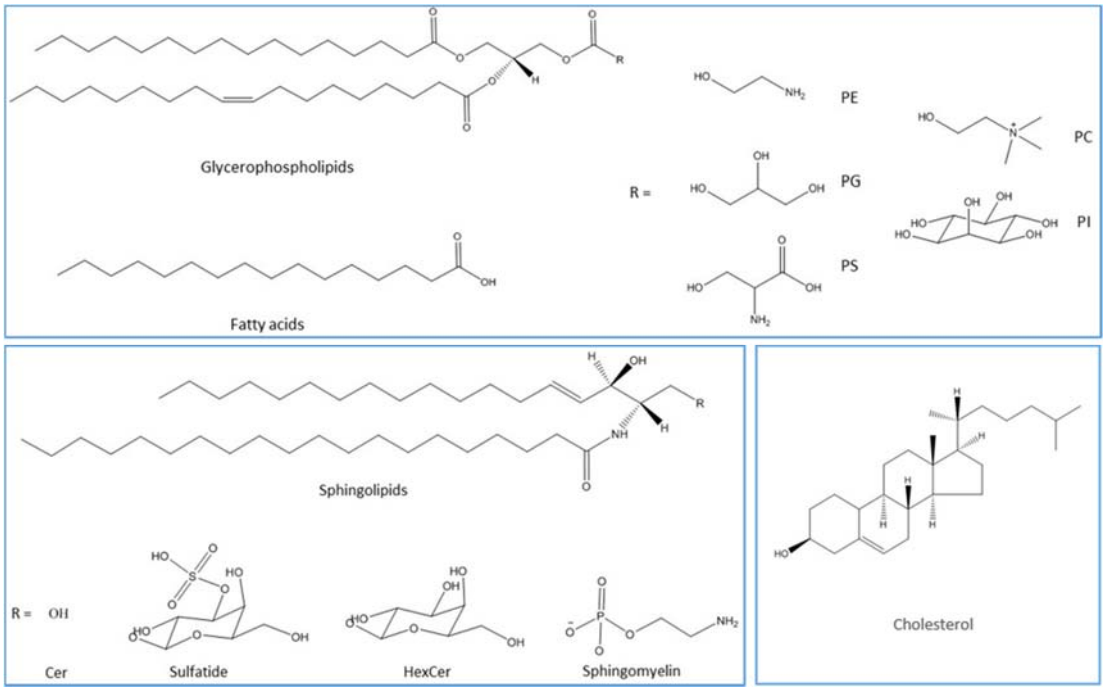

Figure 4.1. Structures of lipid classes

4.1.1 Roles in Membrane Structure

Glycerophospholipids are the main structural component of cellular plasma membranes and intracellular membranes of organelles. The structure of these amphipathic molecules consists of a glycerol core linked to a polar head group by a phosphate ester linkage and to two fatty acids by ester linkages. Non-glyceride-containing lipids, such as sphingomyelin and sterols, are also found in biological membranes. Membranes are composed of lipid bilayers with the head groups positioned towards the polar, aqueous environment whilst the hydrophobic tails align inwards. Lipid bilayers are impermeable to ions and, so, regulate cellular pH and salt concentrations through the use of ion pumps.

Cardiolipins are a subclass of glycerophospholipids and are almost exclusively located in the inner mitochondrial membrane where they can bind to and activate enzymes involved in the electron transport chain. Cardiolipins assist in OXPHOS by

trapping protons, creating a proton pool to maintain pH in the mitochondrial intermembrane space.[106]

4.1.2 Roles in Signalling

Emerging evidence has demonstrated the impact of lipid signalling on normal cellular processes. Sphingosine-1-phosphate, for example, is involved in apoptosis, calcium mobilisation and cell growth.[105] PIs and diacylglycerol activate the protein kinase C pathway which subsequently induces signal transduction cascades to activate/deactivate particular proteins. Diacylglycerols are synthesised from glycerol-3-phosphate (G3P), which is derived primarily from dihydroxyacetone phosphate, a product of glycolysis. G3P is first acetylated with acyl-coenzyme A (acyl-CoA) to form lysophosphatidic acid, which is then acetylated with another acyl-CoA to yield phosphatidic acid. The latter is de-phosphorylated to form diacylglycerol. Diacylglycerol is a precursor for triglycerides which are formed by the addition of a third fatty acid to the diacylglycerol under the catalysis of diglyceride acyltransferase.[107]

Analysis of the lipidome was conducted in this project via electrospray ionisation-mass spectrometry (ESI-MS). MS is quick and has the added advantage of being highly sensitive, producing high-resolution spectra. The technique can detect thousands of metabolites in a single measurement. NMR has been used in previous research to assess inter-class distribution of a lipid mixture but MS is favoured in analysing intra-class distribution. NMR is not sensitive enough for comprehensive structural elucidation of lipids as it cannot give double bond positions and chain length for example. The latter information can be easily sought from tandem MS.[108] Fourier-transform ion cyclotron resonance (FTICR) analyser was used in this research because of its high resolution and sensitivity and no prior separation of lipid classes is needed.[96] Lipid metabolite and pathways strategy (LIPID MAPS), Metlin Scripps and HMDB were used to identify lipids based on their m/z.

4.2/ Results

Organic phase extracts collected from MCF7 cells were first analysed by ^{1}H NMR in deuterated chloroform to observe any inter-class distribution. Figure 4.2 clearly shows that solution state NMR is probably not the best technique to use in this case! Only three broad peaks representing methyl and methylene groups are visible.

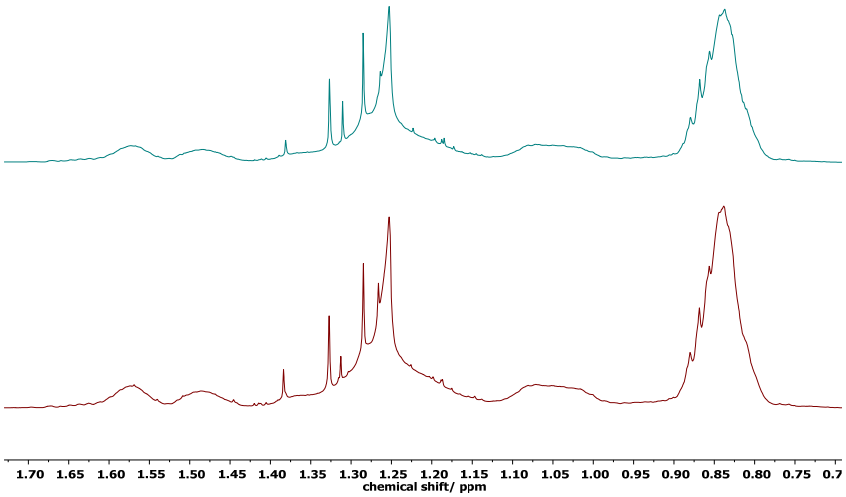

Figure 4.2. Representative ^{1}H NMR of MCF7 cells cultured under (top) 1% and (bottom) 21% pO_2. The chemical shift vs. intensity of the spectra are overlaid.

FTICR MS was then used to analyse the lipidome of MCF7 cells cultured under 1% and 21% pO_2 (6 of each cohort) in both positive and negative modes in the m/z range of 200-2500.

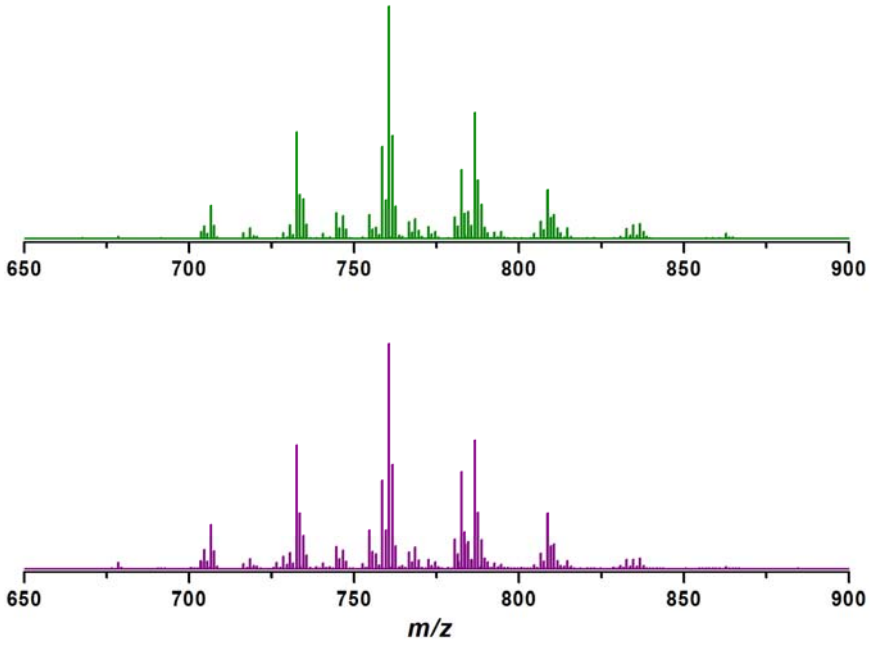

Figure 4.3. Magnified representative positive mode MS spectra of MCF7 cells cultured under 1% (green) and 21% (purple) pO_2. Spectra of m/z vs. intensity of spectra are overlaid.

In negative mode (not shown), there is very little distinction between the cell and control samples (perhaps the lipids are not acidic enough to lose a proton), therefore analysis was conducted using results from positive mode (Figure 4.3). (The whole spectra with control sample comparison can be found in Appendix A.) Samples were spiked with ESI Tuning Mix as an external calibrant. Several lipids in the samples were first identified using LIPID MAPS. Those that produced one hit in the database with a high degree of certainty (0.001 Da) were used to produce an internal calibrant list that all spectra were calibrated to. A signal:noise ratio of 4 and an absolute intensity threshold of $4x10^6$ were chosen and applied. The generated peak list was processed using PCA and PLS-DA to identify any changes in the lipidome. Interestingly, no significant differences were observed between the two cell cohorts. Mainly glycerol lipids and glycerophospholipids dominated the spectra (**Error! Reference source not found.**).

The MS data were first normalised to the sum of the spectrum with the highest peak intensity before being imported to SIMCA-P+ 13.0. PCA was, first, adopted to

examine inherent clustering and patterns within the data (Figure 4.4). Briefly, once the dimensionality of the MS data is reduced, the new plots generated are known as scores. Points, which correspond to the samples, close to each other have similar properties, whereas those far from each other are dissimilar. Observations that lie outside the 0.95 Hotelling's T^2 ellipse are classed as strong outliers. The loadings plot gives an indication of the magnitude (large or small correlation) and the manner (positive or negative correlation) which the *m*/*z* intensity values contribute to the scores.

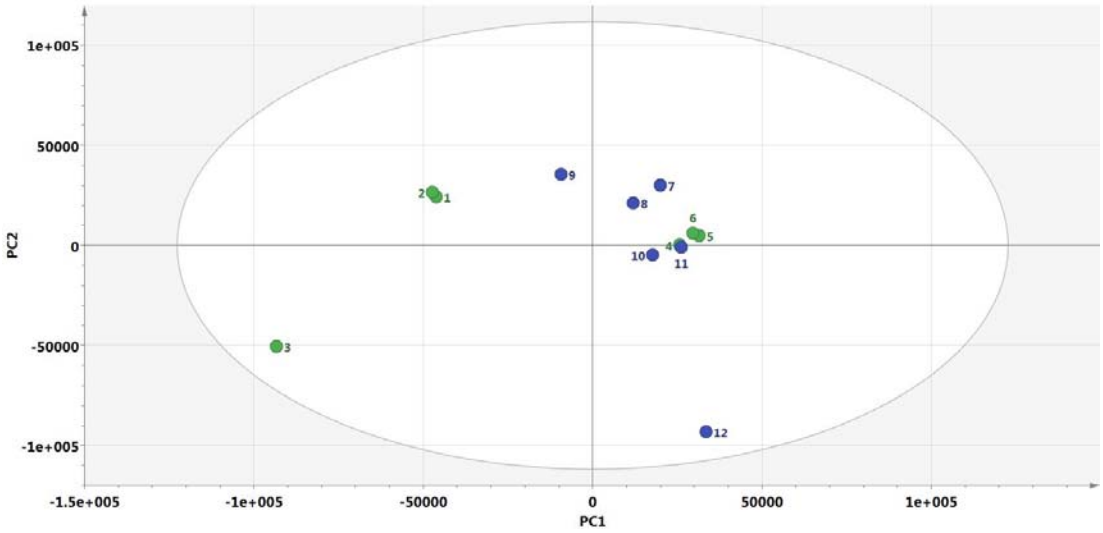

Figure 4.4. PCA scores plot with 3 PCs of organic phase extracts from MCF7 cells cultured at 1% (green) and 21% (blue) pO_2.

PLS-DA was used to assess class membership (Figure 4.5). It finds the fundamental relations between the two matrices **X** (class variables) and **Y** (class membership). The technique will try to find the multidimensional direction in the **X** space that best explains the maximum multidimensional variance direction in the **Y** space. CV-ANOVA was conducted, giving a *p*-value of 0.042 which indicates no significance between the two sample cohorts.

A permutation test was conducted to test the validity and degree of over-fit of the PLS-DA model. This involves randomly ordering the Y-observations but keeping the X-matrix the same. New models are created and the R^2 and Q^2 values are compared with the original model. 100 permutations were calculated here (Figure 4.6). If Q^2 of the original model (far right of permutation model) was equal to or higher than the maximum value of Q^2 on the vertical axis (far left) from the randomly permuted data, the PLS-DA model is regarded as a robust model. The same is said for if the blue regression line of the Q^2 points intersects the vertical axis at or below zero. The permutation test revealed positive slopes with a Q^2 of 0.716 which is the same as the original PLS-DA model, indicating a good predictive model. The permuted data also has a R^2 of 0.975, suggesting the original PLS-DA model is over-fitted.

The scores and loadings of the PLS method can be heavily influenced by strong systematic variations present in the data that are unrelated to the response, making interpretation of the model more difficult. Such variation can arise from instrument and sample handling errors or temperature fluctuations for example which are common with mass spectrometers. More components can be included in the model to improve prediction accuracy but this may lead to over-fitting and increased model complexity.

Furthermore, the cross-validation method for predicting the error of models (R^2) is not very accurate. In this method, N samples of the training set of size M are removed and a model is generated from the M − N remaining data points. The characteristics/properties of the omitted samples are predicted from the new test model. This is done M/N times so that each member of the training set is omitted once. The resulting R^2 value tends to be overly optimistic, particularly when the sample set is small compared to the number of variables which is often the case in metaobolomics. Model quality and predictivity should be assessed using an external test data, not only on the training data as it is not truly random. Doing so produces reliable statistics for comparison between the observed and predicted activities for the test set.[109]

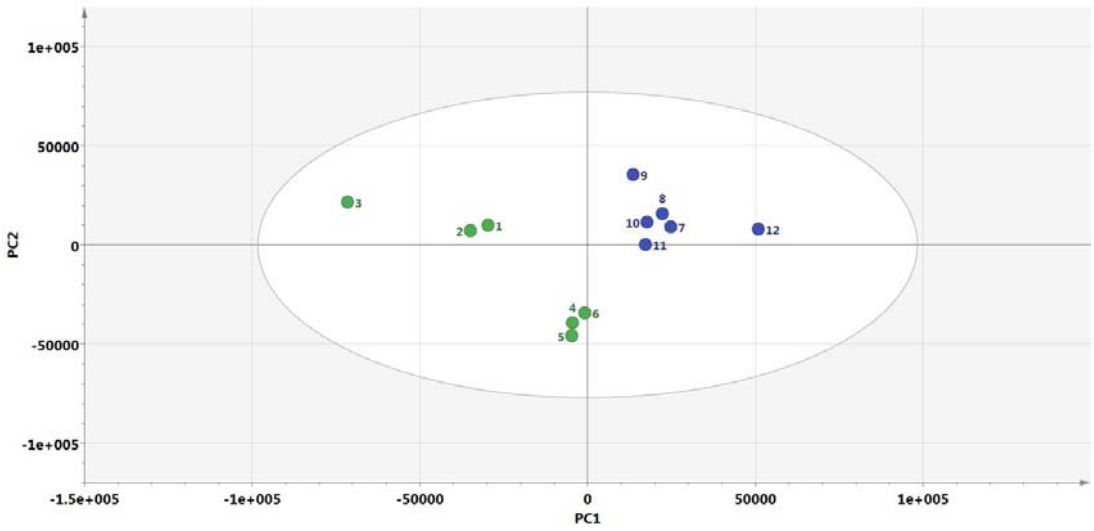

Figure 4.5. PLS-DA scores plot with 3 PCs of organic phase extracts from MCF7 cells cultured at 1% (green) and 21% (blue) pO2. $Q^2 = 0.716$ and $R^2X = 0.571$ and CV-ANOVA p-value = 0.041595.

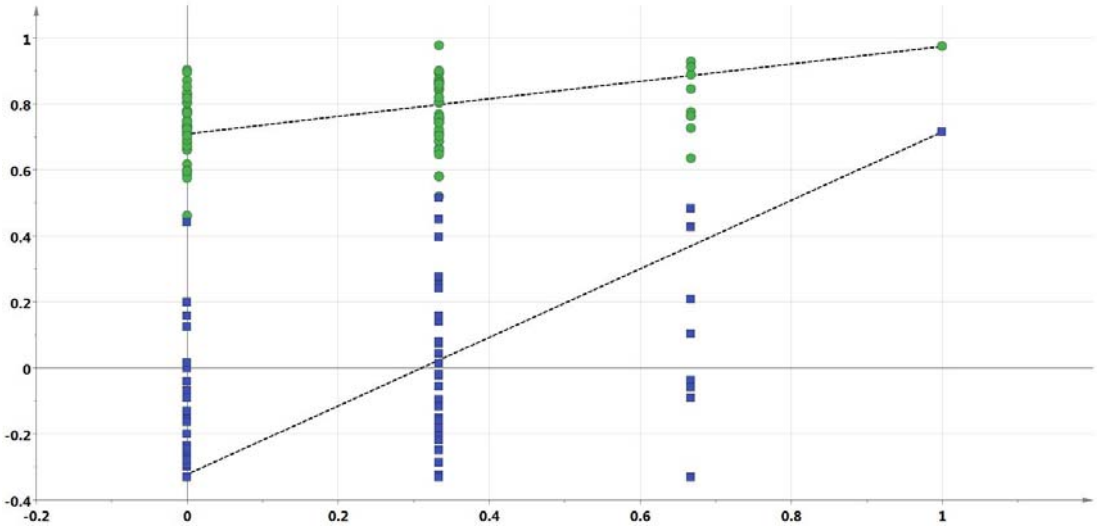

Figure 4.6. Permutations test to test the validity of the PLS-DA model of the MCF7 MS data with 3 PCs. $Q^2max = 0.441$ and $R^2Xmax = 0.975$.

Identifying unknown metabolites is a major challenge in metabolomics; however, databases help to narrow peak assignments to a smaller list of potential hits. Assigning correctly an unambiguous peak is difficult as more abundant signals can

overlay those of lower abundance. This is particularly the case in MS as many signals produce several hits of potential structures (using the databases Metlin Scripps, LIPID MAPS and HMDB), thus making definite identification impossible.

Error! Reference source not found.. Suggested assignments of lipids which contribute (in descending order) to the PLS-DA scores plot. Key: PC = glycerophosphocholine; PG = glycerophosphoglycerols; GL = glycerolipids; PE = glycerophosphoethanolamines.

Adduct m/z	Ion	Chemical formula	Lipid class
734.5693	$[M+H]^+$	$C_{40}H_{80}NO_8P$	PE
760.5847	$[M+H]^+$	$C_{42}H_{82}NO_8P$	PC
703.5752	$[M+H]^+$	$C_{45}H_{82}O_5$	GL
787.6043	$[M+H]^+$	$C_{44}H_{85}NO_8P$	PC
733.5571	$[M+H]^+$	$C_{40}H_{77}O_9P$	PG
788.6084	$[M+H]^+$	$C_{44}H_{84}O_9P$	PG
732.5533	$[M+H]^+$	$C_{40}H_{78}NO_8P$	PC
782.5677	$[M+Na]^+$	$C_{42}H_{82}NO_8P$	PC
735.5730	$[M+H]^+$	$C_{40}H_{79}O_9P$	PG
782.5618	$[M+H]^+$	$C_{45}H_{81}O_{10}$	GL
704.5227	$[M+H]^+$	$C_{38}H_{74}NO_8P$	PC
808.5838	$[M+Na]^+$	$C_{44}H_{84}NO_8P$	PC
810.6015	$[M+H]^+$	$C_{46}H_{84}O_8P$	PC
788.6170	$[M+H]^+$	$C_{44}H_{86}NO_8P$	PC
758.5688	$[M+H]^+$	$C_{42}H_{80}NO_8P$	PE

As a confirmation of the presence of sphingolipids around 700 Da, myriocin [(2S,3R,4R,6E)-2-amino-3,4-dihydroxy-2-(hydroxymethyl)-14-oxo-6-eicosenoic acid] was added to the cell culture. Myriocin is a natural product from thermophilic *Mycelia sterilia*, *Isariasinclairii* and *Cordyceps cicadae* and inhibits the pyridoxal-5'-phosphate (PLP)-dependent enzyme serine palmitoyltransferase (SPT) which catalyses the first and rate-determining step in *de novo* SL biosynthesis.[101], [110] The SPT inhibitor has been extensively used in cancer models [102] and myocardial reperfusion injuries [104], for example, as a therapeutic target with promising results. Here I spiked cell samples cultured under 1% and 21% pO_2 with myriocin (10 μM) for 24 h to confirm SL classification. No peaks disappeared or were reduced in intensity from the mass spectra when spiked with the SL inhibitor, despite SL constituting 10-20% of cellular lipids.[111] A higher concentration was used (20 μM) but this caused cell death in the same incubation period. Figure 4.7 shows an example of cells cultured under 1% pO_2 with and without spiking with myriocin.

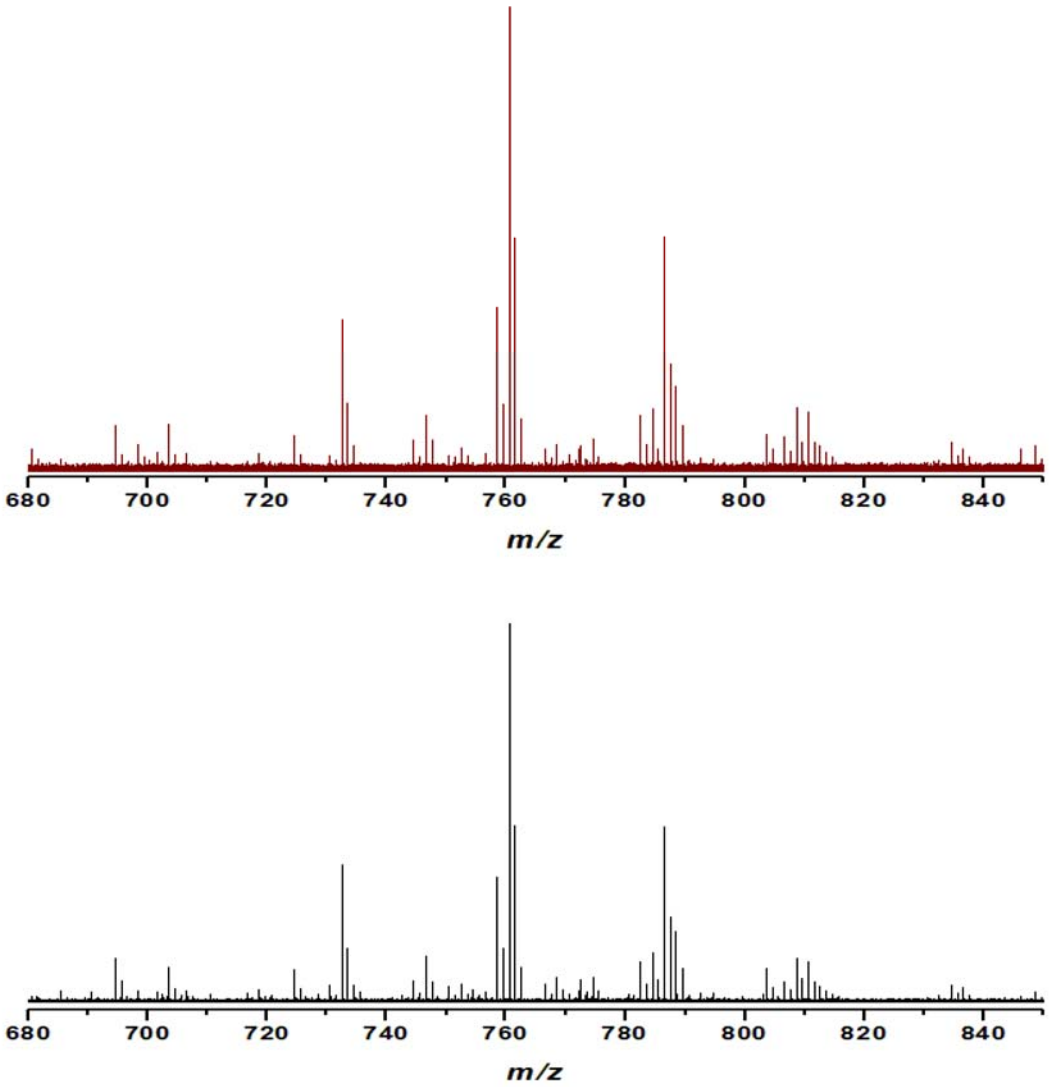

Figure 4.7. Magnified representative positive mode MS spectra of MCF7 cells cultured under 1% (red) and 1% with myriocin spike (black) pO_2. Spectra of m/z vs. intensity are overlaid.

4.3/ Discussion

Studies have demonstrated that low-oxygen conditions alter carbohydrate and lipid metabolism. A switch to anaerobic energy production occurs whereby lipids are synthesised from glutamine as a carbon source instead of from glucose.[112] In order to address the hypoxia-mediated alterations in the lipid profile and to reveal molecular pathways involved, the lipidome of MCF7 cells was investigated.

One hallmark of cancer is the accelerated rate of *de novo* fatty acid synthesis to fuel membrane production and energy metabolism. Fatty acids (FAs) are either derived endogenously from citrate or are taken up from exogenous sources.[95] For the latter, triglycerides from very low-density lipoprotein particles are imported via FA channel proteins once hydrolysed to FAs. Fatty acid synthase (FASN) catalyses the terminal step in the synthesis of FAs from citrate-derived acetyl-CoA, malonyl-CoA and NADPH, predominately producing palmitate (16-carbon FA).[113] Further elongation occurs on the cytoplasmic face of the endoplasmic reticulum and can be desaturated by fatty acyl-CoA desaturases. FAs are stored in the form of triacylglycerols under normal conditions. When additional metabolic fuel is needed, the triacylglycerols are made available through β-oxidation. With the use of isotopically-labelled glucose, it was discovered that most triacylglycerol were derived from *de novo* synthesis, not from dietary FAs in tumour models.[114]

FA synthesis is supported through the upregulation of certain lipogenic enzymes. As well as FASN, two other major enzymes have been linked to carcinogenesis. Firstly, acetyl-CoA carboxylase (ACACA) catalyses the rate-limiting carboxylation of acetyl-CoA to malonyl-CoA for FA synthesis.[115] The overexpression of this enzyme has been reported in breast carcinoma by *Milgraum et al*.[113] Secondly, ATP citrate lyase (ACLY) is responsible for catalysing the first step of *de novo* lipogenesis and linking aerobic glycolysis and FA synthesis (Figure 4.8). ACLY produces cytosolic acetyl-CoA from citrate derived from the TCA cycle, inhibition of which induces apoptosis in MCF7 cells.[116], [117] ACLY activity is also responsible for histone acetylation and gene expression in response to growth factor stimulation.[118] PI3K/Akt signalling pathway regulates ACLY by directly phosphorylating ACLY.[119]

Lipid metabolism is regulated by the transcription factor sterol regulatory element binding protein-1c (SREBP-1c) which stimulates FASN activity. SREBP is activated by the PI3k-Akt and ERK1/2 signal transduction pathways once they are subsequently activated by growth factors. FASN inhibition attenuates tumour growth, implicating its role in the molecular integration of signalling pathways that link metabolism,

proliferation and cell survival. FASN also plays a role in redox homeostasis through consumption of NADPH.[120] In addition, FA synthesis and chain elongation provides oxidising power which is important under hypoxic conditions. AMP-activated protein kinase (AMPK) is an energy sensor and regulates the phosphorylation of ACACA the FASN expression levels. Under hypoxic conditions, AMPK inhibits acetyl-CoA carboxylase (ACC) to reduce malonyl-CoA concentration. This process drives the delivery of long-chain acyl-CoA into the mitochondria for β-oxidation, restoring the energy balance.[121]

The majority of endogenously synthesised FAs are converted to phospholipids in rapidly proliferating cells [122] which is evident from the results obtained here. Phospholipids are one of the major components of cell membranes, consisting of a polar head group and fatty acyl chains which can vary in length and degree of unsaturation. Phospholipid composition determines the physical and functional properties of membranes. *Marien et al.* were able to distinguish the phospholipid composition of tissue derived from patients with non-small lung cancer (NSCLC) from healthy patients using ESI-MS/MS and 2D-imaging MS. Key discriminatory lipids were specific PIs [123] which are known to activate the Akt signalling pathway.[124]

Phospholipids, together with sterols and sphingolipids, represent the major structural components of biological membranes. Cancer cells require more phospholipids to build membranes of new cells quickly, therefore it is not surprising that a marked overexpression of lipogenic enzymes, such as fatty acid synthase (FASN), have already been recorded. FASN catalyses the terminal steps in the *de novo* biogenesis of fatty acids.[113]

The mevalonate pathway is an important process in lipid metabolism as it aids in cholestorol synthesis. The process involves condensation of acetyl-CoA to form 3-hydroxy-3-methylglutaryl (HMG)-CoA. HMG-CoA is then reduced to mevalonate by

HMG-CoA reductase (HMGCR) and is highly regulated. Cholesterol is important for membrane fluidity and facilitates in the activation of signalling pathways.

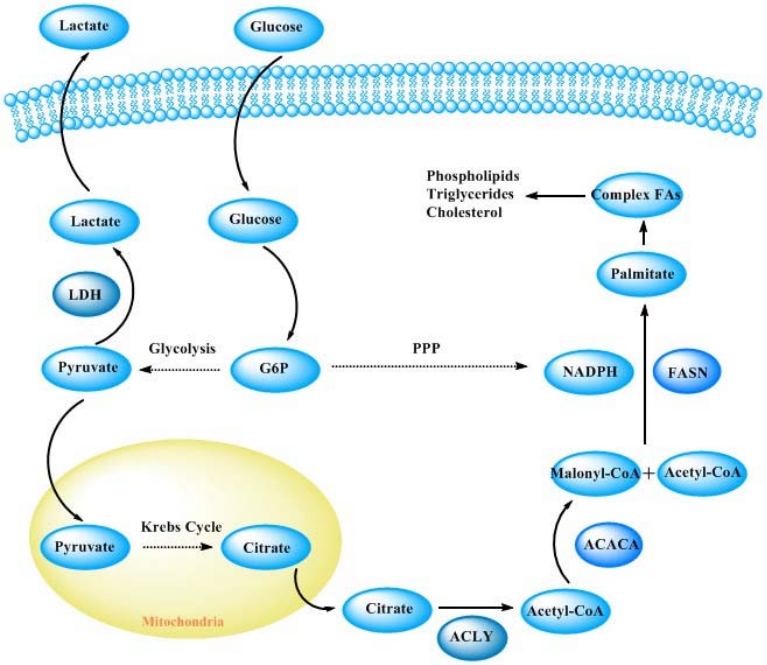

Figure 4.8. Biosynthesis of lipids.

As mentioned before, under hypoxic conditions cells use glutamine as a carbon source for synthesising lipids instead of glucose. HIF prevents pyruvate entry into the TCA cycle by inducing the expression of pyruvate dehydrogenase kinase 1 (PDK1). This enzyme phosphorylates and inhibits pyruvate dehydrogenase, therefore preventing pyruvate's conversion to acetyl-CoA. Studies have shown that hypoxia induces acetyl-CoA synthetase 2 which catalyses the synthesis of acetyl-CoA from cytosolic acetate. Furthermore, isocitrate dehydrogenase-1 is activated under hypoxia which produces citrate from glutamine-derived α-ketoglutarate.

In this work, unsupervised analysis did not clearly differentiate between MCF7 cells cultured under normal and hypoxic conditions, suggesting no/little change is occurring in the lipidome. The initial hypothesis was that as glycolysis increases under hypoxic conditions (as seen from the aqueous phase metabolites results), there

would be elevated levels of lipids as previously reported.[98] One proposal for the observed results could be that membrane lipids are present in such high concentrations, regardless of pO_2 perturbation, that they are masking other lipid classes that are primarily utilised for membrane synthesis. It is recognised that the sample set here was small and more are needed to make reliable conclusions. Furthermore, the acquired relative abundances of ions in the mass spectrum obtained for a mixture does not necessarily reflect the proportions of the compounds in the mixture. The ionisation ability of lipids also depends on many factors. While several compound reference databases already exist, an equivalent of a GenBank for MS spectral deposition is needed. This would allow users to insert referential MS metabolite spectra that can be shared with other scientists.

4.2.1 Method improvements

1) Mass spectrometry in general cannot discriminate isomers, therefore coupling to a chromatographic technique is recommended. This would make quantification more likely but there still exists the difficulty in positively identifying a lipid as different instruments produce different spectra. A second ionisation technique may help combat this problem. ESI tandem MS can be employed for locating double bond position in lipids.
2) A better extraction protocol could be used for future work because the $CHCl_3$:MeOH:H_2O method adopted here does not extract hydrophilic lipids like sphingosine-1-phosphate. Salts could be added to optimise extraction.[125] In addition, the choice of solvent is important as hexane:isopropanol were found to be best suited for extracting apolar lipids like triglycerides.

4.4/ Conclusion

Lipidomics is an emerging field of basic and translational research. Despite recent improvements in technology and bioinformatic tools, more attention must be paid in improving data interpretation for acquiring meaningful biological information.

FTICR MS provides a unique way to detect lipid distributions in a high-throughput manner with high spatial and spectral resolution. A non-targeted lipid analysis of MCF7 cells was acquired using FTICR MS under hypoxic and normoxic conditions but no clear differences were observed. Cellular membrane lipids dominated the spectra, probably to accommodate the high proliferative and energy-consuming rates of these cells.

Chapter 5: RNA-sequencing of MCF7 cells

5.1/ Introduction

Different cell types within our body have different structures and functionality, yet they all contain the same genetic information. This is all down to gene silencing – genetic information can be "turned off". The Central Dogma of Biology describes how DNA (the blueprint of genetic instructions) is transcribed into messenger RNAs (mRNAs) before being translated into proteins. MicroRNAs (miRNAs), which are small, single-stranded non-coding RNA molecules, are post-transcriptional regulators of protein-coding gene expression by binding to and inactivating targeted mRNA. MiRNAs have received considerable attention in recent years as drivers of tumour development and progression, and will, therefore, be explored here.

5.1.1 MiRNA: Biogenesis and Function

MiRNA (which were originally discovered in *Caenorhabditis elegans* in 1993) [126], [127] are commonly found within intergenic regions and introns of protein-coding genes. The formation and function of miRNA can be found in Table 1.

5.1.2 MiRNA: Role in Cancer

It is predicted that miRNA influence at least 30% of human genes with one miRNA usually targeting more than 100 genes.[121] MiRNAs influence and regulate cellular processes such as apoptosis, differentiation, proliferation, and metabolism. Given their widespread regulatory function, it is not unorthodox to link aberrant expression of miRNAs with diseases such as cancer, arthritis and neurodegenerative diseases.[20], [128] To characterise aberrant miRNA expression, transcriptomics can be used and combined with other *omics* studies for effective molecular phenotyping of cancers. An understanding of how miRNA expression effects downstream cellular

activities will increase the potential of discovering new cancer targets as aggressive tumours are still not responding to currently available therapeutics.

5.1.3 High-throughput sequencing of miRNA

RNA-sequencing (RNA-seq) is next-generation sequencing that can quantify RNA in a biological sample. Microarray analysis is one commonly used method to create a gene expression profile; however, its limitations, such as low sensitivity and its lack of a quantification method, make RNA-seq a more attractive technique in discovering novel biomarkers.[129] RNA-seq involves, firstly, the amplification of target RNA by solid phase PCR on a flow cell. Secondly, dye-terminators technology and engineered polymerases are used to sequence the RNA strands. Below is a flow diagram to describe this technology. 3 billion bases per run are read, and GenePool bioinformatics is used to analyse the chromotographs (Figure 5.1).

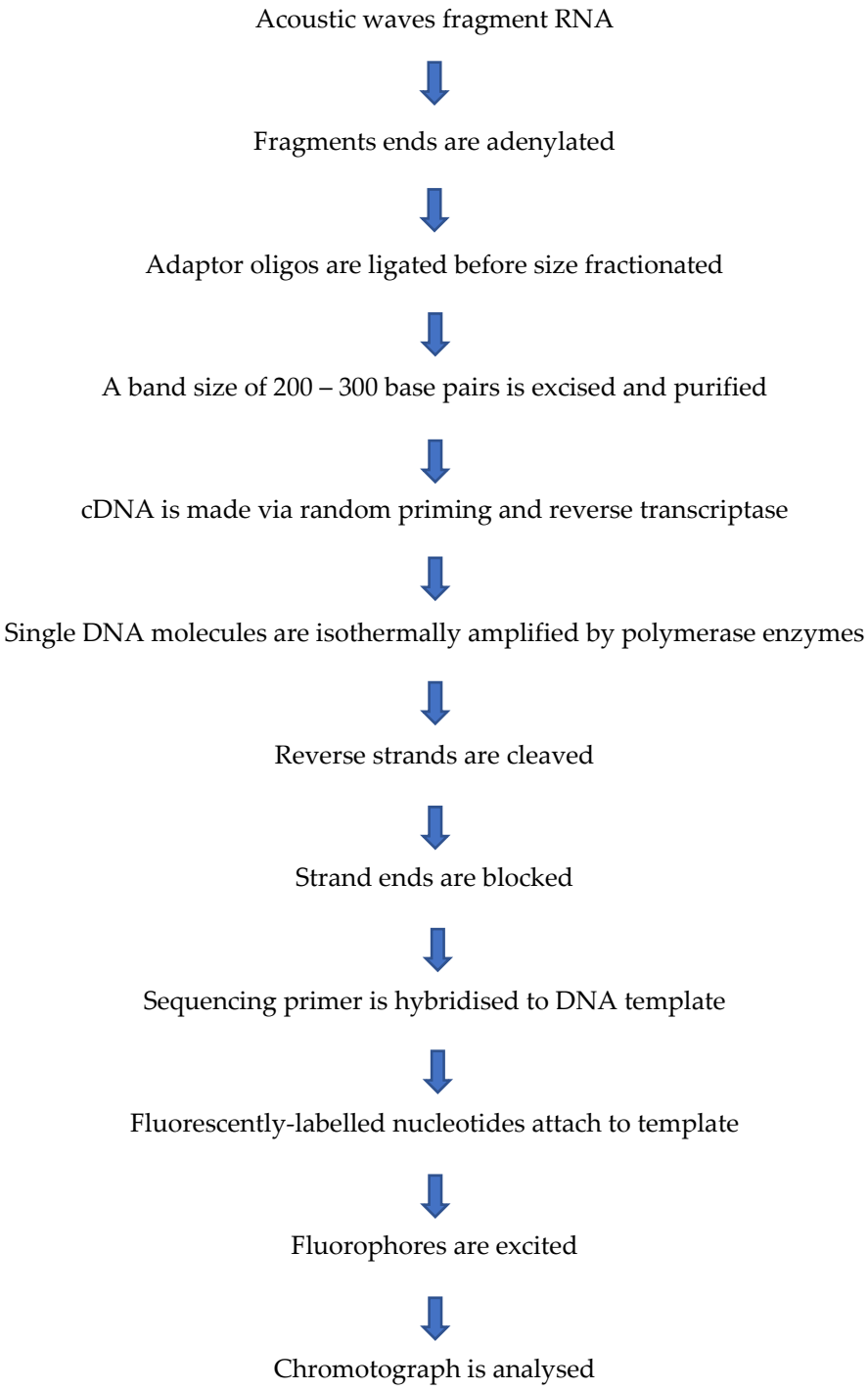

Figure 5.1. Flow diagram of RNA-seq.

Table 1. Flow chart of formation and function of miRNA.

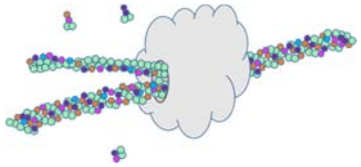	MiRNA are first transcribed by RNA polymerase II or III to form a primary transcript (pri-miRNA). This then folds into a hairpin loop, usually with some unpaired nucleotides and single strand extensions at both ends.
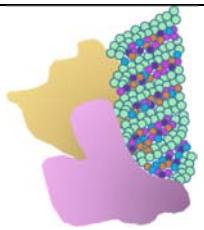	A nuclear RNase III enzyme, known as Drosha, binds to the pri-miRNA. It interacts with the binding protein called DiGeorge syndrome critical region gene 8 (DGCR8), to form a microprocessor complex. DGCR8 cleaves the extensions to form precursor miRNA (pre-miRNA).
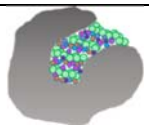	Exportin 5 binds to the double-stranded transcript and exports it from the nucleus into the cytoplasm where the transcript is released.
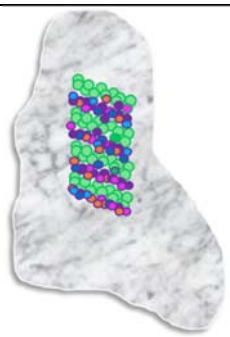	Once in the cytoplasm, DICER, another RNase III enzyme, cleaves the stem-loop to a shorter double stranded miR:miR* duplex with 5′ monophosphate and 3′ overhangs of two nucleotides.
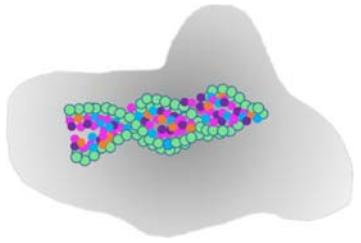	An argonaute protein, AGO 2, interacts with DICER to bind with the miRNA. AGO 2 causes the miRNA to unwind and removes the passenger strand, leaving the guide strand of the mature miRNA. The guide strand, AGO 2 and the addition of other proteins, creates the RNA-induced silencing complex (RISC). This complex is guided by the guide strand to target and inactivate one or multiple genes.
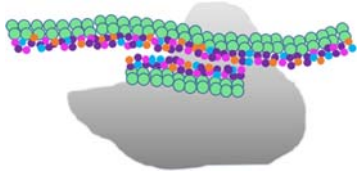	The mRNA of a target gene is complementary to the sequence of the mature miRNA to allow for base-pairing. RISC can inactivate mRNA in two ways: firstly, RISC inhibits translation by preventing a ribosome subunit from binding to translate the mRNA into a protein; secondly, proteins within the RISC can simply cleave the mRNA which would be further destroyed by the cell. [138, 139]

Metabolic profiling can give an instantaneous snapshot of the physiology of that cell; however, combination with transcriptomics (the study of mRNA) would provide a

broader insight into cellular activity, reflecting on the state of the system and the underlying mechanisms that drive malignancy transformation. The technological development of high-throughput generation of transcriptomic data helps to further understand the complexity of cancer cells. RNA-seq has, to our knowledge, not been used to study MCF7 cells and to observe how physical perturbations influence miRNA expression. The aim of this work here was to use RNA-seq to quantify miRNA as they control the stability and translation of mRNA. The aim is to discover which miRNA networks contribute to deviation from the balanced state under perturbed pO_2 and to link these results with the downstream metabolic data.

5.2/ Results

5.2.1 RNA Extraction

Triplicate samples for each pO_2 condition of MCF7 cells were cultured and extracted, once confluent, using the MiRNeasy Mini Kit. Successful nucleic acid extraction and purification involves the following steps: effective cell disruption; protein denaturation; nuclease inactivation; removal of contaminates. RNA is less stable than DNA, therefore special care must be taken to prevent RNA degradation. Salt is a common impurity in nucleic acid samples which is removed through several purification steps.

The MiRNeasy Mini Kit protocol, in short, includes an acid guanidinium thiocyanate-phenol-chloroform extraction which inhibits the action of RNases (nucleases which degrade nucleotides) and has on-column DNase digestion. The phenol-chloroform solution creates a phase separation consisting of polar and non-polar components. Guanidinium thiocyanate is a chaotropic agent and, therefore, degrades proteins and RNases. The pH of the solution is acidic so RNA partitions into the aqueous phase (due to the presence of a 2′-hydroxyl group on the ribose subunit) while DNA and lipids partition into the interface or organic layers.

5.2.2 RNA Quality Control Analysis

Initial quality control (QC) measurements were conducted using a Nanodrop UV-Vis spectrophotometer to give an indication of the quantity and purity of total RNA extracted (Figure 5.2). This method requires ~1 μL of sample which is pipetted onto a pedestal. A surface water column is created between the pedestal and the arm placed on top to direct UV light through. The maximum absorbance of light of nucleic acids peaks at approximately 260 nm, therefore how much light is detected depends on the quantity of nucleic acids in the sample. The presence of proteins and other contaminates absorb strongly at ~280 nm. The ratio of absorbance at 260 nm and 280 nm is used to assess the purity: the accepted ratios ~1.8 and ~2.0 for DNA and RNA, respectively. All RNA samples in this work produced a 260:280 ratio ranging from 2.01 – 2.07 and, after dilution, had concentrations of around 300 ng/μL.

These diluted samples were run on a Bioanalyser to analyse RNA integrity with a resulting value of 10 being optimum. Briefly, samples are placed on a microfabricated chip which contains microchannels. The channels are filled with a sieving polymer and fluorescence dye. Electrophoresis separates nucleic acid fragments based on size, similar to gel electrophoresis. The dye markers, which intercalate with nucleic acids, are detected by laser-induced fluorescence. Results can be viewed as a gel-like image or as an electropherogram. On comparison with an internal standard ladder of known size, a standard curve of migration time vs. fragment size is plotted. From the migration times of each nucleic acid fragment, their size is calculated. The ribosomal RNA (rRNA) ratio is determined and the RNA integrity number (RIN) is given. rRNA constitutes over 80% of total RNA which is easily detected compared to mRNA which constitutes only 1-3%. rRNA are composed of mostly 28S and 18S types (S = Svedberg unit) in mammalian cells. Because the size of 28S and 18S are 5 kb and 2 kb, respectively, the theoretical ratio is approximately 2.7:1 (28S:18S); however, a ratio of 2:1 is generally considered the baseline for intact RNA. 28S rRNA is presumed to degrade faster than the 18S species and, so, the ratio would decrease. RIN software allows for a more accurate classification of RNA degradation.[130] My samples

produced RIN numbers from 8.8 – 9.7, indicating very little RNA degradation had occurred.

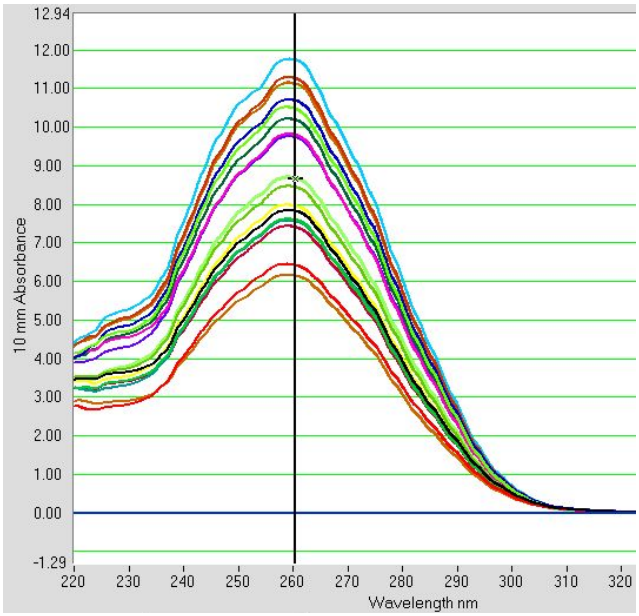

Figure 5.2. NanoDrop UV-Vis results of extracted RNA from MCF7 cells. No humps are observed at ~280 nm which would indicate contamination.

5.2.3 RNA Library Preparation

Before submitting my samples to Edinburgh Genomics for RNA-seq, a collaborator, Paul Dickinson, made a pool of 15 small RNA libraries using TriLink barcodes. Briefly, CleanTag adaptors were added to both 3′ and 5′ ends. Complementary DNA (cDNA) of the tagged RNA library were made through reverse transcription (RT) before being amplified through Polymerase Chain Reaction (PCR). The amplified RT product was run on an agarose gel and the band at 140+ base pairs (bp), which coincided with tagged RNA, was cut and analysed using the Bioanalyser to check its size. From Figure 5.3, the sample had 3 bands, one at 120 bp (adaptor only - 8.9% of

total), one at 129 bp (adapter + unknown - 33% of total sample) and one at 143 bp (adapter + miRNAs - 58.1% of total sample).

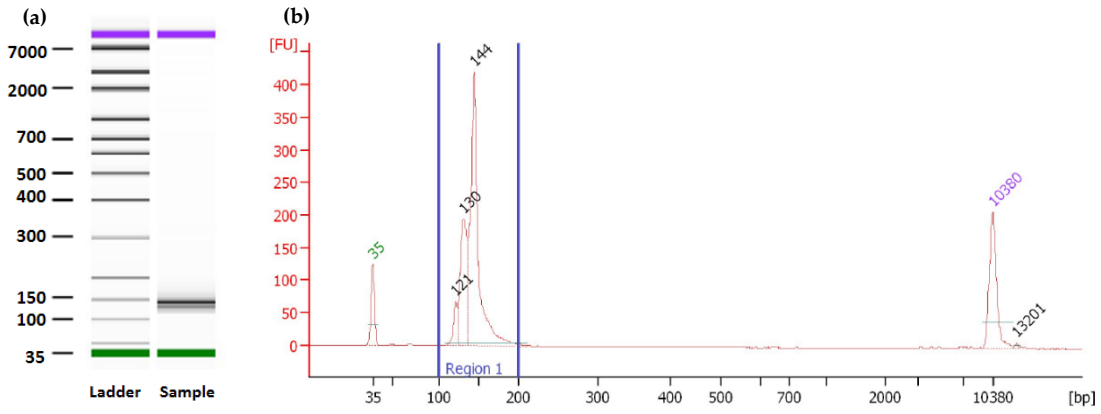

Figure 5.3.(a) Electrophoresis run and (b) electropherogram Bioanalyser results of RNA library pool. Bands at 35 bp and 10,380 represent upper and lower markers.

5.2.4 Surprisal Analysis

As a reminder, surprisal analysis (SA) applies principles of thermodynamics by first calculating the balanced state of maximal entropy and minimal free energy in which the biological system can no longer initiate or participate in spontaneous reactions. Next, SA determines sets of, in this case, miRNA molecules which collectively represent a change in phenotype from the balanced/reference state. A phenotype change causes an increase in the free energy as energy is needed to constrain the system from maximal entropy. Several of these different phenotypes are usually sufficient in quantitatively describing the observed expression levels of extracted miRNA. The phenotypes are ranked in order by their fold change from the balanced state, i.e. by how much each collection of transcripts deviates away from the balanced state of maximal entropy to a state of lowered entropy.

The miRNA counts are represented as matrix X consisting of 5 columns (n) and 610 rows (m): one column is for each pO_2 and each row is the transcript abundance. The

average was taken of the 3 replicates for each condition and then natural log scaled. It should be noted that the triplicate results are not identical, indicating some experimental variability. SA was conducted to rank the system's constraints in order of influence by how much they reduce the entropy from the reference state. Constraint one has the biggest influence on the transcript profile transitioning. The number of constraints that should added to the model is decided based on how well they approximate the raw data with as little information as possible. Figure 5.4 represents the extent of reproduction of the experimental data using one or the sum of two or more constraints. It can be seen that addition of one constraint, and its associated transcription patterns, suffices in modelling the main characteristics and trends of the log-scaled raw data as it provides a high-quality fit. If all constraints were included, as in Figure 5.4e, a mathematically exact reproduction would be made, including all inherent noise.

SVD produces another matrix which is independent of oxygen concentration, stating the magnitude of biological significance that miRNAs have on a particular constraint/phenotype. This matrix is expressed as a G plot (Figure 5.5) which ranks the transcripts in terms of free energy changes. The sign of the transcript indicates the mode of its participation, whether it is downregulated or upregulated. Those transcripts that had a fractional level ±0.6 were included for further interpretation. Since only one constraint has been chosen to model the system, transcripts that contribute to that phenotype are listed in Table 2 &
Table 3, including 60 upregulated and 14 downregulated miRNAs.

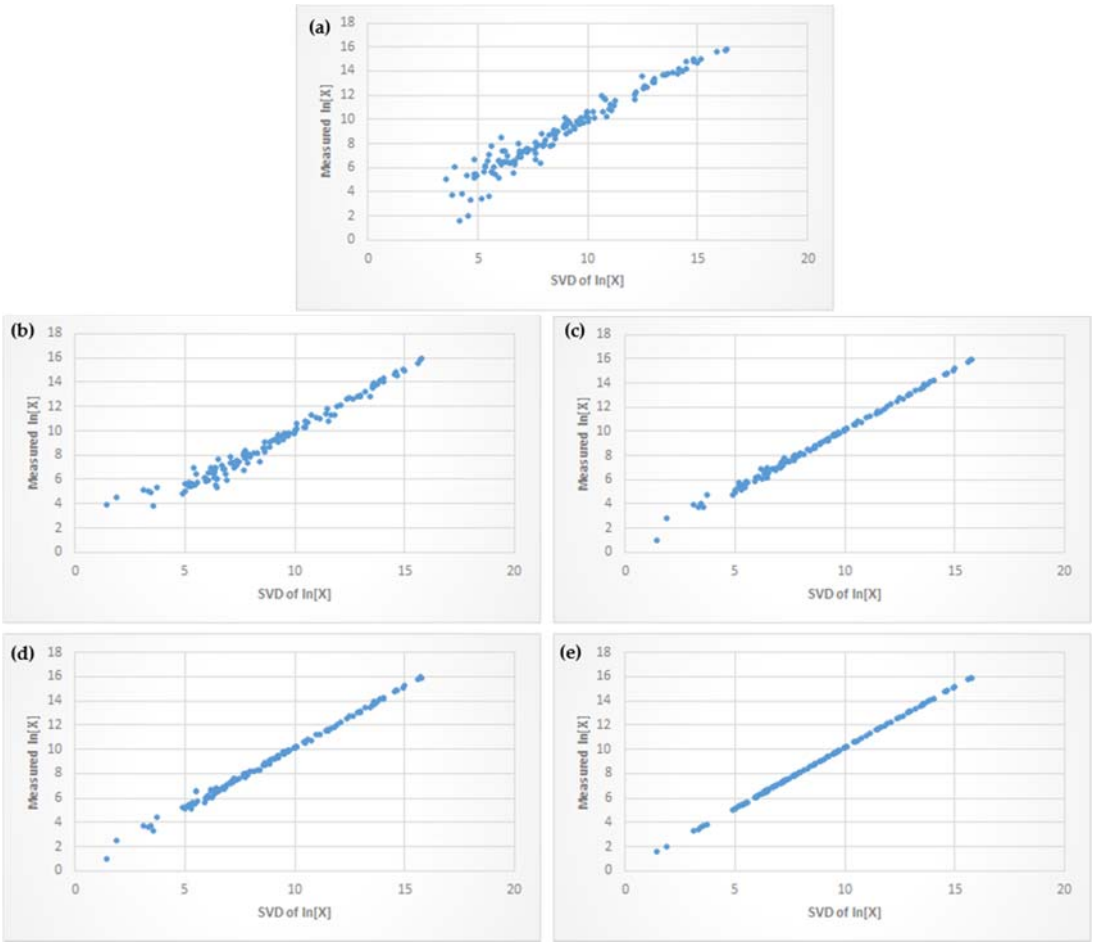

Figure 5.4. Scatter plots of measured transcript levels versus computed values of miRNA from MCF7 cells in (a) balanced state and with (b) one, (c) two, (d) three and (e) four constraints.

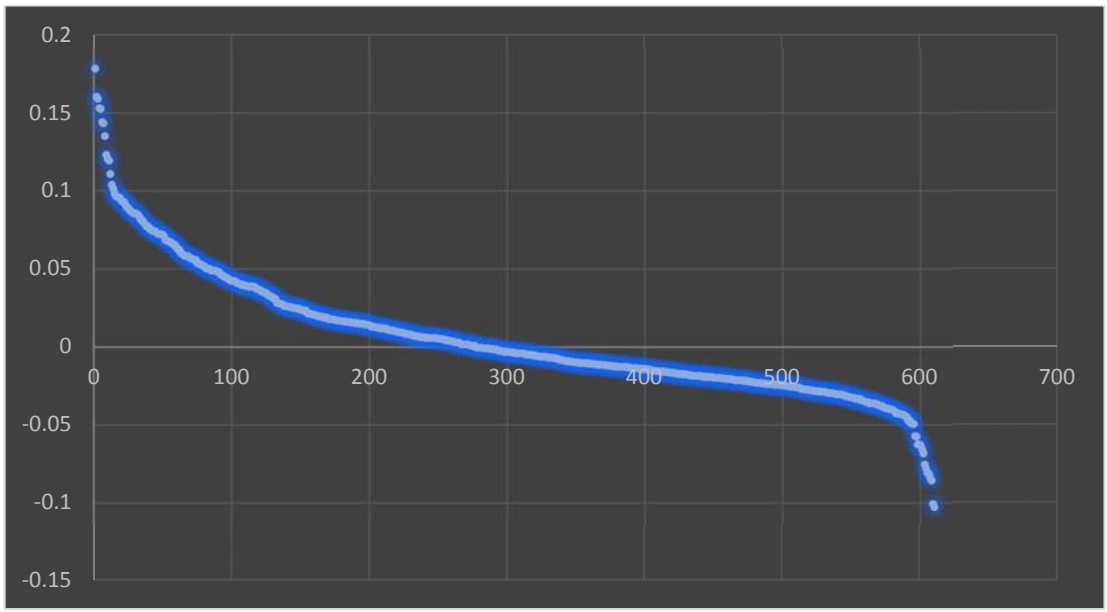

Figure 5.5. G plot of free energy change of metabolites vs. metabolite number of miRNA from MCF7 cells on addition of one constraint.

Table 2. RNA transcripts with greatest positive free energy changes from the balanced state, on addition of one constraint to the system, in descending order of importance down the column and continues from left to right.

Most highly upregulated miRNAs				
hsa-mir-381	**hsa-mir-1266**	**hsa-mir-450a-1**	**hsa-mir-410**	**hsa-mir-6516**
hsa-mir-2278	**hsa-mir-1286**	**hsa-mir-487a**	**hsa-mir-22**	**hsa-mir-370**
hsa-mir-370	**hsa-mir-4707**	**hsa-mir-643**	**hsa-mir-3609**	**hsa-mir-3607**
hsa-mir-1261	**hsa-mir-99a**	**hsa-mir-369**	**hsa-mir-106**	**hsa-mir-551b**
hsa-mir-411	**hsa-mir-326**	**hsa-mir-665**	**hsa-mir-6768**	**hsa-mir-6716**
hsa-mir-7703	**hsa-mir-188**	**hsa-mir-218-1**	**hsa-mir-20b**	**hsa-mir-6862-1**
hsa-mir-501	**hsa-mir-2116**	**hsa-mir-493**	**hsa-mir-377**	**hsa-mir-329-1**
hsa-mir-485	**hsa-mir-203b**	**hsa-mir-106a**	**hsa-mir-5094**	**hsa-mir-629**
hsa-mir-3177	**hsa-mir-548y**	**hsa-mir-195**	**hsa-mir-3174**	**hsa-mir-615**
hsa-mir-4676	**hsa-mir-331**	**hsa-mir-548w**	**hsa-mir-194-2**	**hsa-mir-450b**
hsa-mir-6724-1	**hsa-mir-185**	**hsa-mir-1273d**	**hsa-mir-3180-1**	**hsa-mir-4725**
hsa-mir-3651	**hsa-mir-1224**	**hsa-mir-6860**	**hsa-mir-4677**	**hsa-mir-382**

Table 3. RNA transcripts with greatest negative free energy changes from the balanced state, on addition of one constraint to the system, in descending order of importance down the column and continues from left to right.

Most highly downregulated miRNAs	
hsa-mir-210-3p	**hsa-mir-5010**
hsa-mir-675	**hsa-mir-212**
hsa-mir-1910	**hsa-let7f-2**
hsa-mir-483	**hsa-mir-29c**
hsa-mir-210-5p	**hsa-mir-548h-4**
hsa-mir-335	**hsa-mir-342**
hsa-mir-556	**hsa-mir-483**

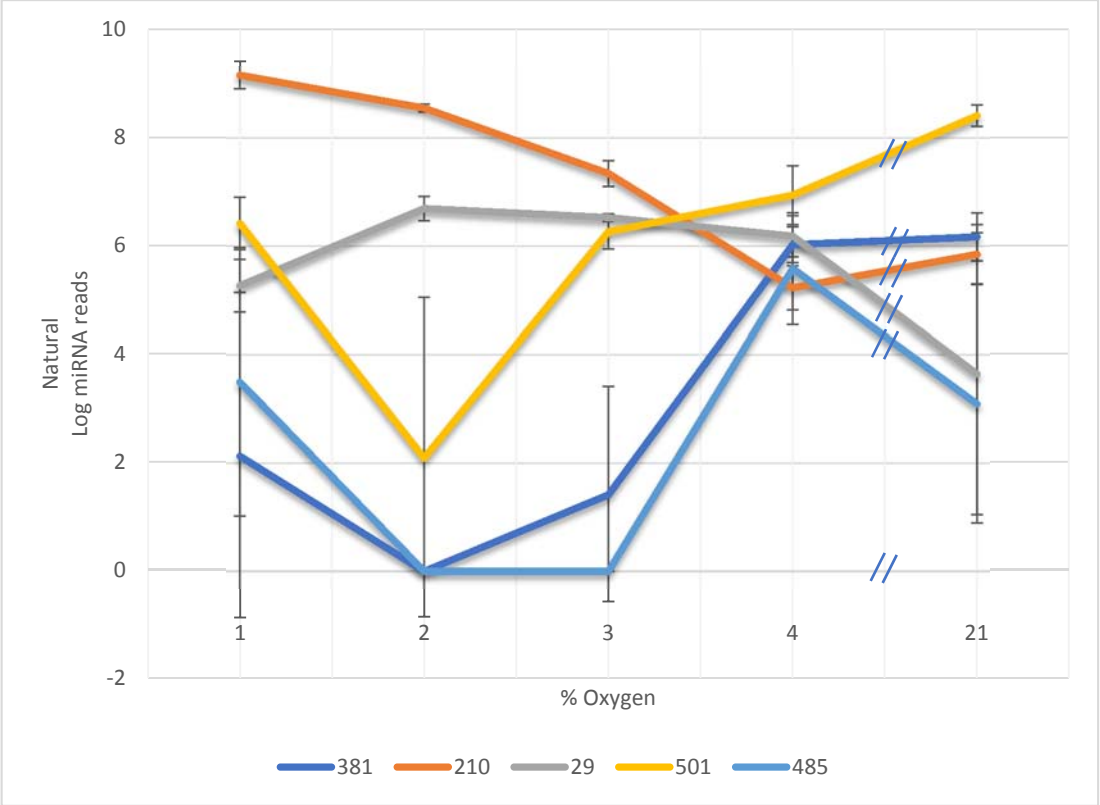

Figure 5.6. Change of miRNA expression at varying pO_2 with standard deviation error bars.

From Figure 5.6, it can be seen that, with most transcripts of interest, a change is occurring from 2-4% pO_2. At 1% pO_2, transcript levels are going in the opposite direction from 2% pO_2 which may be a cellular response to stress. 21% pO_2 is the standard incubation condition for tissue culture but is not actually the physiological level for cells, therefore SA was repeated but excluding data for 1% and 21% pO_2.[131] As can be seen from Table 4 and Table

Table 5, the highlighted miRNAs are also present in the initial analysis in Table 2 and Table

Table 3. This gives a good indication that the initial model is robust and that the trends observed from 2-4% pO_2 are true. *P*-values for miRNAs of interest can be found in Appendix B.

Table 4. RNA transcripts with greatest positive free energy changes from the balanced state, on addition of one constraint to the system, in descending order of importance down the column and continues from left to right. 1% and 21% pO_2 data has been excluded from the anaylsis. Those highlighted in red are found in the original model.

Most highly upregulated miRNAs				
hsa-mir-411	hsa-mir-2278	hsa-mir-6724-1	hsa-mir-495	hsa-mir-185
hsa-mir-370	hsa-mir-1286	hsa-mir-99a	hsa-mir-6735	hsa-mir-106a
hsa-mir-381	hsa-mir-1261	hsa-mir-6716	hsa-mir-331	hsa-mir-6860
hsa-mir-377	hsa-mir-4676	hsa-mir-195	hsa-mir-450a-1	hsa-mir-4677
hsa-mir-758	hsa-mir-218-1	hsa-mir-548y	hsa-mir-6767	hsa-mir-3609
hsa-mir-485	hsa-mir-369	hsa-mir-3139	hsa-mir-539	hsa-mir-203b
hsa-mir-122	hsa-mir-3651	hsa-mir-450b	hsa-mir-4787	hsa-mir-4677
hsa-mir-370	hsa-mir-493	hsa-mir-6882	hsa-mir-548w	hsa-mir-382
hsa-mir-3177	hsa-mir-10b	hsa-mir-4707	hsa-mir-1273d	hsa-mir-3174
hsa-mir-487a	hsa-mir-20b	hsa-mir-329-1	hsa-mir-410	hsa-mir-2116
hsa-mir-501	hsa-mir-326	hsa-mir-329-1	hsa-mir-541	hsa-mir-3607
hsa-mir-7703	hsa-mir-188	hsa-mir-6505	hsa-mir-22	hsa-mir-26a-2
hsa-mir-643	hsa-mir-665	hsa-mir-6516	hsa-mir-1266	hsa-mir-6862-1

Table 5. RNA transcripts with greatest negative free energy changes from the balanced state, on addition of one constraint to the system, in descending order of importance down the column and continues from left to right. 1% and 21% pO_2 data has been excluded from the analysis. Those highlighted in red are found in the original model.

Most highly downregulated miRNAs		
hsa-miR-675	hsa-mir-210-5p	hsa-mir-483
hsa-miR-483	hsa-mir-1910	hsa-mir-1250
hsa-miR-210-3p	hsa-mir-3939	hsa-mir-3064
hsa-miR-556	hsa-mir-342	hsa-mir-503

5.3/ Discussion

Since 1993, our knowledge of miRNAs has been exponentially growing. The function of many identified miRNAs is still unclear but it is thought that their aberrant expression is linked to the development and progression of cancer. The silencing mechanism, in which miRNAs negatively regulate the expression of their target mRNA in eukaryotes, was first discovered in 2003.[132] Activated RISC binds target mRNA between the guide strand of the mature miRNA and the 3'UTR of the target. Depending on the level of base complementarity, mRNA are either cleaved, and subsequently degraded, or their translation to proteins is inhibited. The mechanisms for miRNA dysregulation are poorly understood but it is these alterations that are potentially critical for determining how changes in oxygen concentration lead to changes in tumour phenotype such as sensitivity to therapy and metastatic potential.

RNA-seq provides a comprehensive view of the transcriptome and, unlike microarrays, is not dependent on any prior sequencing knowledge. The technology provides absolute quantifiable information through digital read counts which are aligned to a particular sequence. SA then draws out the biologically relevant information by characterising biomolecule dynamics based on their expression level across a range of conditions. The main phenotype that deviates the most from the global maximum state in this work (Figure 5.5) includes 3 groups of transcripts: (1) a large set whose expression levels hardly change; (2) a group with gradual induction in expression; (3) a small group with gradual reduction in expression. SA revealed a signature of 74 differentially expressed miRNAs between MCF7 cells cultured under varying pO_2 conditions.

It is difficult to determine if altered expression profiles of miRNA is a direct result of cancer or indirect due to downstream phenotype changes. Furthermore, one miRNA can regulate many genes; it is possible that one miRNA is an oncogene in one context and a tumour suppressor in another. MiRNA expression can be controlled by

transcription factors in response to endogenous or exogenous stimuli with evidence already suggesting that hypoxia is one such stimulus.

The miRNAs highlighted below that deviate from the balanced state are affiliated with the hallmarks of cancer.

5.3.1 RNA transcripts with greatest negative free energy changes

MiR-210

It is observed that miR-210 has the greatest positive free energy contribution in deviating the system from the balanced state. Hypoxia-induced miR-210 expression leads to aberrant regulation of normal cellular processes by altering proteins that regulate mitochondrial function, DNA stability and cell proliferation.[133], [134] More specifically, hypoxia-inducible factors (HIF), which are master regulators of the cellular hypoxic response, increase the expression of miR-210 and, in turn, miR-210 stabilises HIF-1α by inhibiting prolyl hydroxylases which degrade HIF-1α.[135], [136] Furthermore, it is thought that miR-210 indirectly activates c-MYC which is linked to cell-cycle progression.[137]

Under hypoxic conditions, cells acquire energy through glycolysis rather than the TCA cycle by stimulating glycolytic proteins or inhibiting mitochondrial proteins. Proteins involved in normal mitochondrial respiration, such as *iron-sulfur (Fe-S) cluster* assembly proteins 1 and 2 (ISCU1) and (ISCU2), are suppressed under hypoxic conditions. Fe-S clusters also play important roles in cellular reactions. The most common Fe-S clusters in eukaryote cells are [2Fe-2S] and [4Fe-4S] complexes which usually coordinate with proteins via cysteine residues. Factors such as redox potential and oxidation state dictate the ability of these clusters to catalyse reactions, stabilise proteins or participate in redox reactions.[138], [139] ISCU1 and ISCU2 are components of complexes I-III of the electron transport chain and aconitase which is involved in the TCA cycle. MiR-210 downregulates ISCU1 and 2, thus promoting the shift from OXPHOS to glycolysis and lactate fermentation. This change in metabolism

may be energy inefficient, as glycolysis produces only two molecules of ATP per glucose molecule, but lactate fermentation produces NAD^+ which aids in cell proliferation.[138], [140] From Figure 5.6, it can be seen that the abundance of miR-210 is especially high at 1% pO_2, and tapers off at 4% pO_2, correlating well with previous findings. These results coincide well with the metabolic data: lactate and NADH were important contributors to a change in phenotype in MCF7 cells.

As a side note, premature transfer of electrons across the mitochondrial complexes can result in increased ROS generation. However, a cellular adaptive response to toxic levels of radicals is hypoxia-induced pyruvate dehydrogenase kinase 1 (PDK1) and lactate dehydrogenase A (LDHA) overexpression which prevent the conversion of pyruvate to acetyl-CoA and instead into lactate. This process reduces the levels of NADH and FADH being delivered to the ETC.[86]

MiR-675

Orphan G-protein-coupled receptor 55 (GRP55) is a suspected target of miR-675 in lung cancer cells; miR-675 is downregulated as it inhibits tumour growth through GRP55 suppression (a modulator of migration).[141] The latter was present in lower levels in MCF7 cells compared to more aggressive breast cancer subtypes in previous studies.[142]

MiR-335

MiR-335 is upregulated in certain cancers and is involved in oncogenic signalling such as the well-known p53, mTOR and TGF-β pathways.[143]–[145] MiR-335 tightly regulates retinoblastoma 1 (Rb1) which controls cell cycle genes and tumour suppression. If there is aberrant expression of Rb1, miR-335 activates the p53 pathway to reduce cell proliferation.[145] MiR-335 was reported to be positively correlated to the tumour suppressor gene breast cancer 1 (BRCA1) cascade which is often mutated in breast cancers.[144]

MiR-Let-7f

Previous research has shown that several let-7s are tumour suppressors, targeting the well-known Ras and high mobility group AT-hook 2 (HMGA2) oncogenes. Let-7s regulate these two oncogenes via 3'UTR binding which inhibits translation. Ras and HMGA2 inhibitors for potential cancer treatment are of interest due to the oncogenes' roles in signalling for cell proliferation and survival. It is also thought that Let-7s inhibit cell cycle regulators such as c-MYC.[146], [147]

MiR-29

MiR-29 is a well-known tumour suppressor but may act as an oncogene under certain conditions or cell lines. As a tumour suppressor, the transcript has several methods of restraining tumour growth. Firstly, by promoting apoptosis through a p53-dependent manner and through upregulation of pro-apoptotic genes such as Bcl-2-like protein 11 (BIM).

Secondly, miR-29 suppresses DNA methylation of other tumour suppressor genes. *Wang et al.* reported that the expression of DNA methyltransferases by miR-29 caused hypomethylation in the phosphatase and tensin homolog (PTEN) promotor and its subsequent overexpression in pancreatic cancer. On the contrary, miR-29 was found to repress PTEN in breast cancer cells.[148] PTEN is a tumour suppressor by negatively regulating the Akt/PKB signalling pathway, which promotes cell growth,[149], [150] and reduces proliferation through insulin-like growth factor 1 (IGF-1) inhibition.[151], [152] ROS also inactivate PTEN through oxidising a residue in the catalytic domain, making an intramolecular disulfide bond between two cysteines.[153] Furthermore, *Parsons et al.* discovered that overoxidation of the cysteine thiol in the active site of protein tyrosine phosphatases, like PTEN, to the cyclic sulfinyl or sulphonamide forms prevents catalytic activity recovery by reducing agents.[154]

Thirdly, miR-29 mediates epithelial-mesenchymal transition (EMT) through possible downregulation of a breast cancer associated gene known as ADAM12. The metalloprotein coded by ADAM12 catalyses cleavage of transmembrane receptors, growth factor precursors or adhesion molecules.[155]

NF-κB, a family of transcription factors which regulate genes involved in inflammation and cell survival, activates the transcriptional repressor protein Ying Yang 1 (YY1) which then downregulates miR-29.[156] NFκB is known to rapidly respond to hypoxic conditions and ROS, the mechanism of which was suggested by *Culver et al*. During hypoxia stress, calcium ions are released from intracellular compartments which are mediated by a family of serine/threonine kinases called calcium/calmodulin-dependent kinases (CaMKs). This induces IκB kinase (IKK) activity which phosphorylates IκBα bound to NF-κB. IκBα dissociates, releasing NF-κB which subsequently is translocated to the nucleus for the transcription of mRNA.[157] SA has highlighted miR-29 as a downregulated transcript, possibly caused by the hypoxia-induced expression of NF-κB.

5.3.2 RNA transcripts with greatest positive free energy changes

MiR-381

MiR-381 was found to contribute the most thermodynamically to the main phenotype. Acting as a potential tumour suppressor, it has been reported that miR-381 is downregulated in various cancers and targets connexin43 (Cx43), an enhancer of breast cancer metastasis through cell invasion and migration.[158] Studies have shown that miR-381 is involved in EMT.[158], [159] Here, epithelial cells lose cell-cell adhesion and become migratory mesenchymal cells, passing into the bloodstream and invading healthy cells. The process is mediated by E-cadherin repression, a transmembrane protein present in epithelial cells at high levels.[160] Transforming growth factor beta (TGF-β) induces EMT which causes the upregulation of transcriptional repressors such as the interestingly named Cys_2His_2-type zinc-finger

proteins Slug, Snail and Zeb1. These proteins bind to the promoter of genes encoding E-cadherin and prevent their expression.[161] Interleukin-6 (Il-6) was also found to induce EMT in cervical cancer.[162] Consistent with previous studies, miR-381 is downregulated in MCF7 cells, especially under hypoxic conditions. At 1% and 3% pO_2, it should be noted that one of the 3 replicates for each condition contained high reads of miR-381 compared to the others which had no reads, therefore skewing the results.

MiR-2278

Research has shown that this miRNA acts as a tumour suppressor in myeloid leukaemia, targeting the JAK/STAT pathways which play roles in proliferation, migration and apoptosis.[163]

MiR-370

Yamane et al. hypothesised that miR-370 is a negative regulator of SLD5 in bladder cancer. SLD5 is important in the assembly of the DNA replication GINS complex. MiR-370 was found to be negatively regulated in this cancer model, leading to the upregulation of SLD5 and tumour growth. Il-6 is thought to induce the suppression of miR-370.[164]

MiR-411

Growth factor receptor-bound protein 2 (GRB2) is involved in signal transduction and communication and is suspected of being a downstream target gene of miR-411. Previous research has linked GRB2 overexpression with breast cancer metastasis. In addition, miR-411 overexpression was found to reduce levels of mRNA and proteins of GBR2.[165], [166]

MiR-501

MiR-501 increases activation of mechanistic target of rapamycin (mTOR) signalling in renal carcinoma, resulting in increased tumour growth and survival. Upregulation

of miR-501 has been observed in breast cancer studies.[167] mTOR is a master regulator of translation and is inhibited under hypoxic conditions.[168] Figure 5.6 shows a dip at 2% pO_2 of miR-501 reads, however there is a high standard deviation between the replicates.

MiR-485

Low levels of miR-485 were found in previous studies on breast cancer cells. The transcript's expression is suggested to be inversely correlated to cell proliferation.[169], [170] *Lou et al.* suggested that miR-485 has a suppressive role on mitochondrial function by directly targeting and inhibiting peroxisome proliferator-activated receptor gamma coactivator 1-alpha (PGC-1α) which is a master regulator of mitochondrial biogenesis and OXPHOS and promotes ATP production.[169], [171] Hypoxic conditions appeared to promote PGC-1α expression to detoxify ROS through direct induction of catalase, glutathione peroxidase and superoxide dismutase II.[172] MiR-485 levels are low in very hypoxic regions but spike at 4% pO_2. Perhaps this is to inhibit PGC-1α activity during hypoxia to reduce OXPHOS and promote metabolic transitioning to anabolic pathways.

Many of these miRNAs have also been implicated in various cancers but a thorough validation of these miRNAs in clinical trials is imperative. Furthermore, miRNA expression is tissue specific and their underlying mechanisms and prognostic value have yet to be ascertained.[9]

5.4/ Conclusion

Recent advances in genome technology has accelerated the rate of discovery science. This work has revealed sets of miRNAs associated with perturbed pO_2. MiRNA research is a new and exciting field of molecular biology. Significant effort has been made in identifying individual or a compilation of modulated transcripts that characterise the driving forces of malignancy transformation. Further investigation,

however, is needed to fully characterise the functional mechanisms and targets of miRNAs to advance our understanding of cancer initiation and progression.

Chapter 6: Redox Potential and ROS Measurements of Normoxic and Hypoxic Cells

6.1/ Introduction

Intracellular redox potential (IRP) is critically important for normal cell function, dysregulation of which can lead to initiation and progression of disease. Subtle changes in IRP can impact cell signalling and bioenergetics such as the metabolic profile. It is, therefore, a main goal of this work to investigate whether there is a correlation between the metabolic and transcriptomic profiles of MCF7 cells and redox potential.

The level of intracellular reactive oxygen/nitrogen species (ROS/RNS) is carefully monitored to sustain redox balance and efficient cellular signalling. Lipid peroxidation and enzyme inactivation are some of the consequences of significant increases in ROS caused by overproduction or the cell's inability to neutralise and remove.[173], [174] Maintaining oxygen homeostasis requires the regulation of a variety of different genes. If cellular oxygen levels are inadequate, respiration switches over to anaerobic glycolysis to sustain ATP production.[175] Intermittent hypoxia (alternating hypoxia and reoxygenation stages) and oxidative stress are induced by fluctuations in cellular oxygenation which in turn affects the following transcription factors: hypoxia-inducible factor (HIF-1), a regulator of the expression of genes important for adapting cells to hypoxia; nuclear factor (erythroid-derived 2)-like 2 (Nrf2) and nuclear factor κB (NF-κB), inducers of antioxidative enzymes.[176]

6.1.1 HIF-1 and its role in redox homeostasis

HIF-1, a heterodimer, constitutes the regulatory HIF-1α and catalytic HIF-1β subunits. HIF-1α is stabilised under hypoxic conditions because prolyl hydroxylase enzymes (PHDs) require oxygen in order to oxidise HIF-1α (labelling it for ubiquitination), therefore HIF escapes degradation.[93] HIF-1α is activated, forms a

dimer with HIF-1β and binds to the hypoxia-responsive element in the regulatory DNA sequence when hydroxylation by prolyl and asparaginyl hydroxylases (FIHs) is inhibited. Once stabilised, HIF-1α translocates to the nucleus where it heterodimerises with HIF-1β to form the active transcription factor.[177]–[181] HIF-1α is thought to be a key mediator of the Warburg effect and it is, thus, important to gain a better understanding of oxygen sensing and signal transduction. More than 100 target genes of HIF-1α have been identified which control such processes as energy metabolism, angiogenesis and erythropoiesis.[178], [182]–[184]

6.1.2 Nrf2 and its role in redox homeostasis

Nrf2 is the major regulator of cytoprotective responses to oxidative and xenobiotic damage. During normoxia, Nrf2 is sequestered in the cytosol by Kelch-like ECH-associated protein 1 (Keap1) where it is constantly ubiquitinated by the Cul-Keap1 ubiquitin E3 ligase complex and then subsequently degraded. The cysteine rich intervening region (IVR) of Keap1 contains a nuclear export signal. Here lie the reactive cysteines (Cys151, 273, and 288) that are essential for Nrf2 regulation. Cys151 is the likely major site for alkylation by Nrf2 inducers, whereas Cys273 and 288 repress the Nrf2 pathway. The mechanism by which these amino acids function by sensing the redox imbalance remains elusive.

Upon exposure to ROS/RNS or electrophiles, reactive cysteine residues of Keap1 become oxidised which induces a conformational change. Nrf2 is no longer bound to Keap1, thereby becomes stabilised and translocates to the nucleus where it associates with the antioxidant response element (ARE) and induces the transcription of a battery of cytoprotective genes such as superoxide dismutase and thioredoxin.[185]–[187]

6.1.3 NF-κB and its role in redox homeostasis

NF-κB plays a key role in proliferation, immunity and inflammation. It, too, is sequestered in the cytosol by I-κB until the latter is phosphorylated by I-κB kinase and ubiquitinated. NF-κB translocates to the nucleus where it induces the activation of antioxidants similar to Nrf2. Hypoxic conditions have been found to stimulate I-κB phosphorylation of a tyrosine residue.[188]

6.1.4 Previous work in measuring redox status of hypoxic cells

Growing evidence suggests that ROS generation from complex III of the electron transport chain is greater under hypoxic conditions. Fluorescence resonance energy transfer (FRET) was used to assess thiol oxidation of a ROS-sensitive probe consisting of cyan and yellow fluorescent proteins. *Guzy et al.* found that H_2O_2 increases at 1.5% pO_2 in live osteosarcoma cells.[189] RoGFP proteins have been used to assess oxidant status of subcellular compartments. Thiol reduction and oxidation of the protein's cysteine residues produce reciprocal changes in emission when excited at 405 and 488 nm. *Waypa et al.*, too, found that the cytosol was more oxidative under hypoxic conditions.[190]

Previous and current work within the group have shown that our nanosensors are non-toxic and measure IRP in a reversible and non-invasive manner in a variety of cell lines.[23], [191] The nanosensors are biocompatible and possess tuneable plasmon resonance. They do not induce any toxic effects or effect cell viability.[192] The aim of this chapter is to extend the group's previous work by measuring the redox potential of MCF7 cells under perturbed oxygen concentrations as well as normal physiological conditions.

6.2/ Results

6.2.1 Functionalisation of NS

Our spherical nanoshells (NS) of diameter 150 nm (125 nm silica core and 25 nm gold outer shell) were functionalised with a redox-active sensor which contain a quinone moiety which undergoes a reversible $2e^-$, $2H^+$ redox reaction, resulting in a change in molecular structure. Redox-sensitive peaks report on the oxidation state through a change in peak intensity. Our nanosensors can report on redox potentials spanning from hypoxic to oxidative stress conditions. For these studies I used Bis-(2-Anthraquinone carboxamide) (AQ) as this particular reporter molecule has a midpoint potential ($E_{1/2}$ = -327 mV vs NHE) in the hypoxic range. To confirm functionalization, UV-Vis and SERS analysis were performed. Figure 6.1 shows an example of UV-Vis spectra taken from bare NS and functionalised AQ-NS before and after washing. The amount of AQ-NS put into the cells was adjusted depending on the absorbance decrease after washing. A red-shift in wavelength suggested successful functionalisation (due to the higher refractive index of adsorbed AQ compared to water) but this was confirmed through SERS measurements. Figure 6.2 shows the signals at 1669 cm^{-1} and 1606 cm^{-1} which correspond to the quinone C=O stretch and amide stretch/symmetric ring breathing (not redox-sensitive), respectively (previously determined through DFT calculations).[193]

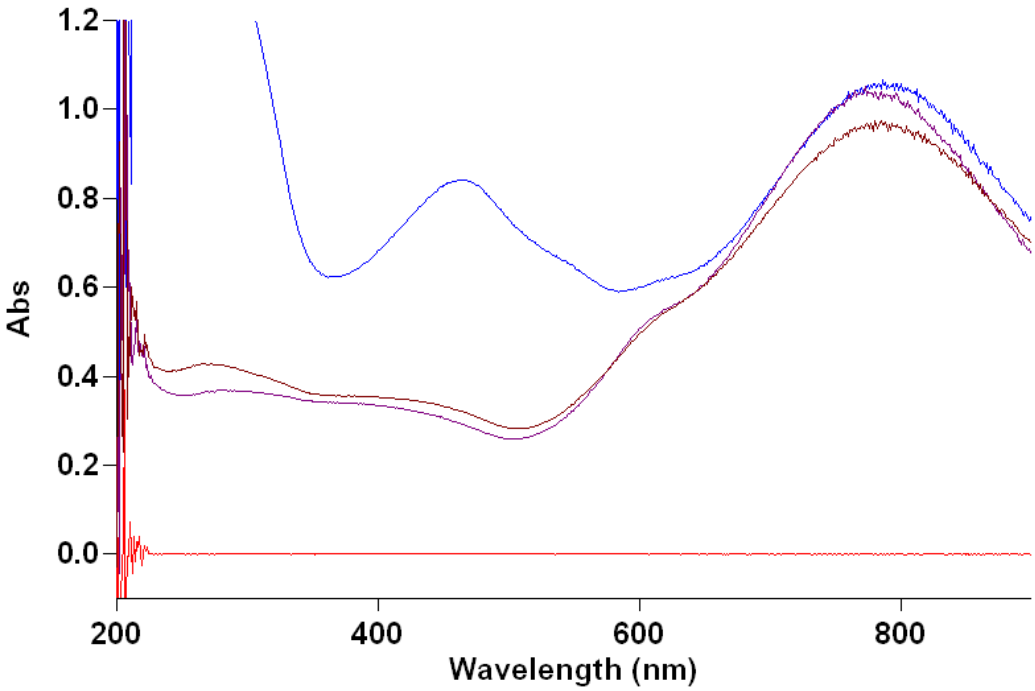

Figure 6.1. UV-Vis spectrum of water blank (red) bare NS (blue), functionalised AQ-NS before washing (purple), functionalised AQ-NS after washing (brown). The wavelength of functionalised NS had red-shifted to 789 nm from 771 nm for bare NS.

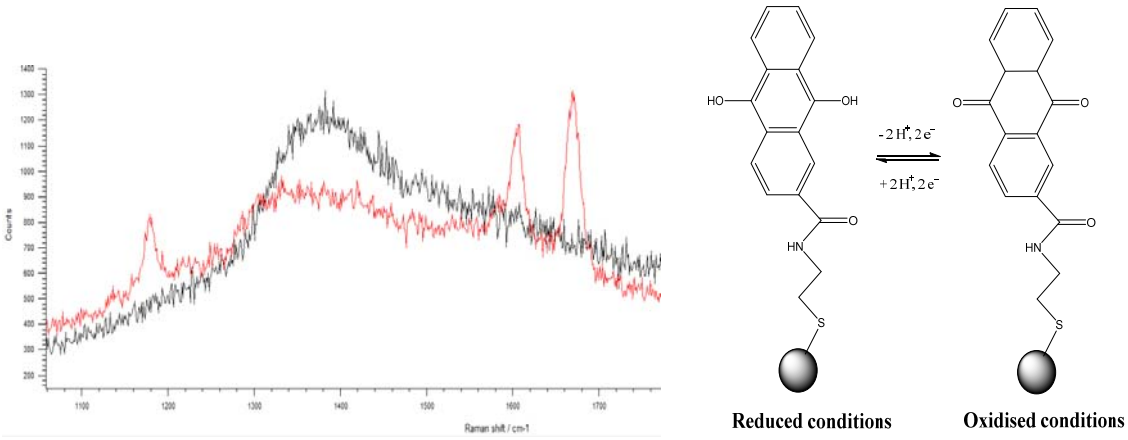

Figure 6.2.(a) SERS spectrum of dry AQ-NS (red) on MgCl2 window (black) and (b) AQ conjugated to a gold nanoshell at equilibrium (not to scale).

SERS maps were acquired, as detailed in Section 2.2, using a Renishaw inVia Raman system with 10% laser power and 1 s point acquisition times as this produced sufficiently high signal-to-noise ratio (Figure 6.3). Higher laser power and shorter acquisition times can resolve peaks, however the higher laser power may burn the cell samples.

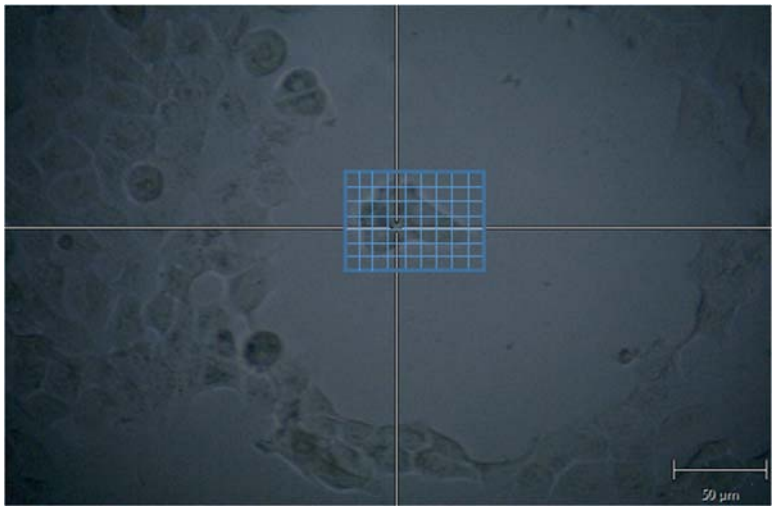

Figure 6.3. A map is manually drawn around the cell using 1 step point acquisitions.

Cellular pH would affect the overall intracellular redox potential as the latter is pH-dependent; therefore, cells were incubated with NS functionalised with the pH-sensitive reporter *para*-mercaptobenzoic acid (MBA) which has been used in previous studies.[52], [194]–[197] The structure and SERS spectrum of dry MBA-NS is shown in Figure 6.4.

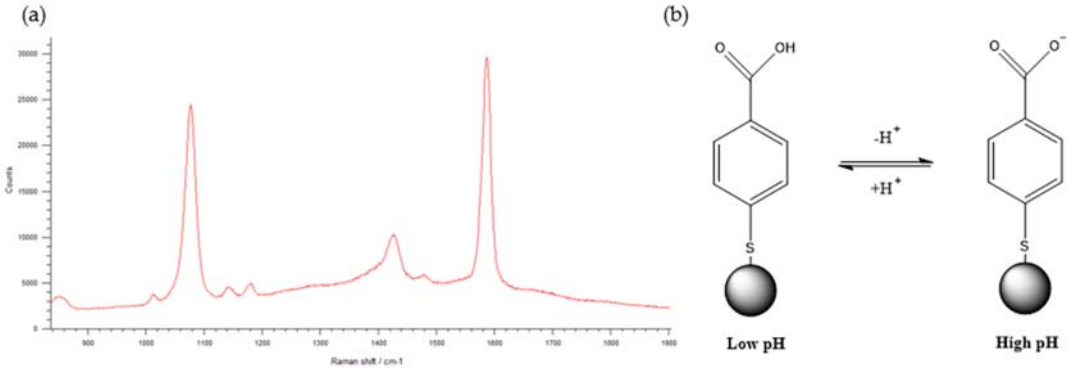

Figure 6.4. (a) SERS spectrum of dry MBA-NS on $MgCl_2$ window and (b) MBA conjugated to a gold nanoshell at equilibrium (not to scale).

6.2.2 SERS measurements

A challenge associated with measuring the IRP and pH of live cells was to keep them in media at fixed pO_2. Several "homemade" and commercially available imaging chambers were tested but all introduced air bubbles into the media. The final homemade device is depicted in Figure 6.5. First of all, two aluminium plates were made with one containing a square window in the middle for viewing the cells. These plates are the top and bottom of the device and contain holes in each corner for clamping the remaining parts together. Next, a plastic mould was designed and created using Autodesk Inventor software and a 3D printer. The mould contained a rectangular gap (for the silica to set into shape) and a cylindrical hole through the centre. Plastic tubing was passed through the holes before pouring silica into the mould and allowing to set overnight. Once solidified, the tubing was removed and the silica was cut out and placed on the bottom aluminium plate. A $MgCl_2$ imaging dish with cells seeded on one side was placed on top with the cell side facing the silica. The aluminium plate with the window was carefully placed on top and screwed into the bottom aluminium plate. Plastic tubing was inserted at both ends through the silica and conditioned media was injected into one end. Once all air bubbles were removed through the other side, the tubing was sealed.

Detailed experimental is described in Chapter 2 but, briefly, cells were seeded at a density of ~75,000 cells into one well of a 6-well plate containing a $MgCl_2$ imaging dish. Fresh media and PBS were added to other wells so that they would be conditioned at the same pO_2 as the cells. The next day, the media from the cells was removed and replaced with FCS-free media with NS. This media was removed the following day and the $MgCl_2$ imaging dish was, first, washed with the conditioned PBS before placing the imagining dish into the device. The conditioned media was then injected.

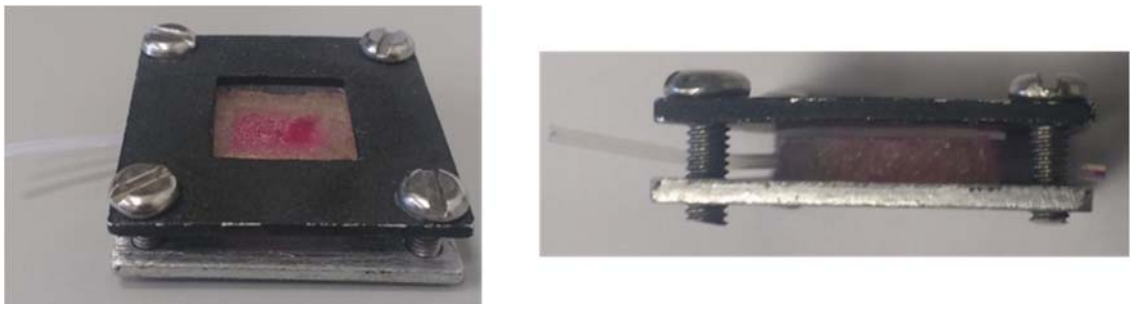

Figure 6.5. Ariel and side view of imaging chamber.

Autofluorescence from organic molecules is low at longer wavelengths[211], and nanoshells have been designed to be used at near-IR wavelengths. Therefore, SERS measurements, in this work, were taken using a 785 nm laser excitation source. Representative spectra of MCF7 cells containing pH- or redox-sensitive sensors are shown in Figure 6.6 and Figure 6.7.

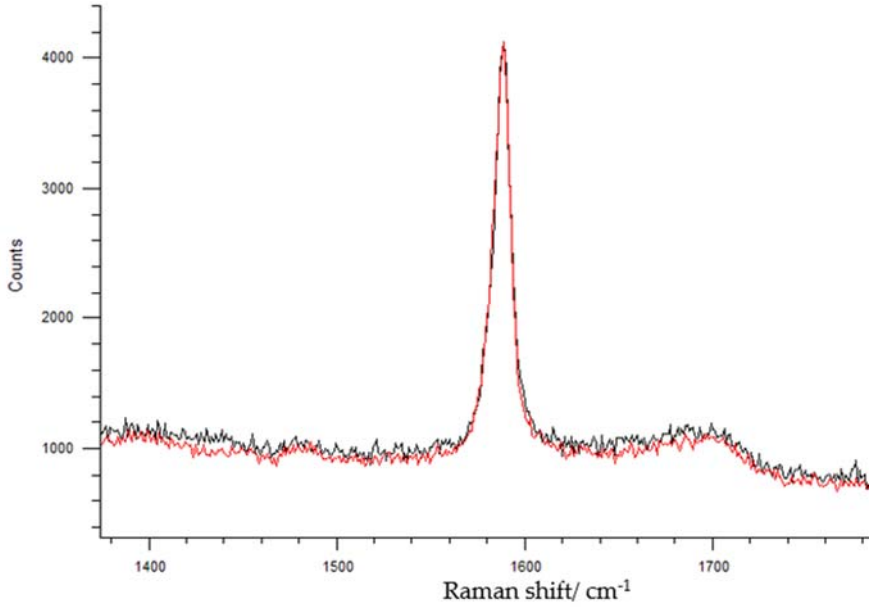

Figure 6.6. Representative Raman spectra of MCF7 cells incubated with MBA-NS at 1% (black) and 21% pO2 (red). All spectra are normalised to the reference peak at ~1590 cm-1 which is due to ring breathing. The peak at ~1400 cm-1 increases with increasing pH and is due to COO^- stretching. A slight increase in the peak at 1700 cm^{-1} with decreasing pH is due to C=O stretching.

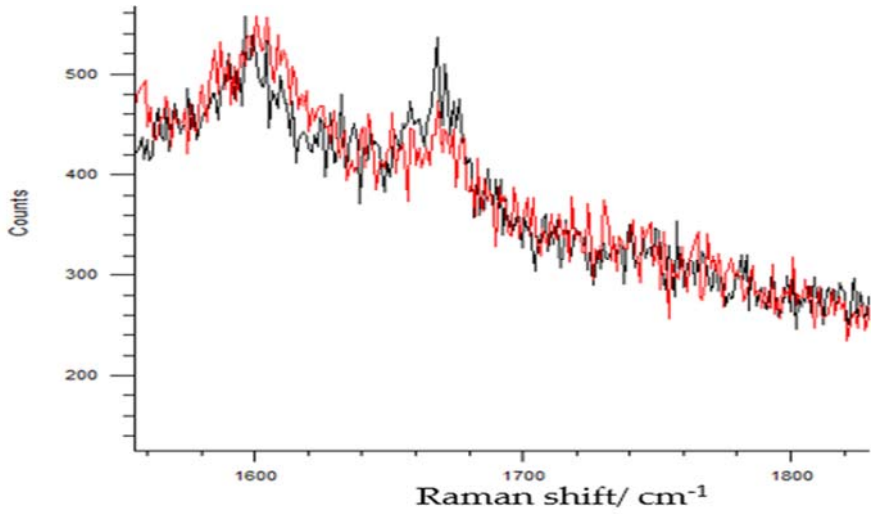

Figure 6.7. Representative SERS spectra of cells incubated at 1% (red) and 21% (black) pO_2 with AQNS.

6.2.3 Processing of data

Many spectra are generated from one map of a cell, thus making data processing to determine IRP extremely time-consuming. Manual baseline correction and smoothing has inherent bias and variability and depends entirely on the individual. Systematic differences would inevitably occur in calculating peak height ratios, leading to differences in the average redox potential. A method for automating the data analysis has been developed by Kate Fisher, a previous member of the CJC group, to help alleviate the drawbacks of manual processing. The SERS files were inserted into Matlab for processing using in-house scripts,[62] as described below.

6.2.3.1 Processing of AQ-NS data

For each spectrum, a background was first subtracted and a Lorentzian peak shape function was applied to fit to the region 1592–1620 cm^{-1} (before and after processing is shown in Figure 6.9). The Lorentzian peak function is in the form below:

$$I(2\theta) = \frac{\omega^2}{\omega^2+(2\theta - 2\theta_0)^2} \qquad \textit{equation 6.1}$$

whereby: w = equal to half of the peak width. The Lorentzian function emphasises peak tails compared to the Gaussian function. Only spectra that produced an adjusted R^2 value of >0.6 were selected for further processing. Spectra with a reference peak height at 1600 cm^{-1} of <100 counts were discarded. The ratio of the peak heights at 1600 cm^{-1} and 1668 cm^{-1} was measured. The redox potential from this ratio and the calibration curve, previously obtained by Lauren Jamieson [195], was calculated along with the associated error. The overall average IRP value and associated standard deviation for cell replicates under each pO_2 condition are quoted in

Table 6. Full details of measurements for each of the 3 replicates of different whole cells under each pO_2 can be found in Appendix A.

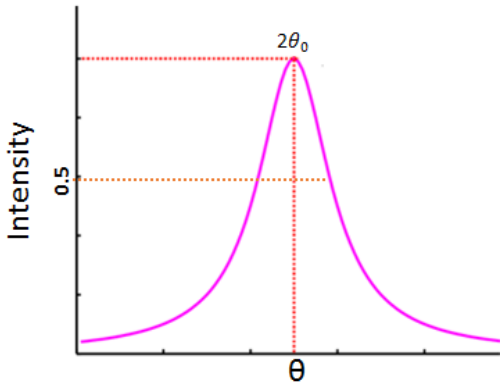

Figure 6.8. Lorentzian peak shape function.

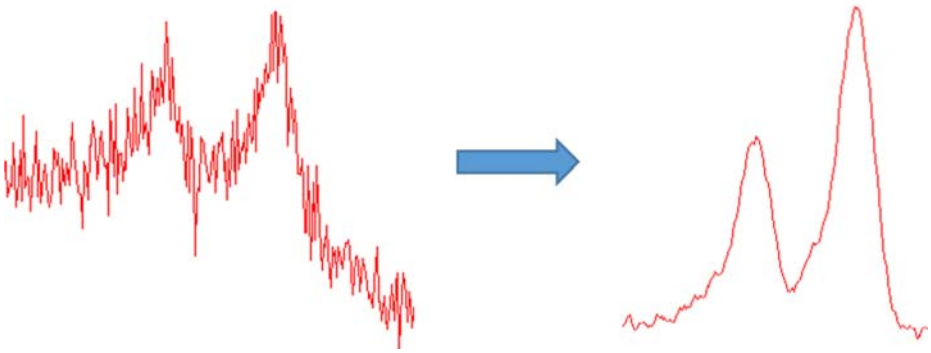

Figure 6.9. AQ-NS signals before and after processing.

6.2.3.2 Processing of MBA-NS data

For each spectrum, a background was first subtracted and a Lorentzian peak shape function was applied on a linear baseline to the reference peak at ~ 1590 cm^{-1}. Only spectra that satisfied the following parameters were selected for further processing: (1) adjusted R^2 value of > 0.8; (2) error in the peak centre of <5 cm^{-1}; (3) peak height of >200 counts. The same was then applied individually to each of the two peaks at ~1400 and ~1700 cm^{-1}. Height ratios and areas of the peaks 1590/1400 cm^{-1}, 1590/1700 $cm^{-1}$and 1400/1700 cm^{-1} were extracted along with the peak centre at ~1590 cm^{-1}. The pH for each parameter was

obtained from the relevant calibration curve, previously obtained by Jing Jiang [191], along with the associated error. Weighted means were calculated for each parameter using inverse weighting to help minimise skewing of results from those with a large error. A colour map of the weighted pH values across the 7 parameters were plotted on a colour map to help visualise cellular pH spatial differences (Figure 6.10). The overall average pH value and associated standard deviation for cell replicates under each pO_2 condition are quoted in

Table 6.

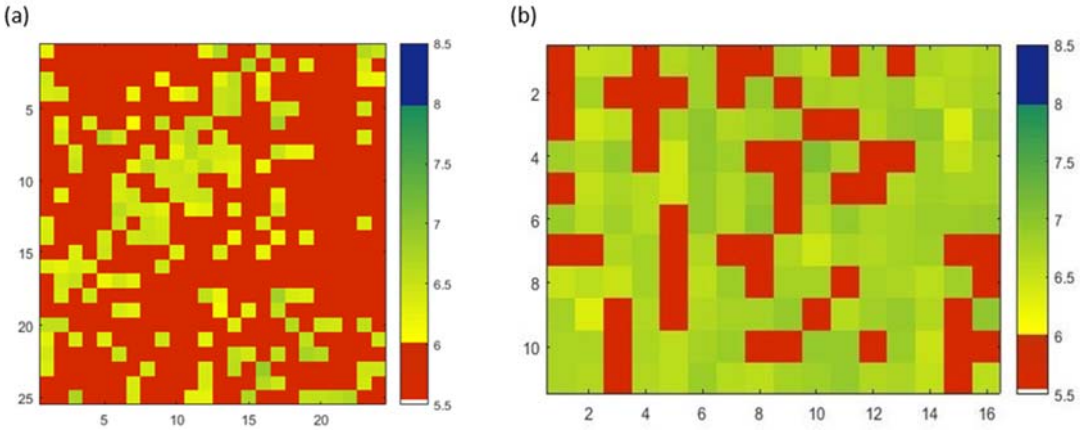

Figure 6.10. Colour map of weighted pH values of MCF7 cell at (a) 2% pO_2 and (b) 21% pO2 obtained from SERS map using MBA-NS.

6.2.4 pH corrected SERS values

The pH and redox potential of at least 3 cells were measured for each pO_2 and then averaged. Detailed results and standard deviations can be found in Appendix A.

Table 6. Average IRPs of MCF7 cells under fixed oxygen conditions. * = *p*-value significance <0.05. *** = *p*-value significance <0.0001.

Cell condition/ % pO_2	IRP/ mV	pH
1	-314.75*	**6.30**
2	-333.73***	**6.06**
3	-305.63	**6.69**
4	-306.88	**6.55**
21	-290.91	**6.45**

The calibration of AQ-NS was done previously by Jing Jiang in buffered solutions at pH 7.0. The Nernst equation is dependent on pH and our group have demonstrated that the half-cell potential of AQ-NS relative to pH changed by 59.1 mV per pH unit.[191] One way ANOVA and Dunnett's multiple comparison's test were conducted to measure the significance of the IRP and pH variation compared to cells at 21% pO_2 (Appendix B). The tests revealed no significance in the pH, therefore it was deemed unnecessary to correct the IRP measurements for pH to avoid introducing a further source of variability. One way ANOVA analysis of IPR results produced a p-value of 0.0009 compared to those obtained at 21% pO_2, implicating a strong significance.

6.2.5 ROS quantification

The level of ROS produced in the cells was measured for reasons including: to help explain the IRP changes and to discriminate between processes driven by IRP changes and those driven by ROS production (Figure 6.11). A fluorinated derivative of fluorescein (H_2DFFDA) was added and a fluorimeter was used to measure the intensity of fluorescence as the molecular probe becomes oxidised by intracellular

ROS. H_2DFFDA in the reduced form is non-fluorescent but, when the acetate groups are removed by intracellular esterases and then oxidised by ROS, the molecular probe fluoresces in the green wavelength (~525 nm).

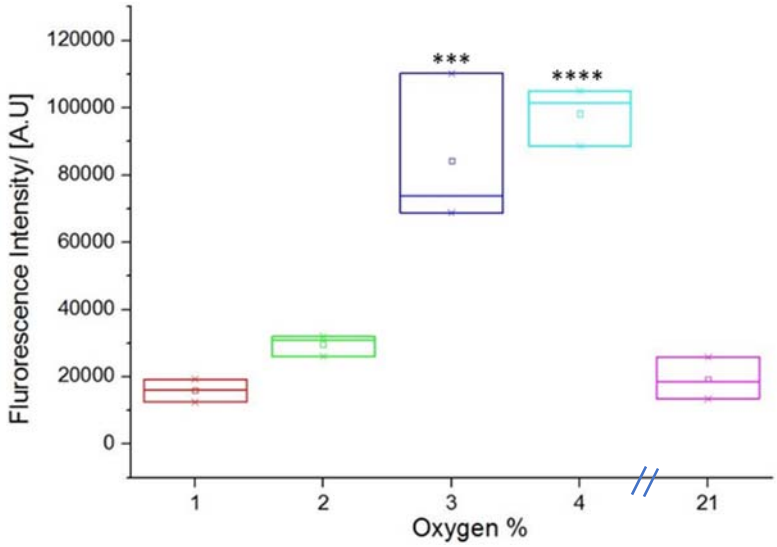

Figure 6.11. Box plot of ROS measurements at varying pO2 for MCF7 cells. *** = p-value significance <0.0001. **** = p-value significance <0.00001.

6.3/ Discussion

The trend in measured IRP is a decrease from 21-2% pO_2 followed by an increase from 2-1% pO_2. The trend in ROS levels, however, is a sharp increase from 21-4% pO_2 and a sharp decrease from 3-1% pO_2 to similar levels as 21% pO_2. These results are different and demonstrate that ROS and redox potential are concepts that cannot be used interchangeably. As mentioned in Chapter 5, PTEN catalytic activity can be inhibited through oxidation of ROS. Despite the redox status of the cell, signalling pathway cascades regulated by phosphorylation of target proteins can be prevented through overoxidation of the catalytic active site. Thus, redox switches can be irreversibly destroyed. This may explain why the transcriptomic profile of miR-29 (a regulator of PTEN) is similar to that of the ROS profile and not the IRP profile. The change in IRP profile from 21-2% pO_2 may be physiological but, at lower pO_2, a stimulus to stress

may be occurring which is aided by the level of ROS to initiate the appropriate response.

There is yet no comprehensive study, to my knowledge, on the redox status of various cancer cell types and by how much it contributes to the cancer phenotype. ROS have dual functions: at low levels, they activate various signalling pathways but at high levels can irreversibly damage cellular compartments and cause cell death. ROS can also mediate chemo/radiotherapy invasiveness and reprogram metabolism.[198]

In this work, an imaging device was created to maintain live MCF7 cells in media under fixed pO_2 whilst taking detailed SERS maps. At least 3 measurements were taken and averaged for each oxygen condition. Any variation in IRP and pH of cells cultured under the same conditions could be due to different stages of cell life-cycle.

Interestingly, the pH and SERS results of the cells do not correlate well with the level of lactic acid produced shown in the NMR data in Chapter 3. For example, NMR suggests that the highest concentration of lactic acid produced is from cells cultured at 3% pO_2 but the cells are most acidic at 2% pO_2. A reductive redox potential at 2% pO_2 would suggest higher rates of glycolysis and PPP which produce reducing agents. The less reductive potential at 1% pO_2 could possibly be explained by cells adapting to extreme hypoxic stress and controlling redox homeostasis. Further work could be conducted in assessing the rates of glycolysis and OXPHOS as glycolysis may in fact be reduced under severe hypoxia (<2% pO_2) to control the levels of reducing agents produced. Studies have shown that hypoxia-induced ROS signals from mitochondria trigger the activation of HIF-1α by inhibiting PHDs.[199] Furthermore, measuring the expression of antioxidant systems, such as Nrf2, could also give an indication as to whether the decrease in ROS is actually due to upregulation of scavenging species.

ROS measurements may strengthen the hypothesis that glycolysis could be increasing at 2% pO_2. At 3% pO_2, ROS concentration is at its highest but suddenly dips at lower oxygen concentrations, implicating that the cancer cells are switching metabolic pathways to prevent damage caused by ROS.

6.4/ Conclusion

Intracellular redox potential is becoming increasingly recognised as an integral component in the decision making concerning cellular signalling and cell fate. Understanding how subtle changes in redox potential and its subsequent shift in biochemical behaviour is important as disruption of redox homeostasis leads to aberrant cell signalling and has implications in disease. SERS is rapidly growing as a technique to be used in diagnosis of disease *in vivo*. In this work, SERS was used to measure the IRP of MCF7 cells which was found to be most reduced in cells under 2% pO_2. Low ROS levels were also found at 2% pO_2, coinciding with potentially reduced OXPHOS and increased glycolysis.

Chapter 7: Conclusion

Cancer is one of the leading causes of mortality worldwide, with half of the U.K. population now predicted to contract some form of cancer during their lifetime. The complete etiology and pathogenesis of cancer still remains unclear but development has been made in trying to elucidate perturbations or abnormalities in metabolism and signal transduction that result in cell malignancy. Metabolic dysregulation is one of the hallmarks of cancer along with sustained proliferation and cell death resistance. It is paramount to understand metabolic dysregulation in cancer cells so that novel biomarkers can be discovered to develop new efficacious therapeutic drugs. The aims of this work were to:

1) Use analytical techniques in conjunction with surprisal analysis to analyse differences in the metabolic and transcriptomic profiles of cells under normal physiological and perturbed conditions.

2) Use nanosensors to map redox potential distributions in living cells to correlate the effect of redox signalling on cell phenotype under normal physiological and perturbed conditions.

From the independently conducted NMR, SERS and RNA-seq experiments of MCF7 cells, it can be seen that a change in phenotype is occurring between 4% and 2% pO_2 and between 2% and 1% pO_2 (Figure 7.1). It has become increasingly recognised that ROS play a critical role in regulating various physiological signalling pathways. It is perhaps that MCF7 cells are responding to stress and maintaining homeostasis by improving the balance between ROS production and ROS scavenging systems, hence the change in trend from 2% - 1% pO_2 in all experiments. Alteration in redox signalling can be caused by excessive accumulation of ROS; for example, redox-sensitive proteins are subject to oxidation which results in signalling cascade events and a change in phenotype. Cysteine thiol redox status can be altered either directly or via

a redox relay system. Transcription factors (TFs), in particular, play a role in subsequent biological outcomes.

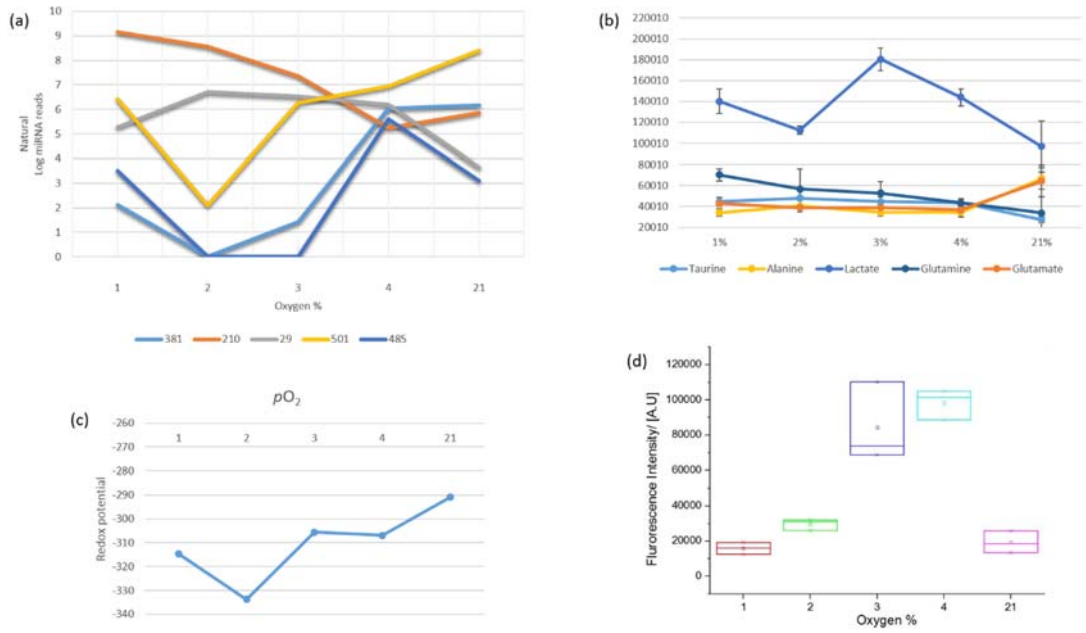

Figure 7.1.(a) Transcriptomic, (b) metabolomic and (c) SERS and (d) ROS profiles of MCF7 cells at varying pO_2.

TFs are proteins that control the rate of protein synthesis by switching genes on or off. There are two types of TF – activators and repressors – which bind to the promoter region upstream of the transcription start site of a gene where RNA polymerase is recruited and bound to. Repressors, however, prevent the polymerase enzyme from binding so that the gene is not transcribed. TFs can be controlled by hormones and second messengers, causing their translocation from the cytoplasm and into the nucleus. Accumulating evidence suggests that aberrant regulation of miRs by TFs is associated with the initiation and progression of disease. MiRs are typically negative regulators of mRNA expression and, thus, play key roles in metabolism, cell signalling and apoptosis, for example. Using the database GeneCards, known TFs of the miR of interest in Chapter 5 are noted in Table 7. At least one TF for each miR is redox sensitive.

Table 7. Transcription factor regulators of miRs of interest in MCF7 cells. Those highlighted in red are zinc-finger proteins.

miRNA	Transcription Factor
210	ARNT, AGO1, HIF
675	KLF1
335	CBX, PKNOX1, HDAC1, CTCF
Let-7f	HDGF, PKNOX1
29	PKNOX1, ATF1, HDGF, FOXA2, MYC, ARNT, CTCF
381	FOXA2, ATF1, CTCF, SUZ12, HDGF, GATA3, MNT
2278	Unknown
370	FOXA2, PKNOX1, ZFP3, ZNF680, HDGF, ZKSCAN1
411	Unknown
501	ZNF140, ZNF316, PKNOX1, ZFP64
485	ZNF680, ZNF263, MNT, CTCF, GATA3, SUZ12, ZFP3

Many TFs contain redox-sensitive cysteine residues in the DNA binding site. TFs highlighted in red in Table 7contain zinc-finger structures which require at least two zinc-coordinated cysteine sulfhydryl groups. Zinc finger proteins are the largest class of DNA-binding proteins. The most common zinc-finger structures contain two cysteines and two histidines (e.g. CTCF [200]) or four cysteines coordinated to zinc (e.g. GATA3 [201]). Oxidation or electrophilic attack of the cysteine thiol prevents DNA-binding due to disassembly of the secondary structure and release of the metal ion.

HIF-1 is a TF that exhibits increased stability and transcriptional potency under low pO_2. It consists of the subunits HIF-1α, HIF-1β and the aryl hydrocarbon receptor

nuclear translocator (ARNT), the latter being a TF of miR-210. Under well oxygenated conditions, HIF-1α is bound by the von Hippel-Lindau (VHL) protein, binding of which is dependent upon hydroxylation of a specific proline residue in HIF-1α by the prolyl hydroxylase PHD2. The latter uses oxygen as a substrate, therefore under hypoxic conditions PHD2 is inhibited and HIF-1α is not ubiquitinated and degraded.[178], [202] HIF-1α activates the transcription of genes that play critical roles in cancer biology, such as epithelial-mesenchymal transition [203] and glucose metabolism.[204]

HIF-1α also activates for the c-MYC transcriptional regulator Max network transcriptional repressor (MNT). MNT encodes a protein member of the MYC/Max/Mad network and is a TF of miR-381 and miR-485. MYC binding with MYC-associated protein X (MAX) allows for former's binding to the promoter region of its target genes, such as those that upregulate glutamine-metabolising enzymes. MAX is controlled through binding with MAX dimerization protein (MAD). This dimer prevents MYC: MAX from transactivating its target genes. HIF-1α upregulates MAD and can directly bind to MAX, therefore reducing MYC:MAX activity.[205] This may explain why miR-381 and miR-485 reads are reduced under low pO_2.

Human hepatoma-derived growth factor (HDGF) regulates the transcription of miR-let-7f, miR-29 and miR-370. The homology of HDGF is similar to high mobility group protein 1 (HMGB1) [206] which has been postulated as a redox sensor. The redox function of HMGB1 depends on two cysteine residues (Figure 7.2).[207] HMGB1 is a regulator of apoptosis and, depending on it oxidation state, has varied cytokine activity: if completely oxidised, it has no cytokine and chemokine activity.[208], [209]

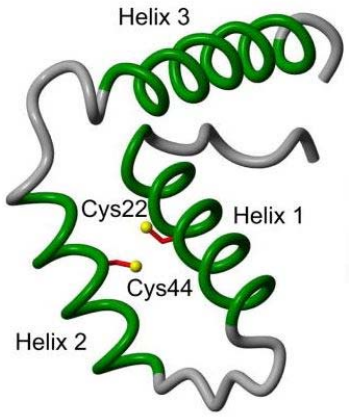

Figure 7.2. Crystal structure of HMGB1 nuclear localisation sequence with redox-active cysteine residues.[207]

In order to avoid excessive ROS production, cancer cells switch the utilisation of mitochondrial respiration to fermentation and develop strategies to enhance ROS detoxification. As seen from Figure 7.1d, ROS generation is at its highest at 3% pO_2 and at its lowest at 1% pO_2. It is possible that the cells are utilising glycolysis and the PPP more at 2% pO_2.

Altered energy metabolism has proven to be as widespread in cancer cells as many of the other cancer-associated traits currently accepted as hallmarks of cancer. This work has correlated the impact of intracellular redox potential to changes in the transcriptome and the downstream metabolome of cancer cell lines under perturbed pO_2. I have demonstrated that ROS and redox potential are concepts that cannot be used interchangeably; ROS are possible driving forces for a change in phenotype due to irreversible activation of signalling pathways in response to stress.

Project limitations

Despite numerous advances, the sheer complexity of biological mixtures far outweighs the current capabilities of NMR. Metabolite identification, of low concentrated species in particular, pose a major challenge for metabolomic studies due to limited instrumental sensitivity and peak overlap. These challenges restrict the number and accurate quantification of metabolites in a sample that contains far more

undetected species. Some important pathways may be overlooked, resulting in a misrepresentation of systems biology.

Although FT-ICR-MS is recognised for its profound sensitivity and ultra-high resolution, sample analysis is hampered by the lack of well-established and standardised methods. Due to the lack of available internal standards and ion suppression, calibration and positive identification of untargeted acquired data is extremely difficult. Furthermore, one parent ion mass can represent many isomers and, depending on positive or negative acquisition mode, cationised or anionised adducts. Combining MS with a separating technique such as liquid or gas chromatography would be beneficial but even then not every metabolite will be detected. GC/LC-MS may add a further dimension to the data, only intensifying the challenge of metabolite identification.

This work involved the extraction of metabolites and miR from a monolayer of various cell lines which does not mimic the complexity and heterogeneity of clinical tumours. Proliferation is unrestrained in conventional 2D cell culture and the cells do not mirror the architecture of living tissue. Gradients also exist within tumours: a necrotic core surrounded by a middle quiescent layer, with limited oxygen and nutrients, and an external proliferating zone. A 3D model using multicellular tumour spheroids is regarded as a more stringent and representative model representing the avascular region of tumours that is dependent on diffusion. Effort was made here to gently trypsinise layers of cells from MCF7 spheroids. This proved difficult, however, for the following reasons: (1) many spheroids were needed to enable the detection of each layer of cells by NMR; (2) trypsinisation involved additional washing steps instead of instantly fixing the cells before extraction; (4) sample reproducibility would be difficult as it meant growing spheroids to equal sizes and removing the same thickness of layer at each pO_2 condition. It would have been ideal to have measured IRP of spheroids instead of monolayer, particularly now that recent studies have suggest a symbiosis of cells excreting lactate and neighbouring cells taking up the lactate to convert to glucose.

Overall, in this work I successfully measured the IRP of MCF7 cells using a homemade imaging device which kept the cells at constant pO_2. This allowed for more accurate cross-comparison with results obtained from the same cell line's metabolome and transcriptome, also measured at varying pO_2. The data revealed a clear link between intracellular oxygen perturbation and biochemical activity, possibly due to the level of thiol oxidation of critical cysteines within redox-sensitive proteins. More research on the relationship between varying IRP and the cellular antioxidant response could improve our understanding of the cell's innate response to hypoxic stress and its link with chemotherapeutic efficiency.

Appendix A

CHAPTER 3

Table 8. ^{1}H NMR chemical shifts of assigned aqueous phase metabolites from A549, PC3 and MCF7 cells. (s) = singlet, (d) = doublet, (dd) = doublet of doublets, (t) = triplet, (m) = multiplet, (q) = quartet.

Metabolites	**Chemical shift**
AMP/ADP/ATP	8.55 (s), 8.27 (s), 6.15 (d), 4.67 (t), 4.29 (m)
Acetate	1.92 (s)
Alanine	1.48 (d)
Formate	8.46 (s)
Fumarate	6.51 (s)
Glucose	4.23 (dd), 4.65 (d), 3.90 (dd), 3.84 (m), 3.73 (m), 3.54 (dd), 3.47 (m), 3.41 (m), 3.26 (dd)
Glutamate	3.75 (dd), 2.33 (m), 2.11 (m), 2.02 (m)
Glutamine	3.76 (t), 2.46 (m), 2.41 (m), 2.13 (m)
Glycine	3.56 (s)
GPC	4.32 (m), 3.87 (m), 3.66 (m), 3.60 (m), 3.21 (s)
Histidine	7.84 (s), 7.08 (s), 3.99 (dd)
Isoleucine	1.97 (m), 1.46 (m), 1.26 (m), 1.01 (d), 0.94 (t)
Lactate	4.12 (q), 1.33 (d)
Leucine	1.73 (m), 0.96 (t)
Lysine	3.02 (t)
NAD^{+}	9.34 (s), 9.15 (d), 8.84 (d), 8.43 (s), 8.18 (s), 8.16 (s), 6.09 (d), 6.03 (d)
Phenylalanine	7.33 (d), 7.38 (m), 7.43 (m)
Phosphocholine	4.17 (m), 3.58 (t), 3.22 (s)
Pyruvate	2.38 (s)

Succinate	2.40 (s)
Taurine	3.43 (t), 3.26 (t)
Tyrosine	7.19 (d), 6.90 (d)
UMP/UDP/UTP	7.99 (d), 5.96 (d)
UDP-glc	7.95 (d), 5.98 (d), 5.61 (dd)
Valine	3.62 (d), 2.26 (m), 1.05 (d), 1.02 (d)

CHAPTER 4

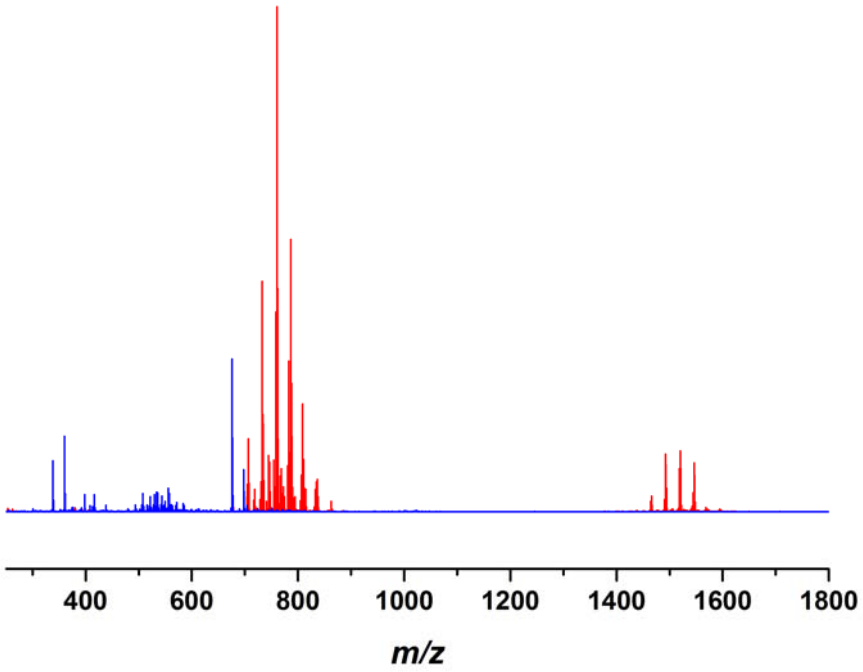

Figure A1. MS of (red) MCF7 cell organic phase extracts and a (blue) control sample with no cells.

CHAPTER 6

Table 9. pH measurements of MCF7 cells.

pO_2 of cell, %	Average pH of cell	Average pH error of each cell	Average pH of all replicates	STDEV of pH of all replicates
1	6.3	0.1	**6.30**	**±0.12**
	6.4	0.1		

	6.1	0.1		
2	6.1	0.0	**6.1**	**±0.03**
	6.1	0.1		
	6.0	0.0		
3	6.4	0.1	**6.7**	**±0.24**
	6.9	0.1		
	6.8	0.1		
4	6.2	0.2	**6.6**	**±0.24**
	6.7	0.2		
	6.8	0.3		
21	6.5	0.2	**6.5**	**±0.05**
	6.5	0.3		
	6.4	0.1		

Table 10. SERS measurements of MCF7 cells.

***p*O₂ of cell, %**	**Average IRP of cell**	**Average IRP error of each cell**	**Average IRP of all replicates**	**STDEV of IRP of all replicates**
1	-316.1	10.4	**-314.7**	**±11.25**
	-310.3	14.5		
	-317.8	8.8		
2	-346.3	24.3	**-333.7**	**±22.18**
	-324.5	17.3		
	-330.4	24.9		
3	-301.7	10.1	**-305.6**	**±10.51**
	-305.5	8.6		
	-309.7	12.9		

4	-319.6	12.9	**-306.9**	**±11.21**
	-298.7	6.3		
	-302.4	14.4		
21	-297.9	2.6	**-290.9**	**±4.82**
	-287.6	6.2		
	-287.3	5.6		

Appendix B

All statistical analysis was conducted using one way ANOVA, comparing all sample means with the control mean at 21% pO_2. Dunnett's multiple comparisons test (DMCT) was then used to compare each sample mean with the mean at 21% pO_2.

CHAPTER 3

Table 11. *p*-values for NMR metabolites of interest for MCF7 cells.

Metabolite	One way ANOVA p-value	Significance	DMCT p-value	Significance
Taurine	<0.0001	****	0.0001	****
			0.0001	****
			0.0001	****
			0.0001	****
Alanine	<0.0001	****	0.0001	****
			0.0001	****
			0.0001	****
			0.0001	****
Fumarate	0.001	**	0.0406	*
			0.112	ns
			0.0017	**
			0.0004	***
NADH	0.0645	ns	0.2881	ns
			0.5614	ns
			0.1019	ns
			0.021	*
Lactate	<0.0001	****	0.0001	***
			0.2322	ns
			0.0001	****

			0.0001	****
Glucose	0.3120	ns	0.9443	ns
			0.75	ns
			0.6109	ns
			0.1286	ns
Glutamine	<0.0001	****	0.0004	***
			0.0001	****
			0.0001	****
			0.0001	****
Glutamate	<0.0001	****	0.0004	***
			0.0001	****
			0.0001	****
			0.0001	****

Table 12. *p*-values for NMR metabolites of interest of A549 cells.

Metabolite	**One way ANOVA p-value**	**Significance**	**DMCT p-value**	**Significance**
Glucose	<0.0001	****	0.0001	****
			0.0001	****
			0.0001	****
			0.0001	****
AMP/ADP/ATP	0.0005	***	0.0075	**
			0.9807	ns
			0.0095	**
			0.9618	ns
UDP-glc	<0.0001	****	0.0001	****
			0.0001	****
			0.0001	****

			0.0001	****
UMP/UDP/UTP	<0.0001	****	0.0001	****
			0.0001	****
			0.0001	****
			0.0001	****
NADH	<0.0001	****	0.0001	****
			0.0001	****
			0.0001	****
			0.0001	****

CHAPTER 5

Table 13. *p*-values for miRs of interest of MCF7 cells.

miRNA	**One way ANOVA p-value**	**Significance**	**DMCT p-value**	**Significance**
381	0.0362	*	0.2214	ns
			0.0328	*
			0.0411	*
			0.9550	ns
210	<0.0001	****	0.0001	***
			0.0045	**
			0.6624	ns
			0.9990	ns
29	0.0026	**	0.9885	ns
			0.0024	***
			0.0120	*
			0.0887	ns
501	<0.0001	****	0.0001	****
			0.0001	****

			0.0001	****
			0.0003	**
485	0.0349	*	0.9633	ns
			0.9228	**
			0.9228	*
			0.059	ns
675	0.0043	**	0.0653	ns
			0.4296	ns
			0.9999	ns
			0.0929	ns
335	0.3727	ns	0.9621	ns
			0.2527	ns
			0.9228	ns
			0.3944	ns
Let-7f	0.1231	ns	0.1084	ns
			0.2266	ns
			0.7547	ns
			0.9999	ns
2278	0.0001	***	0.0047	**
			0.0001	****
			0.0002	***
			0.0018	**
370	0.0004	***	0.9963	ns
			0.3903	ns
			0.6462	ns
			0.0015	**
411	<0.0001	****	0.7703	ns

			0.5784	ns
			0.8658	ns
			0.0001	****

CHAPTER 6

Table 14. *p*-values for IRP of MCF7 cells.

pO_2	One way ANOVA	Significance	DMCT against 21% pO_2 mean	Significance
1%	0.0009	***	0.0143	*
2%			0.0002	***
3%			0.1384	ns
4%			0.1019	ns
21%			-	-

Table 15. *p*-values for pH of MCF7 cells.

pO_2	One way ANOVA	Significance	DMCT against 21% pO_2 mean	Significance
1%	0.0281	***	0.4379	ns
2%			0.1182	ns
3%			0.4065	ns
4%			0.7882	ns
21%			-	-

Table 16. *p*-values for ROS produced by MCF7 cells.

pO_2	One way ANOVA	Significance	DMCT against 21% pO_2 mean	Significance
1%	<0.0001	****	0.9877	ns
2%			0.6476	ns
3%			0.0002	***
4%			0.0001	****
21%			-	-

References

[1] J. K. Nicholson, J. C. Lindon, and E. Holmes, "'Metabonomics': understanding the metabolic responses of living systems to pathophysiological stimuli via multivariate statistical analysis of biological NMR spectroscopic data," *Xenobiotica*, vol. 29, no. 11, pp. 1181–1189, 1999.

[2] M. Čuperlović-Culf, D. A. Barnett, A. S. Culf, and I. Chute, "Cell culture metabolomics: Applications and future directions," *Drug Discov. Today*, vol. 15, no. 15–16, pp. 610–621, 2010.

[3] M. Cuperlovic-Culf, I. C. Chute, A. S. Culf, M. Touaibia, A. Ghosh, S. Griffiths, D. Tulpan, S. Léger, A. Belkaid, M. E. Surette, and R. J. Ouellette, "1H NMR metabolomics combined with gene expression analysis for the determination of major metabolic differences between subtypes of breast cell lines," *Chem. Sci.*, vol. 2, no. 11, p. 2263, 2011.

[4] M. L. Dória, C. Z. Cotrim, C. Simões, B. Macedo, P. Domingues, M. R. Domingues, and L. A. Helguero, "Lipidomic analysis of phospholipids from human mammary epithelial and breast cancer cell lines," *J. Cell. Physiol.*, vol. 228, no. 2, pp. 457–468, 2013.

[5] K. L. Colson, "Cryogenically cooled NMR Probes: a Revolution for NMR Spectroscopy," *Mod. NMR Approaches To Struct. Elucidation Nat. Prod. Instrum. Softw.*, vol. 1, pp. 58–70, 2016.

[6] O. Feron, "Pyruvate into lactate and back: From the Warburg effect to symbiotic energy fuel exchange in cancer cells," *Radiother. Oncol.*, vol. 92, no. 3, pp. 329–333, 2009.

[7] R. Bartrons and J. Caro, "Hypoxia, glucose metabolism and the Warburg's effect," *J. Bioenerg. Biomembr.*, vol. 39, no. 3, pp. 223–229, 2007.

[8] C. Frezza, L. Zheng, D. A. Tennant, D. B. Papkovsky, B. A. Hedley, G. Kalna, D. G. Watson, and E. Gottlieb, "Metabolic profiling of hypoxic cells revealed a catabolic signature required for cell survival," *PLoS One*, vol. 6, no. 9, 2011.

[9] H. Bando, M. Toi, K. Kitada, and M. Koike, "Genes commonly upregulated by hypoxia in human breast cancer cells MCF-7 and MDA-MB-231," *Biomed. Pharmacother.*, vol. 57, no. 8, pp. 333–340, 2003.

[10] S. Wei, L. Liu, J. Zhang, J. Bowers, G. A. N. Gowda, H. Seeger, T. Fehm, H. J. Neubauer, U. Vogel, S. E. Clare, D. Raftery, and D. Raftery, "Metabolomics approach for predicting response to neoadjuvant chemotherapy for breast cancer," vol. 7, no. 2, pp. 9–7, 2012.

[11] M. Bayet-Robert, D. Loiseau, P. Rio, A. Demidem, C. Barthomeuf, G. Stepien, and D. Morvan, "Quantitative two-dimensional HRMAS 1H-NMR spectroscopy-based metabolite profiling of human cancer cell lines and response to chemotherapy," *Magn. Reson. Med.*, vol. 63, no. 5, pp. 1172–1183, 2010.

[12] L. Mörén, C. Wibom, P. Bergström, M. Johansson, H. Antti, and A. T. Bergenheim, "Characterization of the serum metabolome following radiation treatment in patients with high-grade gliomas," *Radiat. Oncol.*, vol. 11, no. 1,

pp. 1–9, 2016.
[13] Y. Liu, K. Smirnov, M. Lucio, R. D. Gougeon, H. Alexandre, and P. Schmitt-Kopplin, "MetICA: Independent component analysis for high-resolution mass-spectrometry based non-targeted metabolomics," *BMC Bioinformatics*, vol. 17, no. 1, pp. 1–14, 2016.
[14] A. Alonso, S. Marsal, and A. JuliÃ , "Analytical Methods in Untargeted Metabolomics: State of the Art in 2015," *Front. Bioeng. Biotechnol.*, vol. 3, no. March, pp. 1–20, 2015.
[15] J. Bartel, J. Krumsiek, and F. J. Theis, "Statistical Methods for the Analysis of High-Throughput Metabolomics Data," *Comput. Struct. Biotechnol. J.*, vol. 4, no. 5, p. e201301009, 2013.
[16] R. Rousseau, B. Govaerts, M. Verleysen, and B. Boulanger, "Comparison of some chemometric tools for metabonomics biomarker identification," *Chemom. Intell. Lab. Syst.*, vol. 91, no. 1, pp. 54–66, 2008.
[17] F. Yao, J. Coquery, and K.-A. D. R. Le Cao, "Independent Principal Component Analysis for biologically meaningful dimension reduction of large biological data sets," *BMC Bioinformatics*, vol. 13, no. 1, p. 24, 2012.
[18] T. Chen, Y. Cao, Y. Zhang, J. Liu, Y. Bao, C. Wang, W. Jia, and A. Zhao, "Random forest in clinical metabolomics for phenotypic discrimination and biomarker selection," *Evidence-based Complement. Altern. Med.*, vol. 2013, 2013.
[19] W. J. Griffiths and Y. Wang, "Mass Spectrometry in Metabolomics," *Mol. Anal. Genome Discov. Second Ed.*, pp. 271–298, 2012.
[20] S. Zadran, F. Remacle, and R. Levine, "Surprisal analysis of glioblastoma multiform (GBM) MicroRNA dynamics unveils tumor specific phenotype," *PLoS One*, vol. 9, no. 9, 2014.
[21] V. Mallikarjun, D. J. Clarke, and C. J. Campbell, "Cellular redox potential and the biomolecular electrochemical series: A systems hypothesis.," *Free Radic. Biol. Med.*, vol. 53, no. 2, pp. 280–288, May 2012.
[22] S. Rose, S. Melnyk, T. A. Trusty, O. Pavliv, L. Seidel, J. Li, T. Nick, and S. J. James, "Intracellular and Extracellular Redox Status and Free Radical Generation in Primary Immune Cells from Children with Autism," *Autism Res. Treat.*, vol. 2012, pp. 1–10, 2012.
[23] C. A. R. Auchinvole, P. Richardson, C. McGuinnes, V. Mallikarjun, K. Donaldson, H. McNab, and C. J. Campbell, "Monitoring intracellular redox potential changes using SERS nanosensors," *ACS Nano*, vol. 6, no. 1, pp. 888–896, 2012.
[24] A. Bar-Even, A. Flamholz, E. Noor, and R. Milo, "Rethinking glycolysis: on the biochemical logic of metabolic pathways," *Nat. Chem. Biol.*, vol. 8, no. 6, pp. 509–517, May 2012.
[25] L. M. Uusitalo and N. Hempel, "Recent advances in intracellular and in vivo ROS sensing: Focus on nanoparticle and nanotube applications," *Int. J. Mol. Sci.*, vol. 13, no. 9, pp. 10660–10679, 2012.
[26] B. C. D. and C. J. Chang, "Chemistry and biology of reactive oxygen species in signaling or stress responses," *Nat Chem Biol*, vol. 7, no. 8, pp. 504–11, 2012.

[27] A. Banach-Latapy, T. He, M. Dardalhon, L. Vernis, R. Chanet, and M. E. Huang, "Redox-sensitive YFP sensors for monitoring dynamic compartment-specific glutathione redox state," *Free Radic. Biol. Med.*, vol. 65, pp. 436–445, 2013.

[28] S. Y. Rhieu, A. A. Urbas, D. W. Bearden, J. P. Marino, K. A. Lippa, and V. Reipa, "Probing the intracellular glutathione redox potential by in-cell NMR spectroscopy," *Angew. Chemie - Int. Ed.*, vol. 53, no. 2, pp. 447–450, 2014.

[29] M. Marí, A. Morales, A. Colell, C. García-Ruiz, and J. C. Fernández-Checa, "Mitochondrial Glutathione, a Key Survival Antioxidant," *Antioxid. Redox Signal.*, vol. 11, no. 11, pp. 2685–2700, 2009.

[30] P. Li, D. Zhang, L. Shen, K. Dong, M. Wu, Z. Ou, and D. Shi, "Redox homeostasis protects mitochondria through accelerating ROS conversion to enhance hypoxia resistance in cancer cells," *Sci. Rep.*, vol. 6, no. February, pp. 1–13, 2016.

[31] S. Chakravarthi, C. E. Jessop, and N. J. Bulleid, "The role of glutathione in disulphide bond formation and endoplasmic-reticulum-generated oxidative stress," *EMBO Rep.*, vol. 7, no. 3, pp. 271–275, 2006.

[32] C. Appenzeller-Herzog, "Glutathione- and non-glutathione-based oxidant control in the endoplasmic reticulum," *J. Cell Sci.*, vol. 124, no. 6, pp. 847–855, 2011.

[33] H. Østergaard, C. Tachibana, and J. R. Winther, "Monitoring disulfide bond formation in the eukaryotic cytosol," *J. Cell Biol.*, vol. 166, no. 3, pp. 337–345, 2004.

[34] J. M. Hansen, H. Zhang, and D. P. Jones, "Differential oxidation of thioredoxin-1, thioredoxin-2, and glutathione by metal ions," *Free Radic. Biol. Med.*, vol. 40, no. 1, pp. 138–145, 2006.

[35] J. M. MatÉs, C. Pérez-Gómez, and I. N. De Castro, "Antioxidant enzymes and human diseases," *Clin. Biochem.*, vol. 32, no. 8, pp. 595–603, 1999.

[36] M. Kirsch and H. D. E. Groot, "NAD (P) H , a directly operating antioxidant ?," *FASEB J.*, vol. 15, no. 9, pp. 1569–1574, 2018.

[37] A. Lau, "Dual roles of Nrf2 in cancer," *Aerospace*, vol. 58, pp. 262–270, 2009.

[38] E. S. J. Arnér and A. Holmgren, "Physiological functions of thioredoxin and thioredoxin reductase," *Eur. J. Biochem.*, vol. 267, no. 20, pp. 6102–6109, 2000.

[39] P. J. Halvey, W. H. Watson, J. M. Hansen, Y.-M. Go, A. Samali, and D. P. Jones, "Compartmental oxidation of thiol-disulphide redox couples during epidermal growth factor signalling.," *Biochem. J.*, vol. 386, no. Pt 2, pp. 215–9, 2005.

[40] J.-F. Collet and J. Messens, "Structure, Function, and Mechanism of Thioredoxin Proteins," *Antioxid. Redox Signal.*, vol. 13, no. 8, pp. 1205–1216, 2010.

[41] J. Lu and A. Holmgren, "The thioredoxin antioxidant system," *Free Radic. Biol. Med.*, vol. 66, pp. 75–87, 2014.

[42] R. Environment, O. F. The, C. As, and V. Through, "Redox environment of the cell as viewed through the redox state of the glutathione disulfide/glutathione couple," *Free Radic. Biol. Med.*, vol. 30, no. 11, pp. 1191–1212, 2001.

[43] W. Ren and H. W. Ai, "Genetically encoded fluorescent redox probes," *Sensors (Switzerland)*, vol. 13, no. 11, pp. 15422–15433, 2013.
[44] M. Gutscher, A.-L. Pauleau, L. Marty, T. Brach, G. H. Wabnitz, Y. Samstag, A. J. Meyer, and T. P. Dick, "Real-time imaging of the intracellular glutathione redox potential," *Nat. Methods*, vol. 5, no. 6, pp. 553–559, 2008.
[45] Y.-E. L. Koo, W. Fan, H. Hah, H. Xu, D. Orringer, B. Ross, A. Rehemtulla, M. a Philbert, and R. Kopelman, "Photonic explorers based on multifunctional nanoplatforms for biosensing and photodynamic therapy.," *Appl. Opt.*, vol. 46, pp. 1924–1930, 2007.
[46] Y. S. Huh, A. J. Chung, and D. Erickson, "Surface enhanced Raman spectroscopy and its application to molecular and cellular analysis," *Microfluid. Nanofluidics*, vol. 6, no. 3, pp. 285–297, 2009.
[47] A. J. Meyer and T. P. Dick, "Fluorescent Protein-Based Redox Probes," *Antioxid. Redox Signal.*, vol. 13, no. 5, pp. 621–650, 2010.
[48] T. Tipple, "Methods for the determination of plasma or tissue glutathione levels," vol. 889, pp. 1–8, 2012.
[49] K. R. Keshari, V. Sai, Z. J. Wang, H. F. Vanbrocklin, J. Kurhanewicz, and D. M. Wilson, "Hyperpolarized 1-C-13 -Ascorbic and Dehydroascorbic Acid: Vitamin C as a Probe for Imaging Redox Status in Vivo," vol. 54, no. 6, pp. 922–928, 2014.
[50] T. Cotton and G. Chumanov, "Application of surface-enhanced raman-spectroscopy to biological systems," vol. 22, no. 12, pp. 729–742.
[51] E. Le Ru and P. Etchegoin, *Principles of Surfance Enhanced Raman Spectroscopy and related plasmonic effets*, vol. 1. 2009.
[52] J. Kneipp, H. Kneipp, B. Wittig, and K. Kneipp, "Following the dynamics of pH in endosomes of live cells with SERS nanosensors," *J. Phys. Chem. C*, vol. 114, no. 16, pp. 7421–7426, 2010.
[53] M. Moskovits, "Surface-enhanced spectroscopy," *Rev. Mod. Phys.*, vol. 57, no. 3, pp. 783–826, 1985.
[54] V. Sanna, N. Pala, and M. Sechi, "Targeted therapy using nanotechnology: Focus on cancer," *Int. J. Nanomedicine*, vol. 9, no. 1, pp. 467–483, 2014.
[55] C. Yang, M. Neshatian, M. van Prooijen, and D. B. Chithrani, "Cancer Nanotechnology: Enhanced Therapeutic Response Using Peptide-Modified Gold Nanoparticles," *Journal of Nanoscience and Nanotechnology*, vol. 14, no. 7. pp. 4813–4819, 2014.
[56] T. Vo-Dinh, H.-N. Wang, and J. Scaffidi, "Plasmonic nanoprobes for SERS biosensing and bioimaging," vol. v, no. 2, pp. 265–275, 2012.
[57] R. J. Dijkstra, W. J. J. M. Scheenen, N. Dam, E. W. Roubos, and J. J. ter Meulen, "Monitoring neurotransmitter release using surface-enhanced Raman spectroscopy," *J. Neurosci. Methods*, vol. 159, no. 1, pp. 43–50, 2007.
[58] S. Hong and X. Li, "Optimal size of gold nanoparticles for surface-enhanced Raman spectroscopy under different conditions," *J. Nanomater.*, vol. 2013, 2013.
[59] G. McNay, D. Eustace, W. E. Smith, K. Faulds, and D. Graham, "Surface-enhanced Raman scattering (SERS) and surface-enhanced resonance raman

scattering (SERRS): A review of applications," *Appl. Spectrosc.*, vol. 65, no. 8, pp. 825–837, 2011.

[60] J. Kneipp, H. Kneipp, B. Wittig, and K. Kneipp, "Novel optical nanosensors for probing and imaging live cells," *Nanomedicine Nanotechnology, Biol. Med.*, vol. 6, no. 2, pp. 214–226, 2010.

[61] P. I. T. Thomson, V. L. Camus, Y. Hu, and C. J. Campbell, "Series of quinone-containing nanosensors for biologically relevant redox potential determination by surface-enhanced Raman spectroscopy," *Anal. Chem.*, vol. 87, no. 9, pp. 4719–4725, 2015.

[62] K. Fisher, "Monitoring intracellular redox potential in single cells using SERS nanosensors," 2015.

[63] A. Noto, F. Cibecchini, V. Fanos, and M. Mussap, "NGAL and metabolomics: The single biomarker to reveal the metabolome alterations in kidney injury," *Biomed Res. Int.*, vol. 2013, 2013.

[64] D. S. Wishart, "Emerging applications of metabolomics in drug discovery and precision medicine," *Nat. Rev. Drug Discov.*, vol. 15, no. 7, pp. 473–484, 2016.

[65] J. E. Le Belle, N. G. Harris, S. R. Williams, and K. K. Bhakoo, "A comparison of cell and tissue extraction techniques using high-resolution 1H-NMR spectroscopy," *NMR Biomed.*, vol. 15, no. 1, pp. 37–44, 2002.

[66] M. Pagani, D. Salmaso, G. Rodriguez, D. Nardo, and F. Nobili, "Principal component analysis in mild and moderate Alzheimer's disease - A novel approach to clinical diagnosis," *Psychiatry Res. - Neuroimaging*, vol. 173, no. 1, pp. 8–14, 2009.

[67] E. Martineau, I. Tea, G. Loaëc, P. Giraudeau, and S. Akoka, "Strategy for choosing extraction procedures for NMR-based metabolomic analysis of mammalian cells," *Anal. Bioanal. Chem.*, vol. 401, no. 7, pp. 2133–2142, 2011.

[68] A. Zabek, J. Swierkot, A. Malak, I. Zawadzka, S. Deja, K. Bogunia-Kubik, and P. Mlynarz, "Application of1H NMR-based serum metabolomic studies for monitoring female patients with rheumatoid arthritis," *J. Pharm. Biomed. Anal.*, vol. 117, pp. 544–550, 2016.

[69] C. V. Vaz, M. G. Alves, R. Marques, P. I. Moreira, P. F. Oliveira, C. J. Maia, and S. Socorro, "Androgen-responsive and nonresponsive prostate cancer cells present a distinct glycolytic metabolism profile," *Int. J. Biochem. Cell Biol.*, vol. 44, no. 11, pp. 2077–2084, 2012.

[70] H. Gu, Z. Pan, B. Xi, V. Asiago, B. Musselman, and D. Raftery, "Principal Component Directed Partial Least Squares Analysis for Combining NMR and MS Data in Metabolomics: Application to the Detection of Breast Cancer," *Anal Chim Acta*, vol. 686, no. 765, pp. 57–63, 2012.

[71] H. Wang, L. Wang, H. Zhang, P. Deng, J. Chen, B. Zhou, J. Hu, J. Zou, W. Lu, P. Xiang, T. Wu, X. Shao, Y. Li, Z. Zhou, and Y.-L. Zhao, "^{1}H NMR-based metabolic profiling of human rectal cancer tissue," *Mol. Cancer*, vol. 12, no. 1, p. 121, 2013.

[72] S.-I. Lee and S. Batzoglou, "Application of independent component analysis to microarrays," *Proc. 4th Int. Symp. Indep. Compon. Anal. Blind Signal Sep.*, no. 11,

pp. 879–884, 2003.

[73] N. Kravchenko-Balasha, S. Simon, R. D. Levine, F. Remacle, and I. Exman, "Computational surprisal analysis speeds-up genomic characterization of cancer processes," *PLoS One*, vol. 9, no. 11, 2014.

[74] N. Kravchenko-Balasha, A. Levitzki, A. Goldstein, V. Rotter, A. Gross, F. Remacle, and R. D. Levine, "On a fundamental structure of gene networks in living cells," *Proc. Natl. Acad. Sci. U.S.A*, vol. 109, pp. 4702–4707, 2012.

[75] R. K. Adosraku, G. T. Choi, V. Constantinou-Kokotos, M. M. Anderson, and W. a Gibbons, "NMR lipid profiles of cells, tissues, and body fluids: proton NMR analysis of human erythrocyte lipids.," *J. Lipid Res.*, vol. 35, no. October 1990, pp. 1925–1931, 1994.

[76] B. J. Altman, Z. E. Stine, and C. V Dang, "From Krebs to Clinic : Glutamine Metabolism to Cancer Therapy," vol. 16, no. 10, pp. 619–634, 2017.

[77] J. BERGSTReM, P. FtiRST, L. NORfiE, E. Vinnars, and L. Norse, "Intracellular free amino acid concentration in human muscle tissue," *J. Appl. ~YSlOLOC3Y*, vol. 36, no. 6, 1974.

[78] G. Qing, B. Li, A. Vu, N. Skuli, Z. E. Walton, P. A. Mayes, D. R. Wise, C. B. Thompson, J. M. Maris, D. Hogarty, and M. C. Simon, "ATF4 Regulates MYC-Mediated Neuroblastoma Cell Death upon Glutamine Deprivation," vol. 22, no. 5, pp. 631–644, 2013.

[79] A. N. Lane and T. W. M. Fan, "Regulation of mammalian nucleotide metabolism and biosynthesis," *Nucleic Acids Res.*, vol. 43, no. 4, pp. 2466–2485, 2015.

[80] L. B. Sullivan, D. Y. Gui, A. M. Hosios, L. N. Bush, and M. G. Vander Heiden, "Supporting Aspartate Biosynthesis Is an Essential Function of Respiration in Proliferating Cells," vol. 162, no. 3, pp. 552–563, 2016.

[81] A. M. Weljie, A. Bondareva, P. Zang, and F. R. Jirik, "1H NMR metabolomics identification of markers of hypoxia-induced metabolic shifts in a breast cancer model system," *J. Biomol. NMR*, vol. 49, no. 3–4, pp. 185–193, 2011.

[82] E. G. Armitage and A. D. Southam, "Monitoring cancer prognosis, diagnosis and treatment efficacy using metabolomics and lipidomics," *Metabolomics*, vol. 12, no. 10, pp. 1–15, 2016.

[83] N. Li, K. Ragheb, G. Lawler, J. Sturgis, B. Rajwa, J. A. Melendez, and J. P. Robinson, "Mitochondrial complex I inhibitor rotenone induces apoptosis through enhancing mitochondrial reactive oxygen species production," *J. Biol. Chem.*, vol. 278, no. 10, pp. 8516–8525, 2003.

[84] R. W. Moreadiths and A. L. Lehningert, "The Pathways of Glutamate and Glutamine Oxidation by Tumor Cell Mitochondria," *J. Biolooical Chewistry*, vol. 259, 1984.

[85] G. A. Nagana Gowda, L. Abell, C. F. Lee, R. Tian, and D. Raftery, "Simultaneous Analysis of Major Coenzymes of Cellular Redox Reactions and Energy Using ex Vivo (1)H NMR Spectroscopy.," *Anal. Chem.*, vol. 88, no. 9, p. acs.analchem.6b00442, 2016.

[86] J. W. Kim, I. Tchernyshyov, G. L. Semenza, and C. V. Dang, "HIF-1-mediated

expression of pyruvate dehydrogenase kinase: A metabolic switch required for cellular adaptation to hypoxia," *Cell Metab.*, vol. 3, no. 3, pp. 177–185, 2006.

[87] J. Pelletier, G. Bellot, P. Gounon, S. Lacas-Gervais, J. Pouysségur, and N. M. Mazure, "Glycogen Synthesis is Induced in Hypoxia by the Hypoxia-Inducible Factor and Promotes Cancer Cell Survival," *Front. Oncol.*, vol. 2, no. February, pp. 1–9, 2012.

[88] C. E. Zois and A. L. Harris, "Glycogen metabolism has a key role in the cancer microenvironment and provides new targets for cancer therapy," *J. Mol. Med.*, vol. 94, no. 2, pp. 137–154, 2016.

[89] H. Ripps and W. Shen, "Review: taurine: a 'very essential' amino acid.," *Mol. Vis.*, vol. 18, no. November, pp. 2673–86, 2012.

[90] R. Huxtable, "Physiological Actions of Taurine," vol. 72, no. 1, 1992.

[91] Y. He, Q. Q. Li, and S. C. Guo, "Taurine attenuates dimethylbenz[a]anthracene-induced breast tumorigenesis in rats: A plasma metabolomic study," *Anticancer Res.*, vol. 36, no. 2, pp. 533–544, 2016.

[92] X. Zhang, H. Lu, Y. Wang, C. Liu, W. Zhu, S. Zheng, and F. Wan, "Taurine induces the apoptosis of breast cancer cells by regulating apoptosis-related proteins of mitochondria," *Int. J. Mol. Med.*, vol. 35, no. 1, pp. 218–226, 2015.

[93] A. King, M. A. Selak, and E. Gottlieb, "Succinate dehydrogenase and fumarate hydratase: Linking mitochondrial dysfunction and cancer," *Oncogene*, vol. 25, no. 34, pp. 4675–4682, 2006.

[94] S. Yoon, M.-Y. Lee, S. W. Park, J.-S. Moon, Y.-K. Koh, Y.-H. Ahn, B.-W. Park, and K.-S. Kim, "Up-regulation of Acetyl-CoA Carboxylase α and Fatty Acid Synthase by Human Epidermal Growth Factor Receptor 2 at the Translational Level in Breast Cancer Cells," *J. Biol. Chem.*, vol. 282, no. 36, pp. 26122–26131, 2007.

[95] J. V Swinnen, F. Vanderhoydonc, A. A. Elgamal, M. Eelen, I. Vercaeren, S. Joniau, H. Van Poppel, L. Baert, K. Goossens, W. Heyns, and G. Verhoeven, "Selective activation of the fatty acid synthesis pathway in human prostate cancer," *Int. J. cancer*, vol. 88, no. 2, pp. 176–179, 2000.

[96] J. J. Kamphorst, J. Fan, W. Lu, E. White, and J. D. Rabinowitz, "Liquid chromatography-high resolution mass spectrometry analysis of fatty acid metabolism," *Anal. Chem.*, vol. 83, no. 23, pp. 9114–9122, 2011.

[97] G. Hatzivassiliou, F. Zhao, D. E. Bauer, C. Andreadis, A. N. Shaw, D. Dhanak, S. R. Hingorani, D. A. Tuveson, and C. B. Thompson, "ATP citrate lyase inhibition can suppress tumor cell growth," *Cancer Cell*, vol. 8, no. 4, pp. 311–321, 2005.

[98] L. Jiang, K. Chughtai, S. O. Purvine, Z. M. Bhujwalla, V. Raman, L. Paša-Tolić, R. M. A. Heeren, and K. Glunde, "MALDI-Mass Spectrometric Imaging Revealing Hypoxia-Driven Lipids and Proteins in a Breast Tumor Model," *Anal. Chem.*, vol. 87, no. 12, pp. 5947–5956, 2015.

[99] D. Panigrahy, A. Kaipainen, E. R. Greene, and S. Huang, "Cytochrome P450-derived eicosanoids: the neglected pathway in cancer," *Cancer Metastasis Rev.*, vol. 29, no. 4, pp. 723–735, 2010.

[100] F. Baenke, B. Peck, H. Miess, and A. Schulze, "Hooked on fat: the role of lipid synthesis in cancer metabolism and tumour development," *Dis. Model. Mech.*, vol. 6, no. 6, pp. 1353–1363, 2013.

[101] J. M. Wadsworth, D. J. Clarke, S. A. Mcmahon, J. P. Lowther, A. E. Beattie, P. R. R. Langridge-Smith, H. B. Broughton, T. M. Dunn, J. H. Naismith, and D. J. Campopiano, "The chemical basis of serine palmitoyltransferase inhibition by myriocin," *J. Am. Chem. Soc.*, vol. 135, no. 38, pp. 14276–14285, 2013.

[102] K. E. Choi, Y. S. Jung, D. H. Kim, J. K. Song, J. Y. Kim, Y. Y. Jung, S. Y. Eum, J. H. Kim, N. Y. Yoon, H. S. Yoo, S. B. Han, and J. T. Hong, "Myriocin induces apoptotic lung cancer cell death via activation of DR4 pathway," *Arch. Pharm. Res.*, vol. 37, no. 4, pp. 501–511, 2014.

[103] S. Schiffmann, J. Sandner, K. Birod, I. Wobst, C. Angioni, E. Ruckhäberle, M. Kaufmann, H. Ackermann, J. Lötsch, H. Schmidt, G. Geisslinger, and S. Grösch, "Ceramide synthases and ceramide levels are increased in breast cancer tissue," *Carcinogenesis*, vol. 30, no. 5, pp. 745–752, 2009.

[104] M. R. Reforgiato, G. Milano, G. Fabriàs, J. Casas, P. Gasco, R. Paroni, M. Samaja, R. Ghidoni, A. Caretti, and P. Signorelli, "Inhibition of ceramide de novo synthesis as a postischemic strategy to reduce myocardial reperfusion injury," *Basic Res. Cardiol.*, vol. 111, no. 2, 2016.

[105] B. Oskouian and J. D. Saba, "Cancer treatment strategies targeting sphingolipid metabolism," *Adv. Exp. Med. Biol.*, vol. 688, pp. 185–205, 2010.

[106] G. Paradies, V. Paradies, V. De Benedictis, F. M. Ruggiero, and G. Petrosillo, "Functional role of cardiolipin in mitochondrial bioenergetics," *Biochim. Biophys. Acta - Bioenerg.*, vol. 1837, no. 4, pp. 408–417, 2014.

[107] E. M. Griner and M. G. Kazanietz, "Protein kinase C and other diacylglycerol effectors in cancer," *Nat. Rev. Cancer*, vol. 7, no. 4, pp. 281–294, 2007.

[108] G. A. N. Gowdaa and D. Raftery, "Can NMR solve some significant challenges in metabolomics?," vol. 344, no. 6188, pp. 1173–1178, 2015.

[109] A. Golbraikh and A. Tropsha, "Beware of q2!," *J. Mol. Graph. Model.*, vol. 20, no. 4, pp. 269–276, 2002.

[110] Y. S. Lee, K. M. Choi, S. Lee, D. M. Sin, K. S. Yoo, Y. Lim, Y. M. Lee, J. T. Hong, Y. P. Yun, and H. S. Yoo, "Myriocin, a serine palmitoyltransferase inhibitor, suppresses tumor growth in a murine melanoma model by inhibiting de novo sphingolipid synthesis," *Cancer Biol. Ther.*, vol. 13, no. 2, pp. 92–100, 2012.

[111] D. K. Breslow, "Sphingolipid homeostasis in the endoplasmic reticulum and beyond," *Cold Spring Harb. Perspect. Biol.*, vol. 5, no. 4, pp. 1–16, 2013.

[112] J. Zheng, "Energy metabolism of cancer: Glycolysis versus oxidative phosphorylation (review)," *Oncol. Lett.*, vol. 4, no. 6, pp. 1151–1157, 2012.

[113] Z. Milgraum and R. Pasternack, "Enzymes of the fatty acid synthesis pathway are highly expressed in in situ breast carcinoma," vol. 3, no. November, pp. 2115–2120, 1997.

[114] G. Medes, S. Weinhouse, and A. Thomas, "Metabolism of Neoplastia Tissue. IV. A Study of Lipid Synthesis in Neoplastia Tissue Slices in Vitro," *Cancer Res.*, vol. 13, no. 2, pp. 27–29, 1953.

[115] L. Tong, "Acetyl-coenzyme A carboxylase: Crucial metabolic enzyme and attractive target for drug discovery," *Cell. Mol. Life Sci.*, vol. 62, no. 16, pp. 1784–1803, 2005.
[116] A. Ozkaya, H. Ak, S. Atay, and H. Aydin, "Targeting Mitochondrial Citrate Transport in Breast Cancer Cell Lines," *Anticancer. Agents Med. Chem.*, vol. 15, no. 3, pp. 374–381, 2015.
[117] D. Wang, L. Yin, J. Wei, Z. Yang, and G. Jiang, "ATP citrate lyase is increased in human breast cancer, depletion of which promotes apoptosis," *Tumor Biol.*, vol. 39, no. 4, 2017.
[118] K. E. Wellen, G. Hatzivassiliou, U. M. Sachdeva, T. V Bui, J. R. Cross, and C. B. Thompson, "ATP-Citrate Lyase Links Cellular Metabolism to Histone Acetylation," vol. 324, no. 2009, pp. 0–4, 2009.
[119] D. E. Bauer, G. Hatzivassiliou, F. Zhao, C. Andreadis, and C. B. Thompson, "ATP citrate lyase is an important component of cell growth and transformation," *Oncogene*, vol. 24, no. 41, pp. 6314–6322, 2005.
[120] X. Li, Y. T. Chen, S. Josson, N. K. Mukhopadhyay, J. Kim, M. R. Freeman, and W. C. Huang, "MicroRNA-185 and 342 Inhibit Tumorigenicity and Induce Apoptosis through Blockade of the SREBP Metabolic Pathway in Prostate Cancer Cells," *PLoS One*, vol. 8, no. 8, 2013.
[121] Y. C. Long and J. R. Zierath, "Review series AMP-activated protein kinase signaling in metabolic regulation," *J. Clin. Invest.*, vol. 116, no. 7, pp. 1776–1783, 2006.
[122] F. P. Kuhajda, K. Jennert, F. D. Wood, R. A. Hennigart, L. B. Jacobs, J. D. Dick, and G. R. Pasternack, "Fatty acid synthesis: A potential selective target for antineoplastic therapy," *Med. Sci.*, vol. 91, no. July, pp. 6379–6383, 1994.
[123] E. Marien, M. Meister, T. Muley, S. Fieuws, S. Bordel, R. Derua, J. Spraggins, R. Van De Plas, J. Dehairs, J. Wouters, M. Bagadi, H. Dienemann, M. Thomas, P. A. Schnabel, R. M. Caprioli, E. Waelkens, and J. V. Swinnen, "Non-small cell lung cancer is characterized by dramatic changes in phospholipid profiles," *Int. J. Cancer*, vol. 137, no. 7, pp. 1539–1548, 2015.
[124] I. Vivanco and C. L. Sawyers, "The phosphatidylinositol 3-Kinase–AKT pathway in human cancer," *Nat. Rev. Cancer*, vol. 2, no. 7, pp. 489–501, 2002.
[125] L. Li, J. Han, Z. Wang, J. Liu, J. Wei, S. Xiong, and Z. Zhao, "Mass spectrometry methodology in lipid analysis," *Int. J. Mol. Sci.*, vol. 15, no. 6, pp. 10492–10507, 2014.
[126] B. Wightman, I. Ha, and G. Ruvkun, "Posttranscriptional regulation of the heterochronic gene lin-14 by lin-4 mediates temporal pattern formation in C. elegans," *Cell*, vol. 75, no. 5, pp. 855–862, 1993.
[127] R. C. Lee, R. L. Feinbaum, and V. Ambros, "The C.Elegans heterochronic gene LIN-4 encodes small RNAs with antisense complementary to LIN-14," *Cell*, vol. 75: 843–85, pp. 843–854, 1993.
[128] D. Xu, S. Li, M. Zhang, and Y. Sun, "MicroRNAs act as potential regulators in apoptosis and senescence against carcinogenicity induced by environmental pollutants," *Crit. Rev. Environ. Sci. Technol.*, vol. 45, no. 4, pp. 319–335, 2015.

[129] S. S. Han, W. J. Kim, Y. Hong, S. H. Hong, S. J. Lee, D. R. Ryu, W. Lee, Y. H. Cho, S. Lee, Y. J. Ryu, and Y.-M. Oh, "RNA sequencing identifies novel markers of non-small cell lung cancer," *Lung Cancer*, vol. 84, no. 3, pp. 229–235, 2014.

[130] O. Mueller, K. Hahnenberger, M. Dittmann, Y. Herman, R. Dubrow, R. Nagle, and D. Ilsley, "A microfluidic system for high-speed reproducible DNA sizing and quantitation," *Electrophoresis*, vol. 21, no. 1, pp. 128–134, 2000.

[131] M. C. Brahimi-Horn and J. Pouysségur, "Oxygen, a source of life and stress," *FEBS Lett.*, vol. 581, no. 19, pp. 3582–3591, 2007.

[132] S. L. Lin, D. Chang, D. Y. Wu, and S. Y. Ying, "A novel RNA splicing-mediated gene silencing mechanism potential for genome evolution," *Biochem. Biophys. Res. Commun.*, vol. 310, no. 3, pp. 754–760, 2003.

[133] C. Voellenkle, J. van A. N. Rooij, A. Guffanti, E. Brini, P. Fasanaro, E. Isaia, L. Croft, M. David, M. C. Capogrossi, A. Moles, A. Felsani, and F. Martelli, "Deep-sequencing of endothelial cells exposed to hypoxia reveals the complexity of known and novel microRNAs.," *RNA*, vol. 18, no. 3, pp. 472–84, 2012.

[134] K. Dang and K. A. Myers, "The role of hypoxia-induced miR-210 in cancer progression," *Int. J. Mol. Sci.*, vol. 16, no. 3, pp. 6353–6372, 2015.

[135] S. Nallamshetty, S. Y. Chan, and J. Loscalzo, "Hypoxia: A master regulator of microRNA biogenesis and activity," *North*, vol. 29, no. 10, pp. 1883–1889, 2008.

[136] W. Chang, C. Y. Lee, J.-H. Park, M.-S. Park, L.-S. Maeng, C. S. Yoon, M. Y. Lee, K.-C. Hwang, and Y.-A. Chung, "Survival of hypoxic human mesenchymal stem cells is enhanced by a positive feedback loop involving miR-210 and hypoxia-inducible factor 1.," *J. Vet. Sci.*, vol. 14, no. 1, pp. 69–76, 2013.

[137] W. Yang, J. Wei, T. Guo, Y. Shen, and F. Liu, "Knockdown of miR-210 decreases hypoxic glioma stem cells stemness and radioresistance," *Exp. Cell Res.*, vol. 326, no. 1, pp. 22–35, 2014.

[138] S. Y. Chan, Y. Zhang, C. Hemann, C. E. Mahoney, L. Jay, and J. Loscalzo, "MicroRNA-210 Controls Mitochondrial Metabolism during Hypoxia by Repressing the Iron-Sulfur Cluster Assembly Proteins ISCU1/2," *October*, vol. 10, no. 4, pp. 273–284, 2010.

[139] A. Sheftel, O. Stehling, and R. Lill, "Iron-sulfur proteins in health and disease," *Trends Endocrinol. Metab.*, vol. 21, no. 5, pp. 302–314, 2010.

[140] M. Vander Heiden, L. Cantley, and C. Thompson, "Understanding the Warburg effect: the metabolic requirements of cell proliferation," *Science (80-.).*, vol. 324, no. 5930, pp. 1029–1033, 2009.

[141] D. He, J. Wang, C. Zhang, B. Shan, X. Deng, B. Li, Y. Zhou, W. Chen, J. Hong, Y. Gao, Z. Chen, and C. Duan, "Down-regulation of miR-675-5p contributes to tumor progression and development by targeting pro-tumorigenic GPR55 in non-small cell lung cancer," *Mol. Cancer*, vol. 14, no. 1, pp. 1–14, 2015.

[142] L. A. Ford, A. J. Roelofs, S. Anavi-Goffer, L. Mowat, D. G. Simpson, A. J. Irving, M. J. Rogers, A. M. Rajnicek, and R. A. Ross, "A role for L-α-lysophosphatidylinositol and GPR55 in the modulation of migration, orientation and polarization of human breast cancer cells," *Br. J. Pharmacol.*, vol. 160, no. 3, pp. 762–771, 2010.

[143] Z. Yan, Y. Xiong, W. Xu, J. Gao, Y. Cheng, Z. Wang, F. Chen, and G. Zheng, "Identification of hsa-miR-335 as a prognostic signature in gastric cancer," *PLoS One*, vol. 7, no. 7, 2012.

[144] H. Heyn, M. Engelmann, S. Schreek, P. Ahrens, U. Lehmann, H. Kreipe, B. Schlegelberger, and C. Beger, "MicroRNA miR-335 is crucial for the BRCA1 regulatory cascade in breast cancer development," *Int. J. Cancer*, vol. 129, no. 12, pp. 2797–2806, 2011.

[145] M. Scarola, S. Schoeftner, C. Schneider, and R. Benetti, "miR-335 directly targets Rb1 (pRb/p105) in a proximal connection to p53-dependent stress response," *Cancer Res.*, vol. 70, no. 17, pp. 6925–6933, 2010.

[146] C. Mayr, M. T. Hemann, and D. P. Bartel, "Disrupting the pairing between let-7 and Hmga2 enhances oncogenic transformation," *October*, vol. 315, no. 5818, pp. 1576–1579, 2008.

[147] S. M. Johnson, H. Grosshans, J. Shingara, M. Byrom, R. Jarvis, A. Cheng, E. Labourier, K. L. Reinert, D. Brown, and F. J. Slack, "RAS is regulated by the let-7 microRNA family," *Cell*, vol. 120, no. 5, pp. 635–647, 2005.

[148] C. Wang, Z. Bian, D. Wei, and J. Zhang, "miR-29b regulates migration of human breast cancer cells," *Mol. Cell. Biochem.*, vol. 352, no. 1–2, pp. 197–207, 2011.

[149] X. Wang, J. Zhao, J. Huang, H. Tang, S. Yu, and Y. Chen, "The regulatory roles of miRNA and methylation on oncogene and tumor suppressor gene expression in pancreatic cancer cells," *Biochem. Biophys. Res. Commun.*, vol. 425, no. 1, pp. 51–57, 2012.

[150] S. Y. Park, J. H. Lee, M. Ha, J. W. Nam, and V. N. Kim, "miR-29 miRNAs activate p53 by targeting p85α and CDC42," *Nat. Struct. Mol. Biol.*, vol. 16, no. 1, pp. 23–29, 2009.

[151] H. Zhao, J. Dupont, S. Yakar, M. Karas, and D. LeRoith, "PTEN inhibits cell proliferation and induces apoptosis by downregulating cell surface IGF-IR expression in prostate cancer cells," *Oncogene*, vol. 23, no. 3, pp. 786–794, 2004.

[152] X.-X. Lu, L.-Y. Cao, X. Chen, J. Xiao, Y. Zou, and Q. Chen, "PTEN Inhibits Cell Proliferation, Promotes Cell Apoptosis, and Induces Cell Cycle Arrest via Downregulating the PI3K/AKT/hTERT Pathway in Lung Adenocarcinoma A549 Cells.," *Biomed Res. Int.*, vol. 2016, p. 2476842, 2016.

[153] J. H. Seo, Y. Ahn, S.-R. Lee, C. Y. Yeo, and K. C. Hur, "The Major Target of the Endogenously Generated Reactive Oxygen Species in Response to Insulin Stimulation Is Phosphatase and Tensin Homolog and Not Phosphoinositide-3 Kinase (PI-3 Kinase) in the PI-3 Kinase/Akt Pathway," *Mol. Biol. Cell*, vol. 16, no. 1, pp. 1–13, 2005.

[154] Z. D. Parsons and K. S. Gates, "Thiol-dependent recovery of catalytic activity from oxidized protein tyrosine phosphatases," *Biochemistry*, vol. 52, no. 37, pp. 6412–6423, 2013.

[155] H. Li, E. Solomon, S. D. Muggy, D. Sun, and A. Zolkiewska, "Metalloprotease-disintegrin ADAM12 expression is regulated by Notch signaling via microRNA-29," *J. Biol. Chem.*, vol. 286, no. 24, pp. 21500–21510, 2011.

[156] Y. Laurent Gautron, Joseph M. Rutkowski, Michael D. Burton, Wei Wei and and J. K. E. Wan, "NF-kappa B-YY1-miR-29 Regulatory Circuitry in Skeletal Myogenesis and Rhabdomyosarcoma," *J Comp Neurol. 2013 Novemb. ; 521(16) 3741–3767. doi10.1002/cne.23376*, vol. 521, no. Serres 1985, pp. 759–785, 2014.

[157] C. Culver, A. Sundqvist, S. Mudie, A. Melvin, D. Xirodimas, and S. Rocha, "Mechanism of Hypoxia-Induced NF- B," *Mol. Cell. Biol.*, vol. 30, no. 20, pp. 4901–4921, 2010.

[158] J. Ming, Y. Zhou, J. Du, S. Fan, B. Pan, Y. Wang, L. Fan, and J. Jiang, "miR-381 suppresses C/EBPα-dependent Cx43 expression in breast cancer cells.," *Biosci Rep*, vol. 35, no. 6, pp. 1–10, 2015.

[159] N. Li, X. He, Y. Wei, Y. Wang, L. Liu, and W. Wang, "MiR-381 functions as a tumor suppressor in colorectal," *Onco. Targets. Ther.*, vol. Volume 9, pp. 1231–1239, 2016.

[160] A. Singh and J. Settleman, "EMT, cancer stem cells and drug resistance: an emerging axis of evil in the war on cancer," *Oncogene*, vol. 29, no. 34, pp. 4741–4751, 2011.

[161] H. Peinado, D. Olmeda, and A. Cano, "Snail, ZEB and bHLH factors in tumour progression: An alliance against the epithelial phenotype?," *Nat. Rev. Cancer*, vol. 7, no. 6, pp. 415–428, 2007.

[162] J.-W. Miao, L.-J. Liu, and J. Huang, "Interleukin-6-induced epithelial-mesenchymal transition through signal transducer and activator of transcription 3 in human cervical carcinoma.," *Int. J. Oncol.*, vol. 45, no. 1, pp. 165–76, 2014.

[163] B. T. Kaymaz, N. S. Günel, M. Ceyhan, V. B. Çetintaş, B. Özel, M. K. Yandım, S. Kıpçak, Ç. Aktan, A. A. Gökbulut, Y. Baran, and B. K. Can, "Revealing genome-wide mRNA and microRNA expression patterns in leukemic cells highlighted 'hsa-miR-2278' as a tumor suppressor for regain of chemotherapeutic imatinib response due to targeting STAT5A," *Tumor Biol.*, vol. 36, no. 10, pp. 7915–7927, 2015.

[164] K. Yamane, H. Naito, T. Wakabayashi, H. Yoshida, F. Muramatsu, T. Iba, H. Kidoya, and N. Takakura, "Regulation of SLD5 gene expression by miR-370 during acute growth of cancer cells," *Sci. Rep.*, vol. 6, no. July, pp. 1–12, 2016.

[165] Y. Zhang, G. Xu, G. Liu, Y. Ye, C. Zhang, C. Fan, H. Wang, H. Cai, R. Xiao, Z. Huang, and Q. Luo, "miR-411-5p inhibits proliferation and metastasis of breast cancer cell via targeting GRB2," *Biochem. Biophys. Res. Commun.*, vol. 476, no. 4, pp. 607–613, 2016.

[166] C.-H. Chen, M.-K. Chen, K.-C. G. Jeng, and F.-D. T. Lung, "Effects of peptidic antagonists of Grb2-SH2 on human breast cancer cells.," *Protein Pept. Lett.*, vol. 17, no. 1, pp. 44–53, 2010.

[167] M. Riaz, M. T. M. van Jaarsveld, A. Hollestelle, W. J. C. Prager-van der Smissen, A. A. J. Heine, A. W. M. Boersma, J. Liu, J. Helmijr, B. Ozturk, M. Smid, E. A. Wiemer, J. A. Foekens, and J. W. M. Martens, "MiRNA expression profiling of 51 human breast cancer cell lines reveals subtype and driver mutation-specific miRNAs," *Breast Cancer Res.*, vol. 15, no. 2, 2013.

[168] D. D. Vadysirisack and L. W. Ellisen, "mTOR Activity Under Hypoxia Douangsone," vol. 821, pp. 45–58, 2012.
[169] C. Lou, M. Xiao, S. Cheng, X. Lu, S. Jia, Y. Ren, and Z. Li, "MiR-485-3p and miR-485-5p suppress breast cancer cell metastasis by inhibiting PGC-1α expression," *Cell Death Dis.*, vol. 7, p. e2159, 2016.
[170] M. Anaya-Ruiz, C. Bandala, and J. L. M. Pérez-Santos, "MiR-485 acts as a tumor suppressor by inhibiting cell growth and migration in breast carcinoma T47D cells," *Asian Pacific J. Cancer Prev.*, vol. 14, no. 6, pp. 3757–3760, 2013.
[171] Valerie S. LeBleu, Joyce T. O'Connell, Karina N. Gonzalez Herrera, H. W.-K. K. Pantel, M. C. H. F. M. de C. A. Damascena, L. T. D. Chinen, R. M. Rocha, J. M. Asara, and R. Kalluri, "PGC-1α mediates mitochondrial biogenesis and oxidative phosphorylation to promote metastasis," *Genes Dev*, vol. 16, no. 10, pp. 1–32, 2004.
[172] J. St-Pierre, S. Drori, M. Uldry, J. M. Silvaggi, J. Rhee, S. Jäger, C. Handschin, K. Zheng, J. Lin, W. Yang, D. K. Simon, R. Bachoo, and B. M. Spiegelman, "Suppression of Reactive Oxygen Species and Neurodegeneration by the PGC-1 Transcriptional Coactivators," *Cell*, vol. 127, no. 2, pp. 397–408, 2006.
[173] A. Gęgotek, J. Nikliński, N. Žarković, K. Žarković, G. Waeg, W. Łuczaj, R. Charkiewicz, and E. Skrzydlewska, "Lipid mediators involved in the oxidative stress and antioxidant defence of human lung cancer cells," *Redox Biol.*, vol. 9, pp. 210–219, 2016.
[174] G. Barrera, "Oxidative Stress and Lipid Peroxidation Products in Cancer Progression and Therapy," *ISRN Oncol.*, vol. 2012, pp. 1–21, 2012.
[175] T. Pfeiffer, S. Schuster, and S. Bonhoeffer, "Cooperation and Competition in the Evolution of ATP-Producing Pathways," *Science (80-.).*, vol. 292, no. 5516, pp. 504–507, 2001.
[176] B. Marengo, M. Nitti, A. L. Furfaro, R. Colla, C. De Ciucis, U. M. Marinari, M. A. Pronzato, N. Traverso, and C. Domenicotti, "Redox homeostasis and cellular antioxidant systems: Crucial players in cancer growth and therapy," *Oxid. Med. Cell. Longev.*, vol. 2016, 2016.
[177] J. P. Piret, D. Mottet, M. Raes, and C. Michiels, "CoCl2, a chemical inducer of hypoxia-inducible factor-1, and hypoxia reduce apoptotic cell death in hepatoma cell line HepG2," *Ann N Y Acad Sci*, vol. 973, pp. 443–447, 2002.
[178] "C. elegans EGL-9 and Mammalian Homologs Define a Family of Dioxygenases that Regulate HIF by Prolyl Hydroxylation," vol. 107, pp. 43–54, 2001.
[179] Y. Yuan, G. Hilliard, T. Ferguson, and D. E. Millhorn, "Cobalt inhibits the interaction between hypoxia-inducible factor-?? and von Hippel-Lindau protein by direct binding to hypoxia-inducible factor-??," *J. Biol. Chem.*, vol. 278, no. 18, pp. 15911–15916, 2003.
[180] Y. Dai, W. Li, M. Zhong, J. Chen, Y. Liu, Q. Cheng, and T. Li, "Preconditioning and post-treatment with cobalt chloride in rat model of perinatal hypoxic-ischemic encephalopathy," *Brain Dev.*, vol. 36, no. 3, pp. 228–240, 2014.
[181] W. Wu and S. Zhao, "Metabolic changes in cancer: beyond the Warburg effect,"

Abbs, vol. 45, no. 1, pp. 18–26, 2013.

[182] A. Vengellur and J. J. LaPres, "The role of hypoxia inducible factor 1α in cobalt chloride induced cell death in mouse embryonic fibroblasts," *Toxicol. Sci.*, vol. 82, no. 2, pp. 638–646, 2004.

[183] E. M. Palsson-Mcdermott and L. A. J. O'Neill, "The Warburg effect then and now: From cancer to inflammatory diseases," *BioEssays*, vol. 35, no. 11, pp. 965–973, 2013.

[184] M. Upadhyay, J. Samal, M. Kandpal, O. V. Singh, and P. Vivekanandan, "The Warburg effect: Insights from the past decade," *Pharmacol. Ther.*, vol. 137, no. 3, pp. 318–330, 2013.

[185] W. Chen, Zheng Sun, X.-J. Wang, T. Jiang, Z. Huang, D. Fang, and D. Zhang, "Direct interaction between Nrf2 and p21 upregulates Nrf-2-mediated antioxidant responce," *Mol. Cell*, vol. 34, no. 6, pp. 663–673, 2009.

[186] A. Singh, C. Happel, S. K. Manna, G. Acquaah-Mensah, J. Carrerero, S. Kumar, P. Nasipuri, K. W. Krausz, N. Wakabayashi, R. Dewi, L. G. Boros, F. J. Gonzalez, E. Gabrielson, K. K. Wong, G. Girnun, and S. Biswal, "Transcription factor NRF2 regulates miR-1 and miR-206 to drive tumorigenesis," *J. Clin. Invest.*, vol. 123, no. 7, pp. 2921–2934, 2013.

[187] M. Jaramillo and D. Zhang, "The emerging role of the Nrf2–Keap1 signaling pathway in cancer," *Genes Dev.*, vol. 27, pp. 2179–2191, 2013.

[188] A. Koong, K. Che, and A. Giaccia, "Hypoxia causes the activation of nuclear factor kappa through the phosphorilation of I-kB on tyrosine residues," *Cancer Res*, no. 54, pp. 1425–1430, 1994.

[189] R. D. Guzy, B. Hoyos, E. Robin, H. Chen, L. Liu, K. D. Mansfield, M. C. Simon, U. Hammerling, and P. T. Schumacker, "Mitochondrial complex III is required for hypoxia-induced ROS production and cellular oxygen sensing," *Cell Metab.*, vol. 1, no. 6, pp. 401–408, 2005.

[190] G. B. Waypa, J. D. Marks, R. Guzy, P. T. Mungai, J. Schriewer, D. Dokic, and P. T. Schumacker, "Hypoxia Triggers Subcellular Compartmental Redox Signaling in Vascular Smooth Muscle Cells," *Circ. Res.*, vol. 106, no. 3, pp. 526–535, 2011.

[191] J. Jiang, C. Auchinvole, K. Fisher, and C. J. Campbell, "Quantitative measurement of redox potential in hypoxic cells using SERS nanosensors," *Nanoscale*, vol. 6, no. 20, pp. 12104–12110, 2014.

[192] L. E. Jamieson, A. P. Bell, D. J. Harrison, and C. J. Campbell, "Monolayer to MTS: using SEM, HIM, TEM and SERS to compare morphology, nanosensor uptake and redox potential in MCF7 cells," *Proc. SPIE*, vol. 9531, no. June 2015, p. 95311I, 2015.

[193] C. A. R. Auchinvole, "SERS Nanosensors for Intracellular Redox Potential Measurements Doctor of Philosophy ," no. September, 2011.

[194] S. W. Bishnoi, C. J. Rozell, C. S. Levin, M. K. Gheith, B. R. Johnson, D. H. Johnson, and N. J. Halas, "All-optical nanoscale pH meter," *Nano Lett.*, vol. 6, no. 8, pp. 1687–1692, 2006.

[195] L. E. Jamieson, A. Jaworska, J. Jiang, M. Baranska, D. J. Harrison, and C. J.

Campbell, “Simultaneous intracellular redox potential and pH measurements in live cells using SERS nanosensors,” *Analyst*, vol. 140, no. 7, pp. 2330–2335, 2015.

[196] M. A. Ochsenku, P. R. T. Jess, H. Stoquert, K. Dholakia, and C. J. Campbell, “Nanoshells for Surface-Enhanced Raman,” vol. 3, no. 11, pp. 3613–3621, 2009.

[197] J. Kneipp, H. Kneipp, B. Wittig, and K. Kneipp, “One- and two-photon excited optical pH probing for cells using surface-enhanced raman and hyper-raman nanosensors,” *Nano Lett.*, vol. 7, no. 9, pp. 2819–2823, 2007.

[198] A. Costa, A. Scholer-Dahirel, and F. Mechta-Grigoriou, “The role of reactive oxygen species and metabolism on cancer cells and their microenvironment,” *Semin. Cancer Biol.*, vol. 25, pp. 23–32, 2014.

[199] N. S. Chandel, E. Maltepe, E. Goldwasser, C. E. Mathieu, M. C. Simon, and P. T. Schumacker, “Mitochondrial reactive oxygen species trigger hypoxia-induced transcription.,” *Proc. Natl. Acad. Sci. U. S. A.*, vol. 95, no. 20, pp. 11715–20, 1998.

[200] “Solution Structure of the zinc finger domain of Transcriptional repressor CTCF protein.” .

[201] I-Cheng Ho, “GATA3 and the T-cell lineage: essential functions before and after T-helper-2-cell differentiation,” vol. 9, no. 2, pp. 125–135, 2010.

[202] W. G. Kaelin and P. J. Ratcliffe, “Oxygen Sensing by Metazoans: The Central Role of the HIF Hydroxylase Pathway,” *Mol. Cell*, vol. 30, no. 4, pp. 393–402, 2008.

[203] P. Mak, I. Leav, B. Pursell, D. Bae, X. Yang, C. A. Taglienti, L. M. Gouvin, V. M. Sharma, and A. M. Mercurio, “ERβ Impedes Prostate Cancer EMT by Destabilizing HIF-1α and Inhibiting VEGF-Mediated Snail Nuclear Localization: Implications for Gleason Grading,” vol. 17, no. 4, pp. 319–332, 2011.

[204] W. Luo and G. L. Semenza, “Pyruvate kinase M2 regulates glucose metabolism by functioning as a coactivator for hypoxia-inducible factor 1 in cancer cells.,” *Oncotarget*, vol. 2, no. 7, pp. 551–556, 2011.

[205] K. L. Eales, K. E. R. Hollinshead, and D. A. Tennant, “Hypoxia and metabolic adaptation of cancer cells,” *Oncogenesis*, vol. 5, no. 1, p. e190, 2016.

[206] S. Wanschura, E. F. P. M. Schoenmakers, C. Huysmans, S. Bartnitzke, W. J. M. Van De Ven, and J. Bullerdiek, “Mapping of the gene encoding the human hepatoma-derived growth factor (HDGF) with homology to the high-mobility group (HMG)-1 protein to Xq25,” *Genomics*, vol. 32, no. 2, pp. 298–300, 1996.

[207] P. Varilly and D. Chandler, “Redox properties of the A-domain of the HMGB1 protein,” vol. v, no. 2, pp. 265–275, 2012.

[208] S. Qin, H. Wang, R. Yuan, H. Li, M. Ochani, K. Ochani, M. Rosas-Ballina, C. J. Czura, J. M. Huston, E. Miller, X. Lin, B. Sherry, A. Kumar, G. LaRosa, W. Newman, K. J. Tracey, and H. Yang, “Role of HMGB1 in apoptosis-mediated sepsis lethality,” *J. Exp. Med.*, vol. 203, no. 7, pp. 1637–1642, 2006.

[209] J. H. Gilmore, “HMGB1 in Cancer: Good, Bad, or Both?,” *North*, vol. 29, no. 10, pp. 1883–1889, 2008.